

International Journal of Innovations in Materials Science and Engineering

IMSE

Vol.1 No. 2

Guest Editor
Prof. Fabrizia Ghezzi

 **EDUGAIT**
PRESS

International Journal of Innovations in Materials Science and Engineering (IMSE)

VOLUME 1, NUMBER 2

July 2014

Preface

This Special Issue of the International Journal of Innovation in Materials Science and Engineering is a collection of a few selected manuscripts in the areas of Mechanical, Civil and Materials Engineering presenting analyses and computational methods, as well as experimental studies of engineering problems of structural vibrations whose solutions focus on strategies for optimizing or quantifying the damping of the system at the propagating disturbance.

This short collection of works is meant to give to the reader an overview of different vibrations problems that can be found in diverse areas of Engineering. Particularly, the common aspect linking these works is the way these problems have been or can be solved or analyzed by proposing innovative solutions, in terms of novel materials or systems, and methods for the analysis, detection and optimization of the damping of vibrations in these very diverse applications.

Five of these manuscripts are the extended versions of articles accepted and included in the Mini-Symposium MS26 - *Development of Materials and Systems for Vibrations Damping* - of the 11th biennial International Conference on vibration Problems (ICOVP-2013) held in Lisbon in September 9-12, 2013. The event was jointly organized by the Department of Civil Engineering of the Faculdade de Ciências e Tecnologia of the Universidade Nova of Lisbon FCT/UNL, and IDMEC, the Institute of Engineering Mechanics of the Instituto Superior Técnico of the Technical University of Lisbon (IST/UTL) and the Institute of Engineering Mechanics of the Instituto Superior Técnico of the Technical University of Lisbon (IST/UTL).

I would like to thank all the authors for their contributions to this Special Issue,

Fabrizia Ghezzi

Shenzhen, P.R. China,

July 2014.



Tel: +1 (613) 663-9646, Fax: +1 (613) 801-1406
PO Box 72032, 4048 Carling Ave,
Ottawa, ON, K2K 2P4, Canada

Electrorheological Fluid Power Dissipation and Requirements for an Adaptive Tunable Vibration Absorber

Nicklas Norrick¹

¹Institute of Structural Dynamics, Technische Universität Darmstadt, Darmstadt, Germany

Electrorheological fluid (ERF) is an adaptive material which changes its material properties quickly and reversibly in response to an electric field. The effect was discovered by Winslow in 1947. The change in apparent material behavior makes ERF interesting for use in the on-line tuning of dynamic systems such as tuned vibration absorbers (TVAs). In this paper, an adaptive multibody absorber prototype filled with ERF is investigated. Its performance is evaluated experimentally and a numerical model is validated with the measurements. Special focus on power requirements and efficiency of the semi-active tuning mechanism. The multibody adaptive TVA prototype consists of a closed plastic casing, in which two rigid bodies are suspended via elastic helical springs. Two independent high-voltage channels allow the application of up to 6000 V in narrow gaps between the absorber bodies and the absorber casing, influencing the material properties of the ERF. Experiments show the continuous change of the apparent first natural frequency and corresponding damping of the absorber in response to the applied high voltages. A mathematical model of the prototype including a nonlinear description of the ER material behavior is presented. An extended BINGHAM model is used to describe the behavior of the ERF under influence of an electric field. Using the validated numerical model, the absorber performance on a virtual test system and the power dissipation in the absorber can be calculated. The power dissipation is compared to the measured power requirements of the ERF and the power consumption of the high voltage amplifiers. The efficiency of the ER material to induce damping is very shown to be very high. In contrast, the efficiency of the high voltage amplifiers used in the experiments is very low. The results can help foster further developments of adaptive TVAs and other semi-active devices utilizing ERF as an adjustment mechanism.

Index Terms—Electrorheological Fluid, ERF, Tuned Vibration Absorber, Semi-Active

I. INTRODUCTION

Passive vibration absorbing devices have been used in structural dynamics for over a century, first patented by Frahm for the damping of ship roll [1]. Since Den Hartog [2] developed the theory of the optimal tuned vibration absorber (TVA), the governing equations have been the subject matter of fundamental structural dynamics courses around the world. It is well-known that the classical TVA is only capable of quenching vibrations at its tuning frequency. When excitation frequencies of a system or system properties change during operation, the mistuned absorber may exhibit worse behavior than the original system without the absorber. To overcome this flaw, much research has been presented regarding active or semi-active TVAs.

Using electrorheological fluids (ERF), the natural frequency and damping characteristics of a multibody tuned vibration absorber can be changed to achieve vibration attenuation over a broad frequency band.

Preumont gives a concise definition of semi-active devices:

“Semi-active control devices are essentially passive devices where properties (stiffness, damping, ...) can be adjusted in real time, but they cannot input energy directly in the system being controlled” [3].

Because of this, semi-active devices have certain advantages over fully active systems. First, semi-active devices require very little energy in comparison with an active system for the same reduction in vibration amplitudes. Second, since

semi-active devices cannot serve as a source of energy for the system they are influencing, destabilization due to faulty control parameters or a failure in the system is generally not a problem. Hrovat offers a comprehensive comparison of the characteristics of passive, semi-active and active TVA performance [4].

Since Winslow discovered the electrorheological effect nearly seventy years ago [5], [6], many researchers have used electrorheological materials to influence dynamic systems. Bullough and Foxon [7] used adaptive electrorheological dampers for the control of unwanted vibrations.

The magnetorheological effect creates very similar changes in the material behavior of magnetorheological fluids (MRF), which have also been studied extensively for the use in adjustable dampers. Recent work by Sims et al. [8] is an example from academia. The LORD Corporation has been marketing industrial products utilizing this technology for over a decade [9].

For TVAs the change in material behavior exhibited by either ERF or MRF has been investigated experimentally and theoretically. Janocha and Jendritza [10] first presented a prototype TVA with adjustable damping characteristics utilizing electrorheological fluid. Sloshing-type vibration absorbers for civil engineering applications have been studied by Truong and Semercigil [11] and Sakamoto et al. [12]. Both groups have presented experimental results using ERF as a sloshing liquid in a tank. Truong and Semercigil noted a change solely in the damping characteristic of the TVA while Sakamoto et al. presented a design that makes it possible to change the effective mass of the absorber and thereby influence the absorber's natural frequency. Koo [13] used MRF dampers in a

Corresponding author: N. Norrick (email: norrick@sdy.tu-darmstadt.de).

prototype of a semi-active TVA and presented both theoretical and experimental results highlighting the advantages of the semi-active system over classical passive TVAs. Instead of MRF, Holdhusen [14] used magnetorheological elastomers (MRE) to design a semi-active TVA with adaptive stiffness, in turn facilitating a change in absorber natural frequency. Several research groups have discussed the change in a sandwich beam's stiffness with ERF or MRF and done extensive theoretical and experimental work. Earliest work was done by Choi et al. [15]. Only recently has the change in beam stiffness been used to change absorber natural frequency on-line by Hirunyapruk [16]. Sun and Thomas used a modified rotational viscometer as an electrorheological dynamic torsional absorber to effectively reduce torsional rotor vibrations of the viscometer rotor [17].

The subject of this paper is an existing prototype semi-active TVA, designed to fit into the steering wheel of a luxury automobile and influence lateral vibrations in the steering wheel plane. In previous work, it has been proven that the natural frequency and damping of this prototype can be changed by applying electrical field strengths of up to 6kV/mm [18], [19]. The prototype has also been fitted to an automobile substructure to test the system in nearly real conditions. Comprehensive measurements validated the prototype's performance when the automobile substructure was subjected to harmonic and white noise excitation [20]. To quantify the advantage of a semi-active TVA compared to fully active solutions, this paper concentrates on the power consumption and efficiency (defined as the ratio of power dissipation of the "smart" material to its power consumption) of the mentioned prototype.

II. MULTIBODY TVA PROTOTYPE

The prototype TVA investigated in this study consists of a closed plastic casing, in which two bodies are suspended via sets of helical springs. The coupling body (mass m_1), has only 10% of the mass of the main body (mass m_2). Modal analysis of the empty prototype was used to validate the analytically predicted natural frequencies of the system.

In the narrow gaps (~ 1 mm) between the coupling body and the casing a high voltage U_1 can be applied, while in the narrow gaps between the coupling body and the main body a different high voltage U_2 can be applied. Both voltages are supplied by independently controlled high voltage amplifiers, each up to 6000 V.

The ER material used in this study is a suspension of polyurethane particles with an average diameter of $3 \mu\text{m}$ in silicone oil. The solid particle content is $\Phi = 42\%$.

The casing of the absorber is filled with ERF under a slight overpressure to prevent the formation of air bubbles, which have a negative effect on the dielectric strength of the material. A photograph of the prototype is shown in Fig. 1.

The prototype was tested on a vibration testing table. A detailed diagram of the test rig is shown in Fig. 2. A real-time control system (dSpace DS1103) is used for data acquisition and the output of the control signals for the two high-voltage generators and the frequency signal Ω for the drive motor. The

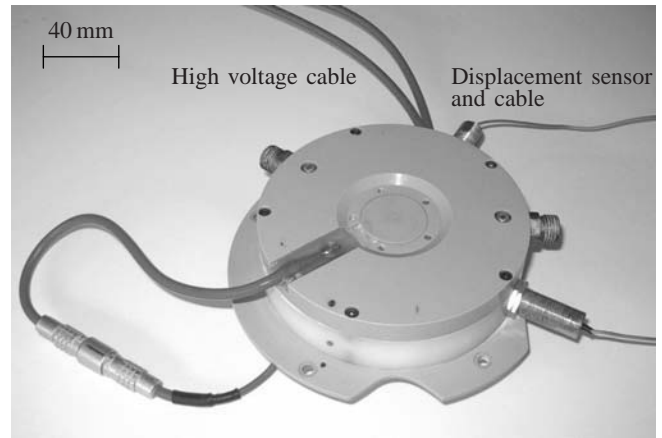


Fig. 1. Photograph of the multibody tunable vibration absorber prototype

drive motor induces a nearly harmonic displacement excitation with a fixed amplitude via a crankshaft. The table displacement $u(t)$ and relative displacement $q_r(t)$ of the main absorber body inside the plastic housing are measured with eddy-current displacement sensors. In addition to the table displacement, a piezoelectric accelerometer on the table records the table acceleration $\ddot{u}(t)$. The actually applied high voltages U_1 and U_2 (each up to 6000 V) are controlled and logged throughout the experiments. All of the acquired signals are filtered via identical analog low-pass filters to eliminate aliasing errors.

Because of the high voltages used in the experiments, special attention must be placed on the connection of the prototype and all components used during measurement to the electrical ground. Most importantly, we want to minimize the risk of electrical shock for people working in the lab. Additionally, sensitive measurement electronics must be protected from electrostatic discharges which can produce erroneous measurements (a minor side effect) or destroy expensive laboratory equipment.

The test setup allows the measurement of the complex frequency response

$$\underline{H}(\Omega) = \frac{q_r(\Omega)}{u(\Omega)} \quad (1)$$

of the TVA prototype with amplitude $|\underline{H}(\Omega)|$ and phase $\psi(\Omega)$. A fixed excitation amplitude $\hat{u} = 0.4$ mm was chosen for all measurements.

III. MATHEMATICAL MODEL

An idealized mechanical model of the absorber is shown in Fig. 3. The casing (shown in white) houses the coupling mass (dark gray) and the main mass (light gray). The application of the high voltage U_1 or U_2 influences the ERF and can achieve a blockage of the spring-damper set 1 or 2, respectively, thereby influencing system damping and natural frequencies.

To model the influence of the ERF, a nonlinear extended BINGHAM-type model based on viscometer measurements is used. The model parameters are the electric field strength E_{el} and the shear rate $\dot{\gamma}$. The shear stress τ_{ERF} is the sum of the

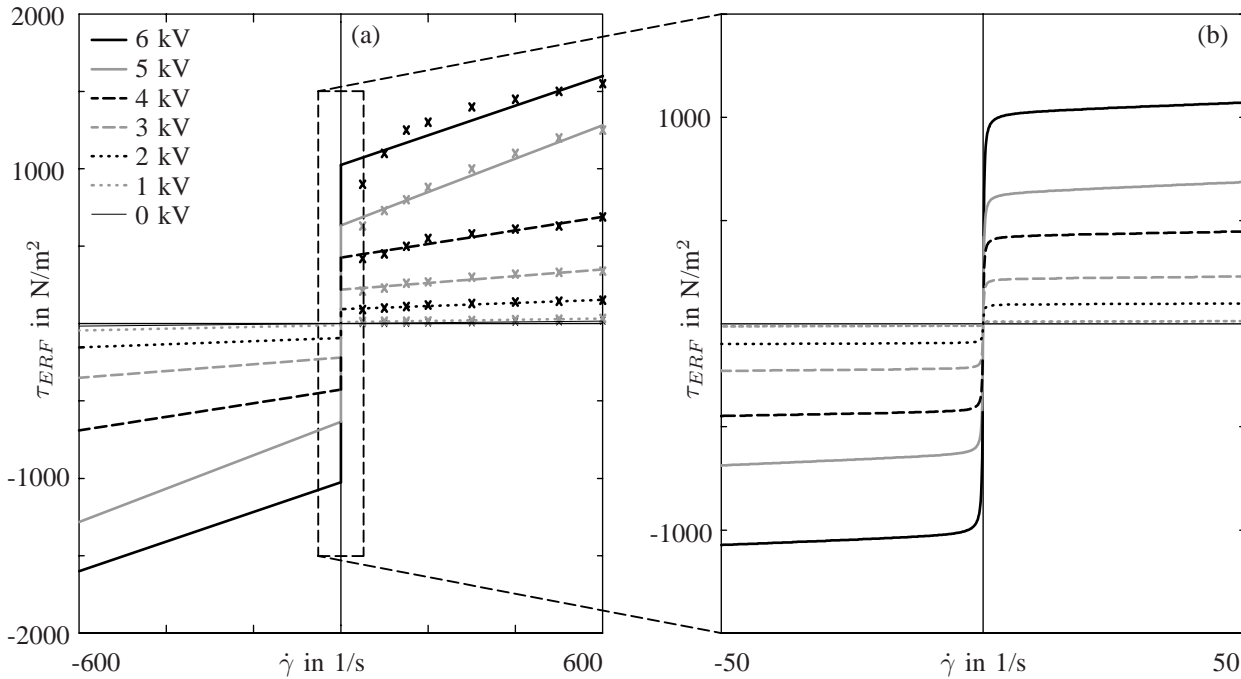


Fig. 4. Shear stress due to shear rate with BINGHAM-type model (a) and zoom of the interesting area showing the effect of multiplication with the arctan-function (b)

In our case, the effective electrode area $A = 8657 \text{ mm}^2$. The enclosed area in a force-displacement diagram is the damping work done by one vibration cycle. Multiplication of the damping work with the frequency f (in Hz) yields the damping power P (in W)

$$P = \oint \vec{F}_{ERF} \vec{ds} f. \quad (8)$$

The shown model for the semi-active tuned vibration absorber and the electrorheological material has been parameterized and validated by vibration response measurements with different types of excitation [23]. The model reproduces the measured dynamic behavior of the absorber under influence of applied high voltage extremely well. Two examples of the quality of the model are shown in Figures 5 and 6. Visible is the measured and simulated system frequency response (amplitude $|\underline{H}(\Omega)|$ and phase $\psi(\Omega)$) of the absorber prototype due to base excitation with a constant amplitude and 4000 V applied to either channel 1 or channel 2 respectively. For comparison, the best linear model is shown as well (dotted line). The discrepancy between the linear model and the measurements is most evident in the amplitude response between about 10 and 20 Hz.

A variation of the applied voltage alters the resonance frequency of the absorber in a range between 18.4 and 24.9 Hz. This can clearly be seen in the measured frequency response curves for increasing voltages in Figures 7 and 8. These show the frequency response of the absorber main body for rising high voltages applied to channel 1 and channel 2, respectively. In both figures, a drop in the resonance frequency is visible between the two curves for 0 V and 2000 V. This drop is due to a change in the added mass of the ERF. From that

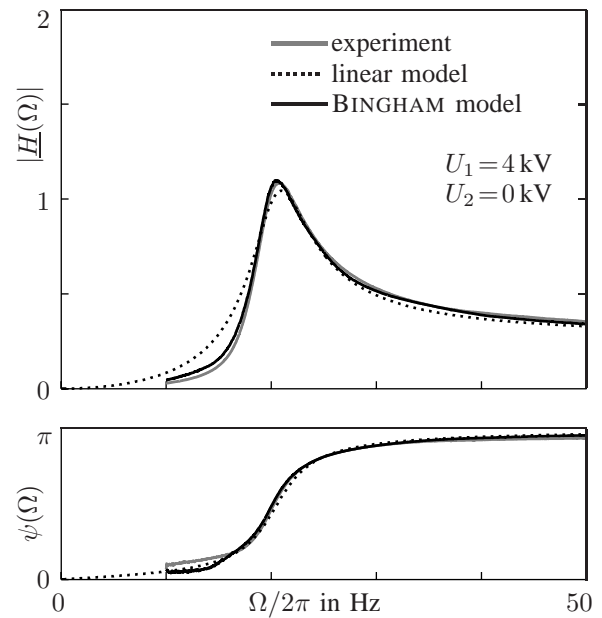


Fig. 5. Measured and simulated displacement amplitude $|\underline{H}(\Omega)|$ and phase $\psi(\Omega)$ for the absorber prototype due to base excitation, $U_1 = 4 \text{ kV}$ and $U_2 = 0 \text{ kV}$

point on, an increase in high voltage results in an increased resonance frequency. The response curves for both cases are similar because of the large ratio m_2/m_1 and the comparable magnitude of the spring stiffnesses k_1 and k_2 .

A closer look at the simple model from Fig. 3 can help explain this: When high voltage is applied to channel 1, the ERF in the gap between main body and coupling body blocks

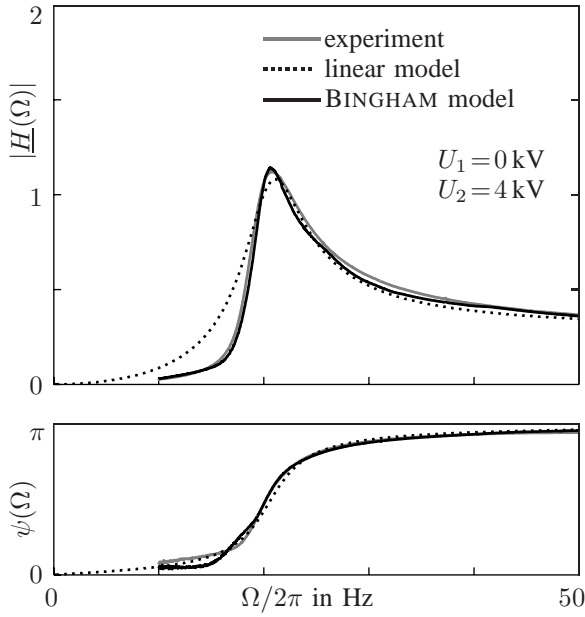


Fig. 6. Measured and simulated displacement amplitude $|\underline{H}(\Omega)|$ and phase $\psi(\Omega)$ for the absorber prototype due to base excitation, $U_1 = 0$ kV and $U_2 = 4$ kV

the compliance of spring k_1 , thereby increasing the apparent natural frequency of the absorber. Ideally, when $m_1 \rightarrow 0$ and $k_1 = k_2$ we will have a base natural frequency of

$$\omega_{base} = \sqrt{\frac{k_2}{2m_2}}. \quad (9)$$

A complete blocking of spring k_1 will result in a natural frequency of

$$\omega_1 = \sqrt{\frac{k_2}{m_2}} = \sqrt{2}\omega_{base}, \quad (10)$$

yielding an increase in natural frequency with the factor $\sqrt{2}$. When high voltage is applied to channel 2, an analogous effect blocks the compliance of spring k_2 , resulting in the same frequency ratio

$$\omega_2 = \sqrt{\frac{k_1}{m_2}} = \sqrt{2}\omega_{base}. \quad (11)$$

The measurements show that the prototype absorber attains a frequency ratio of 1.35, quite close to the ideal ratio of $\sqrt{2}$.

IV. APPLICATION OF THE ABSORBER TO A HARMONICALLY EXCITED SYSTEM

The validated model can also be used to apply the virtual absorber to a vibrating system and evaluate the semi-active system's vibration reduction potential. Let us look at a simple case and apply the tunable absorber to a one-degree-of-freedom system with a natural frequency of 20 Hz and 2% damping. For this example, the system mass is $m_{sys} = 10$ kg, about 10 times the absorber mass, a common ratio for TVAs. The resulting parameters are the stiffness $k_{sys} = 158$ kN/m and damping $b_{sys} = 50$ Ns/m. The system is subjected to harmonic force excitation $F(t) = \hat{F} \cos(\Omega t)$. Due to the ER material behavior under influence of the electrical field,

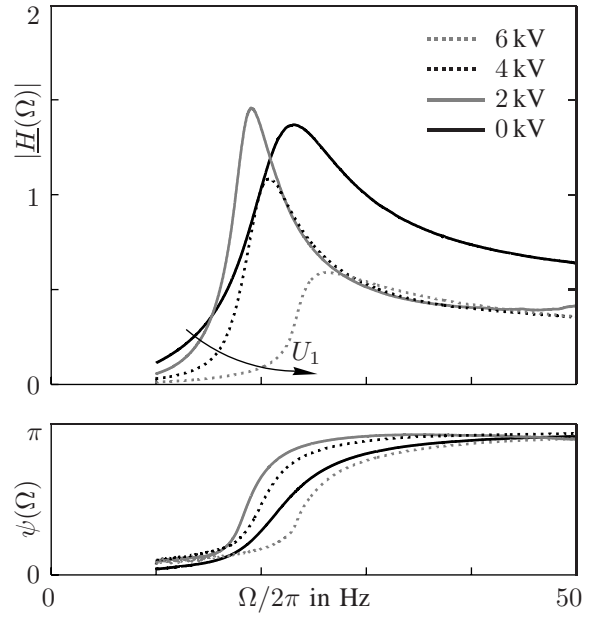


Fig. 7. Measured displacement amplitude $|\underline{H}(\Omega)|$ and phase $\psi(\Omega)$ for the absorber prototype due to base excitation, $U_1 = 0$ to 6 kV and $U_2 = 0$ kV

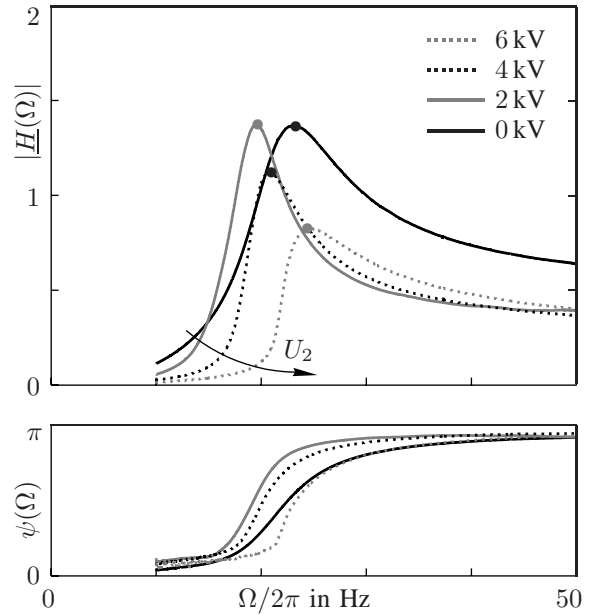


Fig. 8. Measured displacement amplitude $|\underline{H}(\Omega)|$ and phase $\psi(\Omega)$ for the absorber prototype due to base excitation, $U_1 = 0$ kV and $U_2 = 0$ to 6 kV

the semi-active system is non-linear and the magnitude of \hat{F} influences the results. Fig. 9 shows a schematic diagram of the system including a sensor, controller and voltage amplifiers to complete the semi-active system.

The results for $\hat{F} = 1$ N can be seen in Fig. 10. The dashed line is the magnitude of the frequency response of the reference system. When the adaptive absorber is applied and different voltages from 0 to 6000 V are kept constant during operation, the gray response curves are attained. The thick black line is the frequency response we can achieve when we

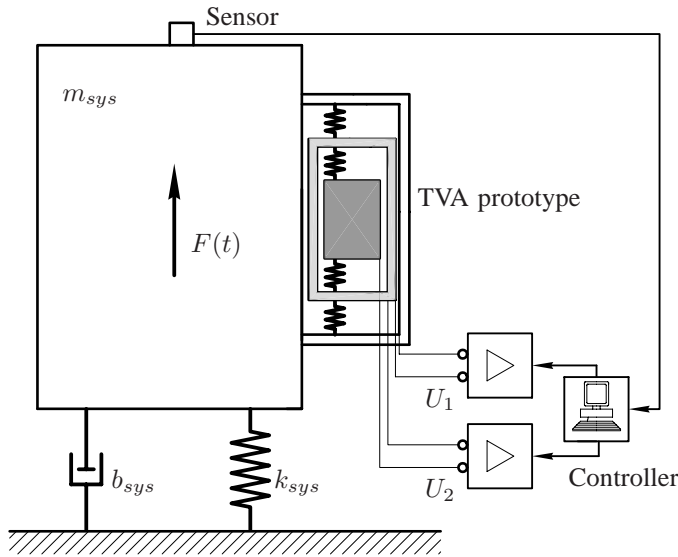


Fig. 9. Schematic diagram of the one-degree-of-freedom system with applied TVA prototype

suppose that the high voltage applied to the TVA is optimally switched depending on excitation frequency, for example by a simple feed forward control algorithm.

For very large force excitation amplitudes, on the order of $\hat{F} = 100$ N, the yield stress of the ER material is too small to show a visible effect on the absorber natural frequency and the net effect of the semi-active absorber on the system is that of an adjustable viscous damper.

To quantify the response due to broadband excitation, we can calculate the area under the response amplitude curves in a frequency band from 10 to 30 Hz for the system without absorber, with a passive absorber (corresponding to no voltage applied) and the optimally switching semi-active absorber. The resulting values are 0.05 mm/Ns for the system without absorber, 0.0474 mm/Ns for the passive system and 0.0198 mm/Ns for the semi-active system. The passive absorber achieves a broadband reduction of only 5%, whereas the semi-active system attains a reduction of 60%.

These numbers quantify the great advantage of the semi-active system. If the power needed to induce this switch in system behavior is small, the resulting efficiency of the device is high. In the following sections, we will therefore focus on power dissipation and power consumption of the ER material.

V. POWER DISSIPATION IN THE ERF

The power dissipation in the ERF cannot be measured directly, but can be calculated from the hysteretic force-displacement diagrams created with the validated model. Because of the previously discussed inherent symmetry of the prototype's dynamic behavior, we will only alter the high voltage of channel 2 (U_2) in the following studies. Two distinct cases will be discussed, and because of symmetry, the findings apply to channel 1 as well.

Case 1:

The vibration absorber is tuned to a varying excitation frequency via high voltage U_2 . The base excitation amplitude \hat{u} is assumed to be constant. The points of operation for each high voltage are marked with bullets (\bullet) in Fig. 8.

Case 2:

The vibration absorber is subjected to a fixed excitation frequency of $\Omega/2\pi = 30$ Hz. The base excitation amplitude \hat{u} is constant. The applied high voltage U_2 is increased from 0 to 6000 V.

Fig. 11 shows the calculated force-displacement and force-velocity characteristic obtained from the extended BINGHAM-type model for **Case 1**. In this case, the system parameters and excitation frequency change from one voltage to the next, so the displacement q_r of the absorber body is diminished with rising voltages.

Fig. 12 shows the calculated force-displacement and force-velocity characteristic obtained from the extended BINGHAM-type model for **Case 2**. For this parameter set, the system response amplitude \hat{q}_r remains nearly constant with the exception of a change in system behavior from linear (no voltage applied) to non-linear (high voltage applied). In both cases, the damping work per cycle increases visibly in accordance with the increase in high voltage.

From this data, the damping power for these different points of operation is calculated and shown in Fig. 13. The quadratic trend of the data for **Case 2** is due to Eq. (4) and the fact that the displacement amplitude \hat{q}_r is constant. This trend is not evident in the data for **Case 1** because of the aforementioned change in the displacement amplitude \hat{q}_r .

During the course of the experiments, it was postulated that the dissipated energy in the prototype absorber would heat the ERF and thereby change the material's damping properties during operation. To test this, a temperature probe was mounted inside the housing during operation near resonance and the ERF temperature was monitored over a period of 22 minutes from a starting point of 25.4 °C. Fig. 15 shows the results where it is evident that the induced change in temperature is negligible.

VI. POWER CONSUMPTION OF THE SEMI-ACTIVE SYSTEM

The power needed to create the electrical fields is very low. Because the ERF is an isolator with a conductivity of 10^{-7} S/m, the currents flowing through the material are of the order 1 mA. This can be verified by measuring the electrical current during operation with different high voltages. The utilized laboratory-grade high voltage amplifiers support both voltage and current monitoring. The power consumption for steady-state, direct current operation can be calculated simply as the product of voltage and current,

$$P = UI = \frac{U^2}{R}. \quad (12)$$

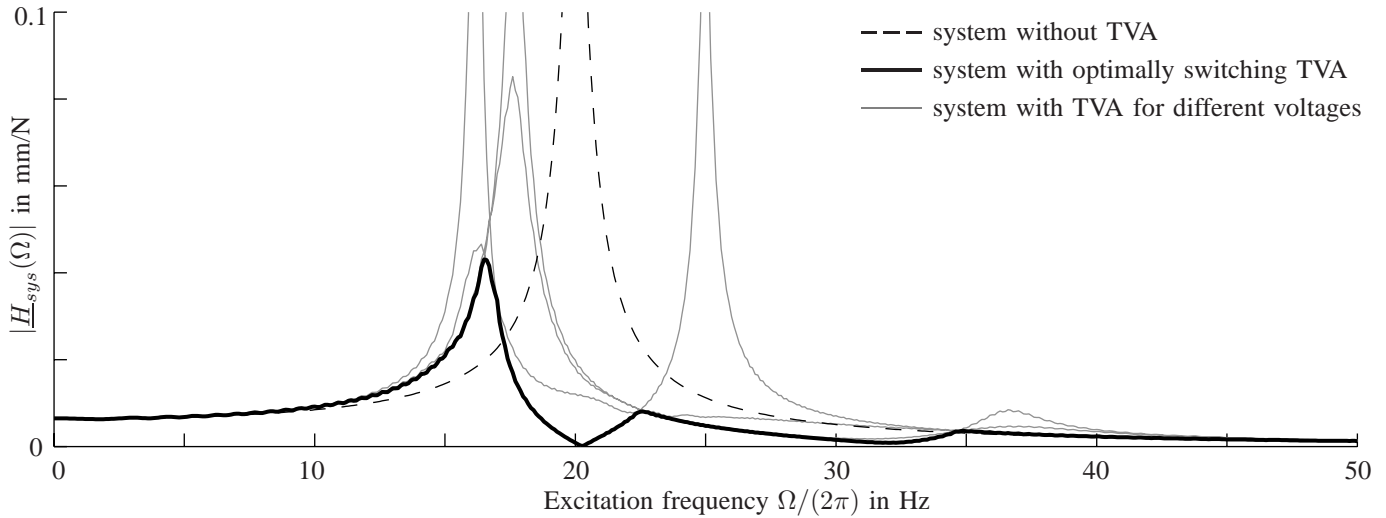


Fig. 10. Calculated system response of a one-degree-of-freedom system due to harmonic force excitation with the absorber prototype applied

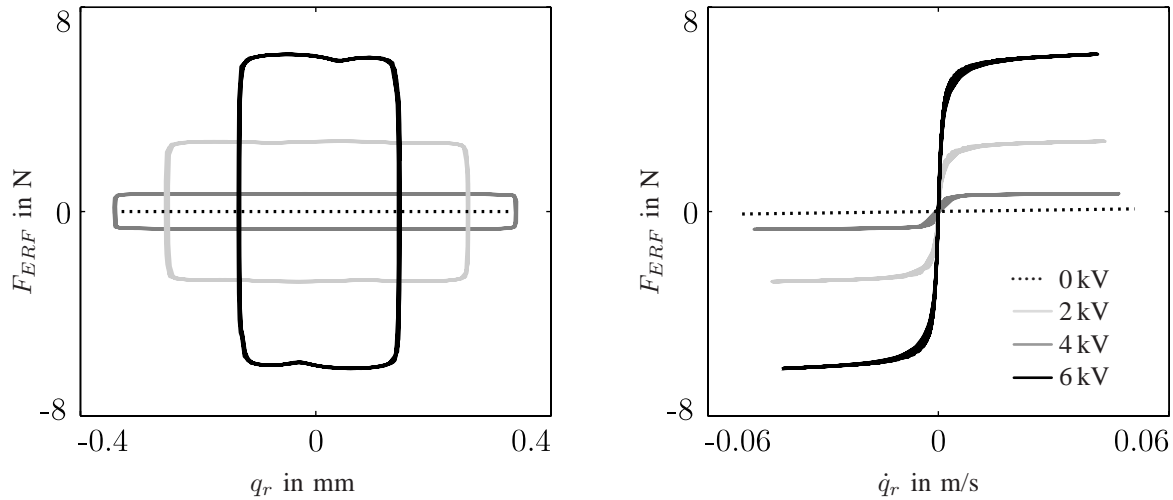


Fig. 11. **Case 1:** Calculated force-displacement and force-velocity diagrams for the ERF, high voltages U_2 from 0 to 6000 V applied, harmonic excitation at resonance frequency

The resistance of the ERF is assumed to remain constant and independent of factors such as air bubble entrainment, so that the resulting power consumption will be proportional to the square of the applied high voltage.

In addition to the power requirements of the ERF itself, the total power consumed by the high voltage generators coming from the power grid is measured simultaneously with a commercially available wattmeter. The result of this experiment for different high voltages is shown in Fig. 16.

As expected, the power consumption of the ERF is proportional to the square of the applied voltage. Even when 6000 V are applied, only 2 W of power are needed to maintain the electric field. Comparison with the 80 W of dissipated power results in a amplification factor of 40.

On the other hand, the high voltage generator has a much higher power consumption. In standby the high voltage generator already demands 8.6 W. When 6000 V are applied, the power consumption reaches almost 30 W. Even at maximum voltage, the efficiency of the high voltage generator is below

6%. For a complete semi-active system there will be additional power needs for sensor and controller. The overall efficiency of the resulting system is too low to result in a semi-active absorber with energetic advantages over active systems. For a real industrial application, an optimized high voltage generator is required.

VII. CONCLUSIONS

The objective of this paper was to discuss the efficiency of ER material as a semi-active tuning mechanism using a tunable vibration absorber prototype as an example. A prototype TVA and a corresponding mathematical model were presented in detail. The quality of the validated model is very high, allowing the calculation of the absorber performance on a virtual test system as well as the power dissipation in the ERF during operation. The prototype requires very little power to change its apparent natural frequency and damping. Compared to the damping evoked by the change in ER material behavior, the power provided by the high voltage generators is very small,

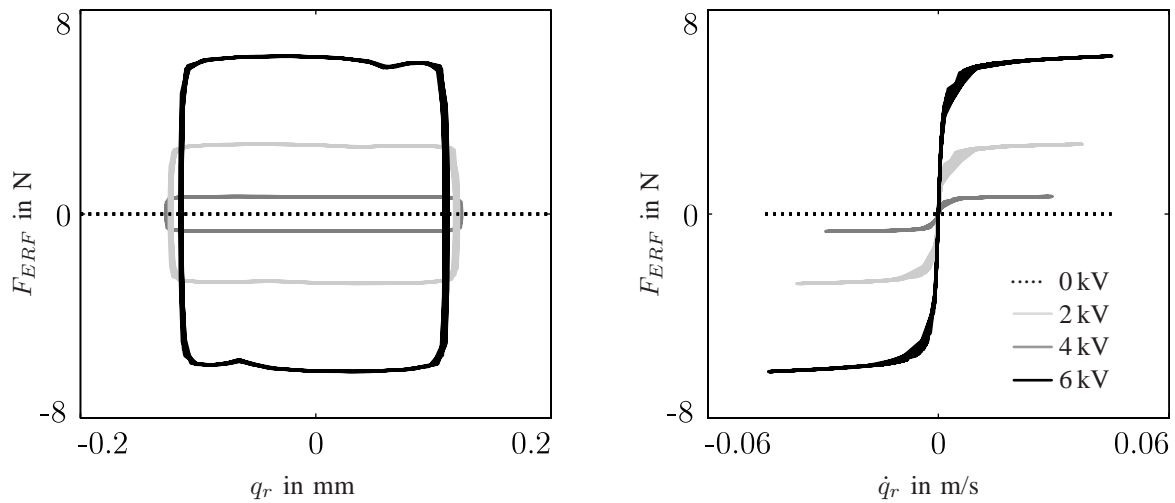


Fig. 12. **Case 2:** Calculated force-displacement and force-velocity diagrams for the ERF, high voltages U_2 from 0 to 6000 V applied, harmonic excitation at fixed frequency $\Omega/2\pi = 30$ Hz

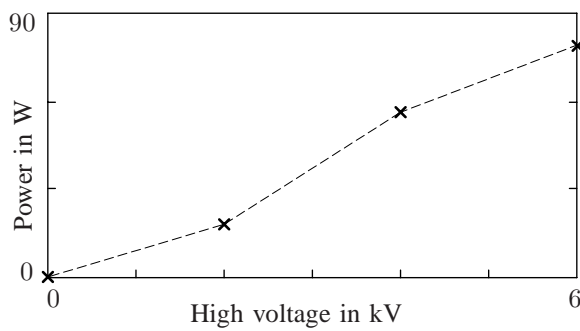


Fig. 13. Calculated power dissipation in the ERF in W for different applied high voltages U_2 , **Case 1**

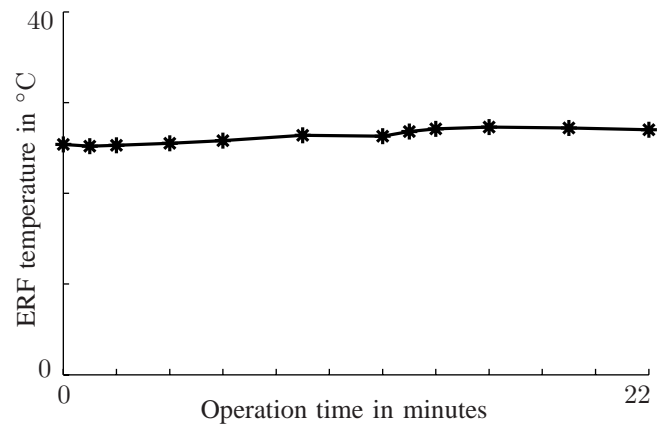


Fig. 15. Measured ERF temperature during operation with applied high voltage in resonance conditions in $^{\circ}\text{C}$

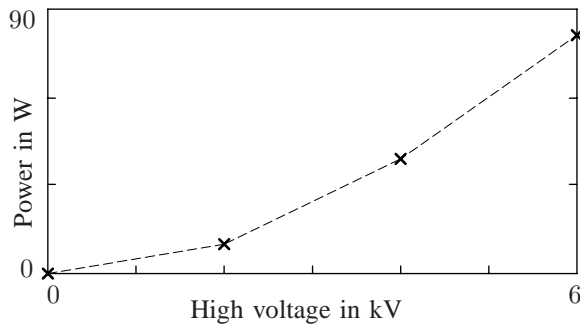


Fig. 14. Calculated power dissipation in the ERF in W for different applied high voltages U_2 , **Case 2**

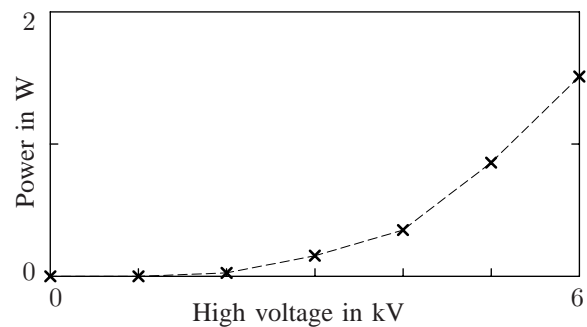


Fig. 16. Power consumption of the ERF in W for increasing high voltages

resulting in a high efficiency of the semi-active mechanism. Measurements of power consumption and numerical results for the corresponding power dissipation were presented. It was shown that the efficiency of the high voltage generators used in this study is too low for the semi-active absorber to exhibit its full potential. The power requirements of the high voltage generator can in part be attributed to the special voltage and current monitors supplied by the laboratory unit used for these measurements. Future development of semi-

active devices using ERF as an adjustment mechanism must incorporate this knowledge into the design process to ensure competitiveness.

VIII. ACKNOWLEDGEMENTS

The author would like to thank Prof. Dr.-Ing. Richard Markert for the fruitful discussions and his constant encour-

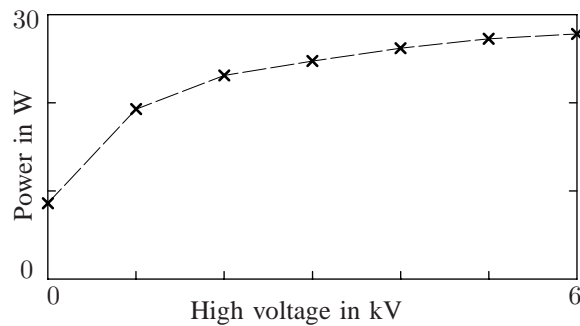


Fig. 17. Power consumption of the high voltage generator in W for increasing high voltages

agement and support throughout the years. Additionally, a special thanks goes to the companies TRW Automotive GmbH and Fludicon GmbH for their support of this research.

REFERENCES

- [1] H. Frahm, *Device for Damping Vibrations of Bodies*. US Patent No. 989,958, 1911.
- [2] J. P. Den Hartog, *Mechanical Vibrations*, New York, USA: McGraw-Hill, 1956.
- [3] A. Preumont, *Vibration Control of Active Structures, SMIA 179*, Berlin/Heidelberg, Germany: Springer-Verlag, 2011.
- [4] D. Hrovat, P. Barak and M. Rabins, „Semi-Active versus Passive or Active Tuned Mass Dampers for Structural Control,” *Journal of Engineering Mechanics*, vol. 109, pp. 691–705, 1983.
- [5] W. Winslow, *Method and means for translating electrical impulses into mechanical force*, U.S. Patent No. 2,417,850, 1947.
- [6] W. Winslow, „Induced fibrillation of suspensions,” *Journal of Applied Physics*, vol. 20, pp. 1137–1140, 1949.
- [7] W. A. Bullough and M. B. Foxon, „A proportionate coulomb and viscously damped isolation system,” *Journal of Sound and Vibration*, vol. 56, no. 1, pp. 35–44, 1978.
- [8] N. D. Sims, N. J. Holmes and R. Stanway, „A unified modelling and model updating procedure for electrorheological and magnetorheological vibration dampers,” *Smart Materials and Structures*, vol. 13, no. 1, pp. 100–121, 2004.
- [9] (2013, Nov.), LORD Corporation Website. [Online]. Available: <http://www.lord.com/our-company/history.xml>
- [10] H. Janocha and D. J. Jendritza, „Einsatzpotential von Elektorrheologischen Flüssigkeiten,” *Konstruktion*, vol. 46, pp. 111–115, 1994.
- [11] T. D. Truong and S. E. Semercigil, „A Variable Damping Tuned Absorber with Electro-Rheological Fluid for Transient Resonance of Light Structures,” *Journal of Sound and Vibration*, vol. 239, no. 5, pp. 891–905, 2001.
- [12] D. Sakamoto, N. Oshima and T. Fukuda, „Tuned sloshing damper using electro-rheological fluid,” *Smart Materials and Structures*, vol. 10, no. 5, pp. 963–969, 2001.
- [13] J.-H. Koo, *Using Magneto-Rheological Dampers in Semiactive Tuned Vibration Absorbers to Control Structural Vibrations*. PhD thesis, Virginia Polytechnic Institute and State University, USA, 2003.
- [14] M. H. Holdhusen, *The State-Switched Absorber Used for Vibration Control of Continuous Systems*. PhD thesis, Georgia Institute of Technology, USA, 2005.
- [15] Y. D. Choi, *Mechanical Properties of a Composite Beam Containing an Electrorheological Fluid*. PhD thesis, North Carolina State University, USA, 1991.
- [16] C. Hirunyapruk, *Vibration Control Using an Adaptive Tuned Magneto-Rheological Fluid Vibration Absorber*. PhD thesis, University of Southampton, England, 2009.
- [17] Y. Sun and M. Thomas, „Control of torsional rotor vibrations using an electrorheological fluid dynamic absorber,” *Journal of Vibration and Control*, vol. 17, no. 8, pp. 1253–1264.
- [18] N. Norrick, R. Markert and D. Plöger, „Analyse und Modellierung eines in elektorrheologischer Flüssigkeit arbeitenden Zweimassenschwingungstilgers,” *VDI-Berichte*, vol. 2093, pp. 73–81, 2010.
- [19] N. Norrick, R. Markert and R. Nicoletti, „Analysis and nonlinear modeling of a dual-mass tuned vibration absorber working in electrorheological fluid,” *XIV International Symposium on Dynamic Problems of Mechanics (DINAME 2011)*, Maresias, Brazil, 2011.
- [20] N. Norrick, „Application of a Nonlinear Semi-Active Tuned Vibration Absorber to an Automobile Substructure,” *International Conference on Sound and Vibration (ICSV19)*, Vilnius, Lithuania, 2012.
- [21] Z. Huang and J. H. Spurk, „Der elektroviskose Effekt als Folge elektrostatischer Kraft,” *Rheologica Acta*, vol. 29, no. 5, pp. 475–481, 1990.
- [22] J. Bauer, *Intelligenter ERF-Schwingungsdämpfer für Rotorsysteme mit großen Amplituden*. Fortschritt-Berichte VDI: Reihe 11 Band 346, Düsseldorf, Germany: VDI-Verlag, 2012.
- [23] N. Norrick, *Elektorrheologisch verstellbare Mehrfreiheitsgrad-Schwingungstilger*. Fortschritt-Berichte VDI: Reihe 11 Band 347, Düsseldorf, Germany: VDI-Verlag, 2013.

The Optimization and Sensitivity Analysis of Sandwich Plates

E. Kormaníková*¹, K. Kotrasová¹

¹Technical University of Košice, Civil Engineering Faculty, Slovakia

*eva.kormanikova@tuke.sk

Abstract—This paper presents the optimization and sensitivity analysis of a sandwich plate whose laminate facings' failure is predicted by applying the criterion of Tsai-Wu. A symmetric sandwich plate is optimized with the objective functions of maximizing the natural frequencies and maximizing the buckling load. The design variables are the fiber orientation of the individual outer layers and are computed by using the Sequential Linear Programming method and the Modified Feasible Direction method. The sensitivity analysis is similar, in principle, to the design optimization. In the sensitivity analysis the design variables are changed between their lower and upper bounds in a specified number of steps.

Keywords—Buckling Analysis, Free Vibration Analysis, Optimization, Sensitivity Analysis, Sandwich Plate, Tsai-Wu Criterion

I. INTRODUCTION

Material that is a mixture of two or more distinct constituents or phases is a composite material, in which must be fulfillment that all constituents have to be presented in reasonable proportions and have quite different properties from the properties of the composite material. One very important group of laminated composites are sandwich composites. Sandwich composites consist of two thin facings sandwiching a core. The facings are made of a material that has high strength (metals or fiber reinforced laminates), which can transfer axial forces and bending moments, while the core is generally made of lightweight materials such as foam, resins with special fillers, alder wood etc. The material used in a sandwich core must be resistant to compression and capable of transmitting shear [1].

In the present paper we optimize a symmetric sandwich plate with laminated angle-ply facings. The design variables are the fiber orientations of the laminated facings. The objectives of the design are the maximization of the natural frequencies and the maximization of the buckling load. The Tsai-Wu constraint must be satisfied in order to have a feasible design. Optimization problem is formulated as a nonlinear programming problem.

The sandwich plate is taken to be rectangular and simply supported. The static analysis is performed in two steps. First, a finite element method is used to determine the overall buckling load of the sandwich plate. Using FEM formulation [2, 12], the first ten buckling loads are solved numerically. The second part of the analysis is free vibration analysis. Within this analysis the first ten natural frequencies are solved.

The optimization and sensitivity of a composite plate are very important analyses for design of structures ranging from aircrafts to civil structures.

II. STATIC ANALYSIS OF SANDWICH PLATES

To formulate the governing differential equations for sandwich plates we utilize the similarity of the elastic behaviour between laminates and sandwiches within the first order shear deformation theory applied to sandwich plates. We restrict our considerations to symmetric sandwich plates with thin cover sheets. There are differences in the expressions for the flexural stiffness, coupling stiffness and the transverse shear stiffness of laminates and sandwiches [3]. Furthermore there are essential differences in the stress distributions.

The assumptions on the deformations are:

- For the sandwich thin cover sheets are valid Kirchhoff's assumptions on deformations. In-plane stress-strain state is accrued in the sandwich thin cover sheets.
- The sandwich core with the thickness h_2 transfers only shear stresses perpendicular to the mid-plane of the cover sheets. The needed material property is the shear modulus G_2 .
- All points in the normal line have the equal deflections $w_1 = w_2 = w_3 = w$.
- All layers are perfectly bonded.

We can write the shear deformations (Fig. 1) [4, 5] as follows

$$\gamma_{xz,2} = \left(\frac{u_{12} - u_{32}}{h_2} + \frac{\partial w}{\partial x} \right) = \left(\frac{u_1 - u_3}{h_2} + \frac{d}{h_2} \frac{\partial w}{\partial x} \right),$$

$$\gamma_{yz,2} = \left(\frac{v_{12} - v_{32}}{h_2} + \frac{\partial w}{\partial y} \right) = \left(\frac{v_1 - v_3}{h_2} + \frac{d}{h_2} \frac{\partial w}{\partial y} \right), \quad (1)$$

where d is the distance between the sheets' mid-planes.

$$d = h_2 + \frac{h_1 + h_3}{2}. \quad (2)$$

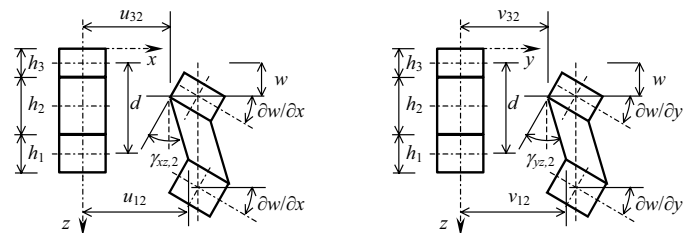


Fig. 1. Geometry of deformation

There are the normal forces (Fig. 2) in cover sheets $i = 1, 3$

$$N_{xi} = D_{Ni} \left(\frac{\partial u_i}{\partial x} + \nu_i \frac{\partial v_i}{\partial y} \right), \quad N_{yi} = D_{Ni} \left(\nu_i \frac{\partial u_i}{\partial x} + \frac{\partial v_i}{\partial y} \right),$$

$$N_{xyi} = \frac{D_{Ni}(1-\nu_i)}{2} \left(\frac{\partial u_i}{\partial y} + \frac{\partial v_i}{\partial x} \right),$$

where

$$D_{Ni} = E_i h_i / (1-\nu_i^2). \quad (3)$$

The bending moments and the shear forces in the skins (Fig. 2) we can write as

$$M_{xi} = -D_{Mi} \left(\frac{\partial^2 w}{\partial x^2} + \nu_i \frac{\partial^2 w}{\partial y^2} \right), \quad M_{yi} = -D_{Mi} \left(\nu_i \frac{\partial^2 w}{\partial x^2} + \frac{\partial^2 w}{\partial y^2} \right),$$

$$M_{xyi} = -D_{Mi} (1-\nu_i) \frac{\partial^2 w}{\partial x \partial y},$$

$$V_{xzi} = -D_{Mi} \left(\frac{\partial^3 w}{\partial x^3} + \frac{\partial^3 w}{\partial x \partial y^2} \right), \quad V_{yzi} = -D_{Mi} \left(\frac{\partial^3 w}{\partial y^3} + \frac{\partial^3 w}{\partial x^2 \partial y} \right),$$

where

$$D_{Mi} = E_i h_i^3 / 12(1-\nu_i^2). \quad (4)$$

The shear stresses in the core are written

$$\tau_{xz} = G_2 \gamma_{xz2} = \frac{G_2}{h_2} \left(u_1 - u_3 + d \frac{\partial w}{\partial x} \right),$$

$$\tau_{yz} = G_2 \gamma_{yz2} = \frac{G_2}{h_2} \left(v_1 - v_3 + d \frac{\partial w}{\partial y} \right). \quad (5)$$

The equilibrium equations for internal forces are the following

$$\frac{\partial N_{xi}}{\partial x} + \frac{\partial N_{xyi}}{\partial y} + \frac{\partial V_{xzi}}{\partial z} = 0, \quad \frac{\partial N_{xyi}}{\partial x} + \frac{\partial N_{yi}}{\partial y} + \frac{\partial V_{yzi}}{\partial z} = 0,$$

$i = 1, 3$

$$\frac{\partial V_{xz}}{\partial x} + \frac{\partial V_{yz}}{\partial y} + p = 0,$$

where

$$\frac{\partial V_{xz1}}{\partial z} = -\tau_{xz}, \quad \frac{\partial V_{xz3}}{\partial z} = \tau_{xz},$$

$$V_{xz} = \frac{\partial M_x}{\partial x} + \frac{\partial M_{xy}}{\partial y} + \frac{\partial V_{xz}}{\partial z}, \quad V_{yz} = \frac{\partial M_{yx}}{\partial x} + \frac{\partial M_y}{\partial y} + \frac{\partial V_{yz}}{\partial z},$$

$$\frac{\partial V_{xz}}{\partial z} = \tau_{xz} h_2, \quad \frac{\partial V_{yz}}{\partial z} = \tau_{yz} h_2. \quad (6)$$

To solve the unknown functions $u_1(x,y)$, $u_3(x,y)$, $v_1(x,y)$, $v_3(x,y)$, $w(x,y)$ it is necessary to set the boundary conditions for each boundary [9-11].

We have used the finite element method for solving the problem. The continuum was divided into a finite number of rectangular finite plate elements.

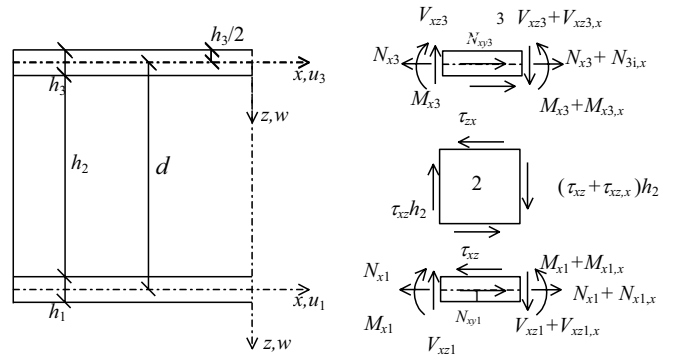


Fig. 2. Internal forces at the sandwich element in the (x, z) plane

III. FREE VIBRATION AND BUCKLING ANALYSIS OF SANDWICH PLATE

The equations to determine the natural frequencies of a symmetric sandwich panel are following

$$D_{11} \frac{\partial^2 \bar{\alpha}}{\partial x^2} + D_{66} \frac{\partial^2 \bar{\alpha}}{\partial y^2} + (D_{12} + D_{66}) \frac{\partial^2 \bar{\beta}}{\partial x \partial y} - \quad (7)$$

$$-k^s A_{55} \left(\bar{\alpha} + \frac{\partial w}{\partial x} \right) - I \frac{\partial^2 \bar{\alpha}}{\partial t^2} = 0,$$

$$(D_{12} + D_{66}) \frac{\partial^2 \bar{\alpha}}{\partial x \partial y} + D_{66} \frac{\partial^2 \bar{\beta}}{\partial x^2} + D_{22} \frac{\partial^2 \bar{\beta}}{\partial y^2} - \quad (8)$$

$$-k^s A_{44} \left(\bar{\beta} + \frac{\partial w}{\partial y} \right) - I \frac{\partial^2 \bar{\beta}}{\partial t^2} = 0,$$

$$k^s A_{55} \left(\frac{\partial \bar{\alpha}}{\partial x} + \frac{\partial^2 w}{\partial x^2} \right) + k^s A_{44} \left(\frac{\partial \bar{\beta}}{\partial y} + \frac{\partial^2 w}{\partial y^2} \right) - \quad (9)$$

$$-\rho_m h \frac{\partial^2 w}{\partial t^2} = 0,$$

$$\rho_m = \frac{1}{h} \sum_{k=1}^N \rho_k (z^{(k)} - z^{(k-1)}), \quad (10)$$

$$I = \frac{\rho_m h^3}{12} \frac{1}{3} \sum_{k=1}^N \rho_k (z^{(k)})^3 - (z^{(k-1)})^3,$$

where

k^s is the transverse shear deformation factor given by value 5/6 for quasi-isotropic laminate,

ρ_k is the mass density of the k^{th} layer.

For the simply supported plate let

$$w(x, y, t) = \sum_{m=1}^{\infty} \sum_{n=1}^{\infty} C'_{mn} \sin\left(\frac{m\pi x}{a}\right) \sin\left(\frac{n\pi y}{b}\right) e^{i\omega_{mn} t},$$

$$\bar{\alpha}(x, y, t) = \sum_{m=1}^{\infty} \sum_{n=1}^{\infty} A'_{mn} \cos\left(\frac{m\pi x}{a}\right) \sin\left(\frac{n\pi y}{b}\right) e^{i\omega_{mn} t},$$

$$\bar{\beta}(x, y, t) = \sum_{m=1}^{\infty} \sum_{n=1}^{\infty} B'_{mn} \sin\left(\frac{m\pi x}{a}\right) \cos\left(\frac{n\pi y}{b}\right) e^{i\omega_{mn} t}, \quad (11)$$

where

m, n – are integers only,

a, b – are the panel dimensions in x, y axis direction respectively,

ω_{mn} is natural angular velocity.

Substituting (11) into equations (7), (8) and (9) results in a set of homogeneous equations that are derived and used to solve the natural frequencies of vibration

$$\begin{pmatrix} L_{11}^{\text{eff}} & L_{12} & L_{13} \\ L_{12} & L_{22}^{\text{eff}} & L_{23} \\ L_{13} & L_{23} & L_{33}^{\text{eff}} \end{pmatrix} \begin{pmatrix} A_{mn} \\ B_{mn} \\ C_{mn} \end{pmatrix} = \begin{pmatrix} 0 \\ 0 \\ 0 \end{pmatrix}. \quad (12)$$

Matrix elements are given by the formulas

$$L_{11}^{\text{eff}} = L_{11} - \frac{\rho_m h^3}{12} \omega_{mn}^2, \quad L_{22}^{\text{eff}} = L_{22} - \frac{\rho_m h^3}{12 \omega_{mn}^2}, \quad (13)$$

$$L_{33}^{\text{eff}} = L_{33} - \rho_m h \omega_{mn},$$

where

$$\begin{aligned} L_{11} &= D_{11} \lambda_m^2 + D_{66} \lambda_n^2 + k^s A_{55}, \\ L_{12} &= (D_{12} + D_{66}) \lambda_m \lambda_n, \\ L_{13} &= k^s A_{55} \lambda_m, \\ L_{22} &= D_{66} \lambda_m^2 + D_{22} \lambda_n^2 + k^s A_{44}, \\ L_{23} &= k^s A_{44} \lambda_n, \quad L_{33} = k^s A_{55} \lambda_m^2 + \lambda_n^2, \end{aligned} \quad (14)$$

$$\lambda_m = \frac{m\pi}{a}, \quad \lambda_n = \frac{n\pi}{b}. \quad (15)$$

If the rotary inertia terms are neglected then $L_{11}^{\text{eff}} = L_{11}$, $L_{22}^{\text{eff}} = L_{22}$, and we obtain

$$\omega_{mn}^2 = \frac{(QL_{33} + 2L_{12}L_{23}L_{13} - L_{22}L_{13}^2 - L_{11}L_{23}^2)}{\rho_m h Q}, \quad (16)$$

$$Q = L_{11}L_{22} - L_{12}^2.$$

Also applies

$$\begin{aligned} A_{mn}^{\text{eff}} &= \frac{L_{12}L_{23} - L_{22}L_{13}}{Q} C_{mn}, \\ B_{mn}^{\text{eff}} &= \frac{L_{12}L_{13} - L_{11}L_{23}}{Q} C_{mn}. \end{aligned} \quad (17)$$

In a similar way the governing equations for buckling problems can be derived. In the matrix equations (12) only the differential operator L_{33}' is substituted by [6, 7]

$$L_{33}' - \left(N_1 \frac{\partial^2}{\partial x^2} + 2N_6 \frac{\partial^2}{\partial x \partial y} + N_2 \frac{\partial^2}{\partial y^2} \right). \quad (18)$$

IV. OPTIMIZATION PROCESS

Engineering design is an iterative process. The design is continuously modified until it meets evaluation and acceptance criteria set by the designer. Mathematical and empirical formulas and experience have been useful in the traditional design processes to verify the adequacy of designs. A fully automated design optimization and sensitivity is used when designers are trying to modify a design whose level of complexity exceeds their ability to make appropriate changes. It is not surprising that even what might appear as an extremely simple design task may easily be a real challenge to the designer during the decision-making process [8].

The design problem consists of determining the optimal fiber orientation $^k \theta$ where $k = 1, 2, \dots, N$, with N denoting the number of layers so as to satisfy the following objectives:

1. Maximization of the natural frequencies when the plate undergoes free vibrations
2. Maximization of the buckling load N when the plate is subjected to an in-plane load N .

Moreover, the design variables should satisfy the constraint

$$g_k = G_{01} \varepsilon_{1k} + G_{11} \varepsilon_{1k}^2 + G_{12} \varepsilon_{1k} \varepsilon_{2k} + G_{02} \varepsilon_{2k} + G_{22} \varepsilon_{2k}^2 + G_{44} \gamma_{12k}^2 - 1 < 0 \quad (19)$$

for $k = 1, \dots, N$,

where ε_{1k} , ε_{2k} , γ_{12k} are the strains in the principal material direction in the k -th layer. According to the Tsai-Wu criterion, which puts bounds on the values of the strains in the principal material directions, the failure envelope is an ellipsoid [3].

$$\begin{aligned} G_{01} &= F_{01} E_{11} + F_{02} E_{12}, \\ G_{02} &= F_{02} E_{22} + F_{01} E_{12}, \\ G_{11} &= F_{11} E_{11}^2 + F_{22} E_{12}^2 + F_{12} E_{11} E_{12}, \\ G_{22} &= F_{22} E_{22}^2 + F_{11} E_{12}^2 + F_{12} E_{22} E_{12}, \\ G_{12} &= 2E_{12} (F_{11} E_{11} + F_{22} E_{22}) + 2F_{12} (E_{12}^2 + E_{11} E_{22}), \\ G_{44} &= F_{44} E_{44}^2 \end{aligned} \quad (20)$$

$$F_{01} = \frac{1}{X_t} - \frac{1}{X_c}, \quad F_{11} = \frac{1}{X_t X_c},$$

$$F_{02} = \frac{1}{Y_t} - \frac{1}{Y_c}, \quad F_{22} = \frac{1}{Y_t Y_c},$$

$$F_{12} = -\frac{1}{2} \frac{1}{\sqrt{X_t X_c Y_t Y_c}}, \quad F_{44} = \frac{1}{S^2}, \quad (21)$$

where X and Y represent the ultimate strengths along and transverse to the fiber directions, respectively. The subscripts t and c are used to distinguish the tension and compression, respectively, S is the ultimate in-plane shear strength.

The optimization process is applied to the approximate problem represented by the polynomial approximation. The coefficients of the polynomial function are determined by the least squares regression.

For regression analysis the singular value decomposition is used. When the objective function and constraints are approximated and their gradients with respect to the design variables are calculated based on the chosen approximation, it is possible to solve the optimization problem.

One of the algorithms used in the optimization module is called the Modified Feasible Direction method (MFD). The solving process is iterated until convergence is achieved.

It is important to distinguish the iteration inside the approximate optimization from the loop in the overall optimization process. Fig. 3 shows the iterative process within each optimization loop.

Using the modified feasible direction method [8] the solving process consists on an iterative procedure which continues until convergence is achieved:

1. $q = 0$, $X^q = X^m$.
2. $q = q + 1$.
3. Evaluate objective function and constraints.
4. Identify critical and potentially critical constraint \bar{N}_c .
5. Calculate gradient of objective function $\nabla F(X_i)$ and constraints $\nabla g_k(X_i)$, where $k = 1, 2, \dots, \bar{N}_c$.

6. Find a usable-feasible search direction S^q .
7. Perform a one-dimensional search $X^q = X^{q-1} + \alpha S^q$.
8. Check convergence. If satisfied, make $X^{m+1} = X^q$. Otherwise, go to 2.
9. $X^{m+1} = X^q$.

The convergence of MFD to the optimum is checked by several criteria. There are the criterion of maximum of iterations and criterion of changes of objective function. Besides the previously mentioned criteria, the Kuhn-Tucker conditions necessary for optimality must be satisfied.

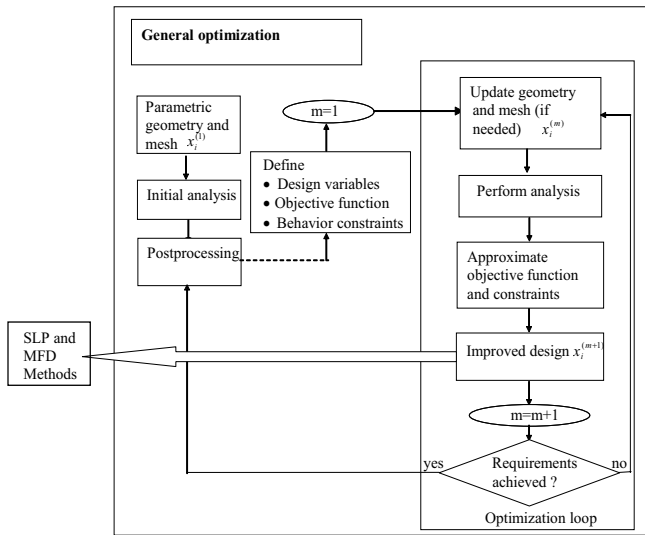


Fig. 3. General optimization process

A. Unconstrained Problems

The conditions degenerate to the case where the gradient of the objective function vanishes

$$\nabla F(\mathbf{X}) = 0. \tag{22}$$

It is noted that this condition is necessary but not sufficient for optimality. To ensure a function to be a minimum, the Hessian matrix must be positive-definite.

Also, the optimum is in a sense of relative optimum rather than global one. In general, the conditions to ensure a global minimum can rarely be demonstrated. If a global minimum is intended, one must restart the optimization process from different initial points to check if other solutions are possible. Fig. 4 shows the relative and global minima in the design space.

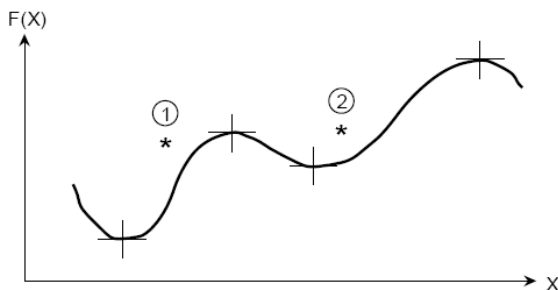


Fig. 4. Relative and global minima in the design space

B. Constrained Problems

The conditions of optimality are more complex. By using the Lagrangian multiplier method, we define the Lagrangian function as the following

$$L = F(X_1, \dots, X_n) + \sum_{j=1}^k \lambda_j h_j(X_1, \dots, X_n) + \sum_{j=1}^m \mu_j [g_j(X_1, \dots, X_n) + s_j^2] \tag{23}$$

where $\lambda_j, j = 1, \dots, k$ and $\mu_j, j = 1, \dots, m$ are Lagrangian multipliers and s_j is a slack variable which measures how far the j^{th} constraint is from being critical.

Differentiating the Lagrangian function with respect to all variables we obtain the Kuhn-Tucker conditions which are summarized as follows

$$\frac{\partial F}{\partial X_i} + \sum_{j=1}^k \lambda_j \frac{\partial h_j}{\partial X_i} + \sum_{j=1}^m \mu_j \frac{\partial g_j}{\partial X_i} = 0, \quad i = 1, \dots, n. \tag{24}$$

Stationarity with respect to $\lambda_j, j = 1, \dots, k$ gives the following restrictions

$$h_j(X_1, \dots, X_n) = 0, \quad j = 1, \dots, k. \tag{25}$$

Stationarity L with respect to s_j , gives $\mu_j s_j = 0$ and $\partial^2 L / \partial s_j^2$ for maximum of F .

The physical interpretation of these conditions is that the sum of the gradient of the objective function and the scalars λ_j times the associated gradients of the active constraints must vectorially add to zero as shown in Fig. 5.

The Kuhn-Tucker conditions are also sufficient for optimality when the number of active constraints is equal to the number of design variables. Otherwise, sufficient conditions require the second derivatives of the objective function and constraints (Hessian matrix) similar to the unconstrained one. If the objective function and all of the constraints are convex, the Kuhn-Tucker conditions are also sufficient for global optimality [8].

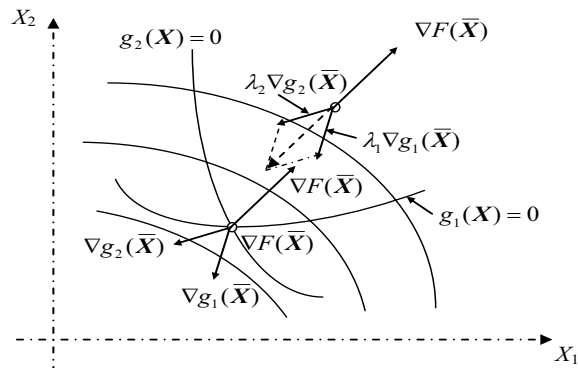


Fig. 5. Kuhn-Tucker conditions at a constrained optimum

We conducted a sensitivity analysis during and after the optimization process. A sensitivity study is the procedure that determines the changes in a response quantity for a change in a design variable. We used the global sensitivity, where design variables are changed between their lower and upper bounds in a specified number of steps.

The other algorithm for solving the nonlinear approximate optimization problem is called the Sequential Linear

Programming method (SLP). The iterative process of SLP within each optimization loop is shown below:

1. $p=0, X^p=X^m$.
2. $p=p+1$.
3. Linearize the problem at X^{p-1} by creating a first order Taylor Series expansion of the objective function and retained constraints
 $F(X) = F(X^{p-1}) + \nabla F(X^{p-1})(X - X^{p-1})$
 $g(X) = g(X^{p-1}) + \nabla g(X^{p-1})(X - X^{p-1})$.
4. Use this approximation of optimization instead of the original nonlinear functions:
 Maximize: $F(X)$
 Subject to: $g(X) \leq 0$ and $\bar{X}_i^L \leq X_i \leq \bar{X}_i^U$.
5. Find an improved design X^p (using the Modified Feasible Direction method).
6. Check feasibility and convergence. If both of them are satisfying, go to 7. Otherwise, go to step 2.
7. $X^{m+1} = X^p$.

Using the SLP method the solving process is iterated until convergence is achieved. Convergence or termination checks are performed at the end of each optimization loop in general optimization. The optimization process continues until either convergence or termination occurs.

V. TSAI-WU CRITERION

We can distinguish the failure between fiber failure (FF) and inter fiber failure (IFF). In the case of plane stress, the IFF criteria discriminates three different modes. The IFF mode A is when perpendicular transversal cracks appear in the lamina under transverse tensile stress with or without in-plane shear stress. The IFF mode B denotes the occurrence of perpendicular transversal cracks, but in this case they appear under in-plane shear stress with small transverse compression stress. The IFF mode C indicates the onset of oblique cracks when the material is under significant transversal compression [2].

The strength of a composite layer in any other direction can be evaluated on various failure criteria. The basic premise in predicting the failure of fiber-reinforced layers using the maximum stress and maximum strain criteria is the same as the one used for isotropic material. Failure is predicted when the maximum stress along the fiber or transverse to the fiber directions exceed the strength of the tension or compression.

A more general form of the Tsai-Wu failure criterion for orthotropic materials under plane stress assumption is expressed as

$$F_{01}\sigma_1 + F_{11}\sigma_1^2 + 2F_{12}\sigma_1\sigma_2 + F_{02}\sigma_2 + F_{22}\sigma_2^2 + F_{44}\tau_{12}^2 < 1 \quad (26)$$

The failure criterion for orthotropic material under strain assumption is expressed as

$$G_{01}\varepsilon_1 + G_{11}\varepsilon_1^2 + G_{12}\varepsilon_1\varepsilon_2 + G_{02}\varepsilon_2 + G_{22}\varepsilon_2^2 + G_{44}\gamma_{12}^2 < 1. \quad (27)$$

When $F_{12} = \frac{-1}{2X_1^2}$, the Tsai-Wu criterion is reduced to Tsai-

Hill criterion, and when $F_{12} = \frac{-1}{2X_1X_c}$ the Tsai-Wu criterion

is reduced to Hoffman criterion [3].

These failure criteria are used to calculate a failure index (F.I.) from the computed stresses and user-supplied material strengths. A failure index denotes the onset of failure, and a value less than 1 denotes no failure. The failure index according to this theory is computed using the following equation [2]

$$I_F = F_{01}\sigma_1 + F_{11}\sigma_1^2 + 2F_{12}\sigma_1\sigma_2 + F_{02}\sigma_2 + F_{22}\sigma_2^2 + F_{44}\tau_{12}^2. \quad (28)$$

The failure load factor is inverse value to the failure index.

VI. SOLUTION AND RESULTS

Solve the optimization and sensitivity of sandwich plate (Fig. 6) made of a 6-layer Boron-Epoxy laminated facings $[\theta/\theta-60/\theta+60]_s$ and polystyrene core. The thickness h of the laminate is 0.001 m. The material properties for laminate layers are given as:

$$E_1 = 194\text{GPa}, E_2 = 8.7\text{GPa}, G_{12} = 3.2\text{GPa}, \nu_{12} = 0.33, \rho = 2100\text{kg/m}^3$$

$$X_t = 1300\text{MPa}, X_c = 2000\text{MPa}, Y_t = 140\text{MPa}, Y_c = 300\text{MPa}, S = 90\text{MPa}.$$

The material properties for sandwich core are given as:

$$E = 42\text{MPa}, \nu = 0.3, \sigma_u = 1\text{MPa}, \rho = 150\text{kg/m}^3.$$

The plate is simply supported at all boundaries and loaded by a uniaxial uniform load (Fig. 6). Thickness h is for the facings and 8^*h is for the core (Fig. 7).

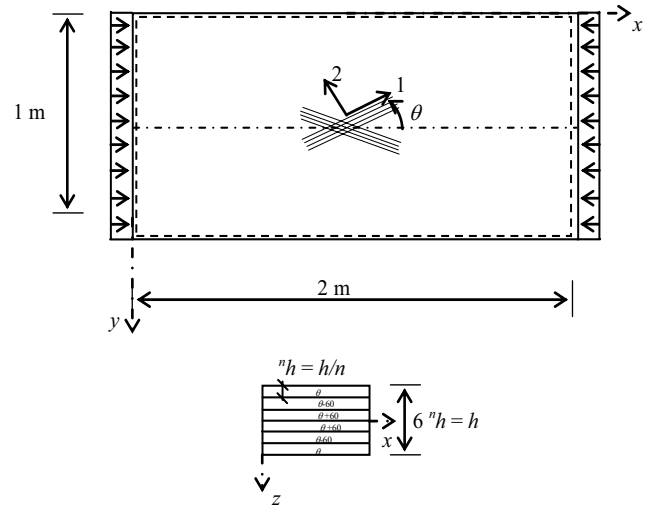


Fig. 6. Geometry of the sandwich plate and staff of facing layers

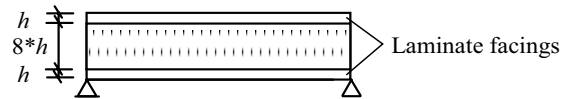


Fig. 7. Cross-section of sandwich plate

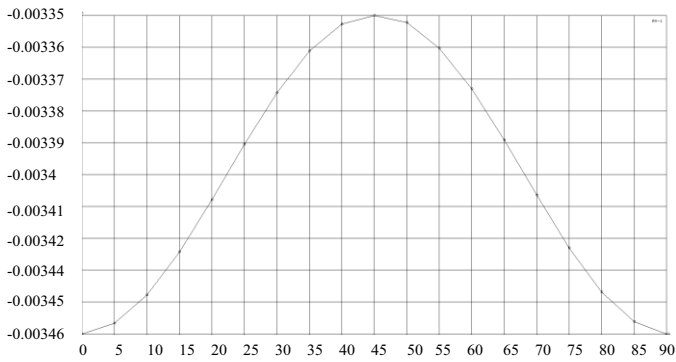


Fig. 8. Maximum F.I for changed angle orientation $0^{\circ} - 90^{\circ}$

TABLE I
FIRST 10 BUCKLING LOAD FACTORS

Eigen Value	Buckling Load Factor
1	12.79965
2	15.44049
3	19.73424
4	21.25276
5	29.79095
6	41.38276
7	54.31924
8	56.70496
9	57.96148
10	61.83806

TABLE II
FIRST 10 FREQUENCIES IN BUCKLING ANALYSIS

Frequency	Frequency [Hz]	Period [s]
1	60.1931	$1.66132 \cdot 10^{-2}$
2	72.1556	$1.38589 \cdot 10^{-2}$
3	93.6620	$1.06767 \cdot 10^{-2}$
4	98.7033	$1.01314 \cdot 10^{-2}$
5	137.297	$7.28349 \cdot 10^{-3}$
6	166.673	$5.29456 \cdot 10^{-3}$
7	245.163	$4.07892 \cdot 10^{-3}$
8	255.635	$3.91183 \cdot 10^{-3}$
9	163.688	$3.79237 \cdot 10^{-3}$
10	274.553	$3.64229 \cdot 10^{-3}$

TABLE III
FIRST 10 EIGEN FREQUENCIES IN FREE VIBRATION ANALYSIS

Frequency	Frequency [Hz]	Period [s]
1	47.9450	$2.08573 \cdot 10^{-2}$
2	77.1406	$1.29633 \cdot 10^{-2}$
3	126.157	$7.92660 \cdot 10^{-3}$
4	163.474	$6.11719 \cdot 10^{-3}$
5	176.255	$5.67361 \cdot 10^{-3}$
6	194.218	$5.14886 \cdot 10^{-3}$
7	195.647	$5.11124 \cdot 10^{-3}$
8	245.632	$4.07113 \cdot 10^{-3}$
9	286.601	$3.48917 \cdot 10^{-3}$
10	318.363	$3.14106 \cdot 10^{-3}$

9_00001 12.7997

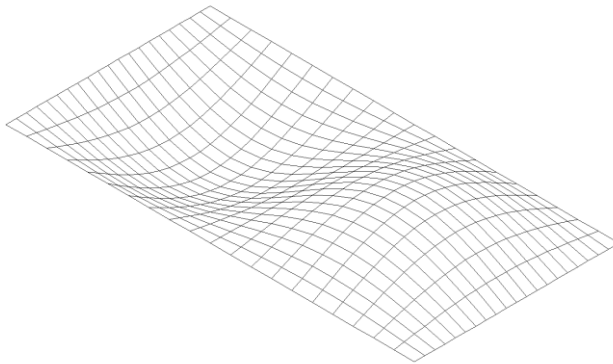


Fig. 9. Eigen mode for the first eigen value in buckling analysis after optimization

9_00002 19.7342

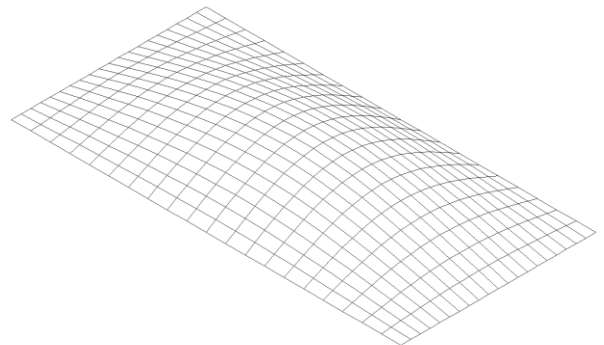


Fig. 11 Eigen mode for the third eigen value in buckling analysis after optimization

9_00003 21.2528

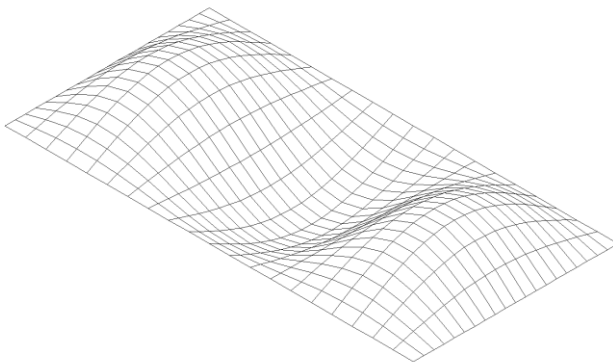


Fig. 10. Eigen mode for the second eigen value in buckling analysis after optimization

9_00004 274.553

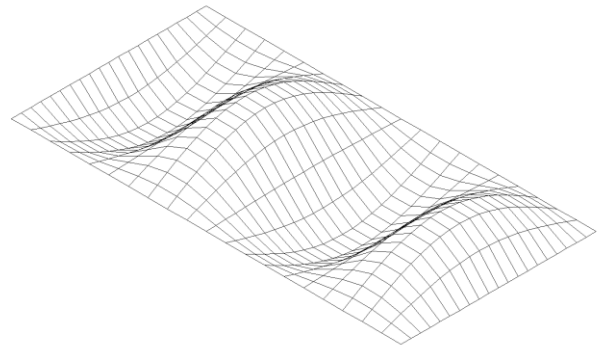


Fig. 12. Eigen mode for the fourth eigen value in buckling analysis after optimization

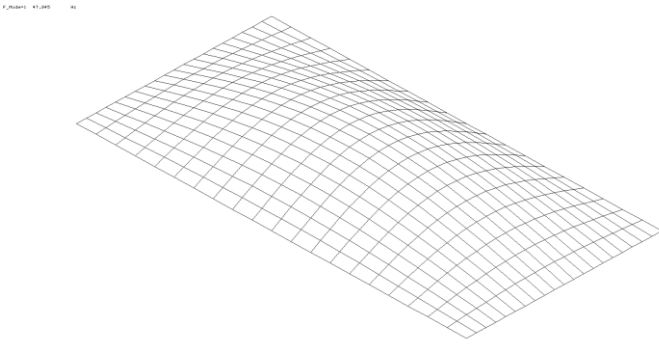


Fig. 13. First eigen mode in free vibration analysis after optimization

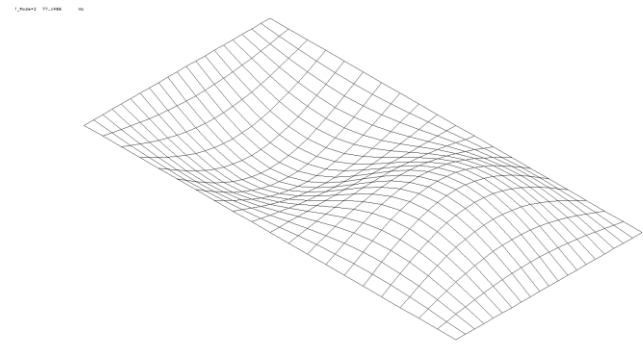


Fig. 14. Second eigen mode in free vibration analysis after optimization

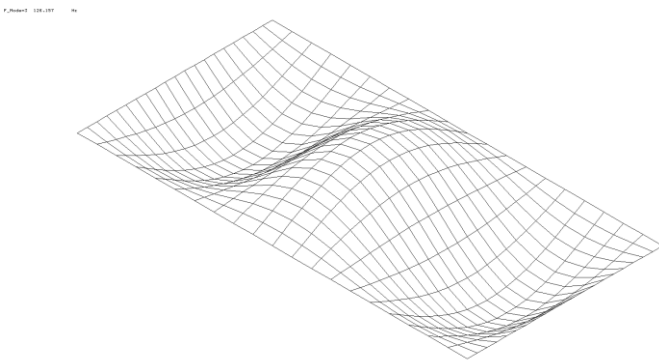


Fig. 15. Third eigen mode in free vibration analysis after optimization

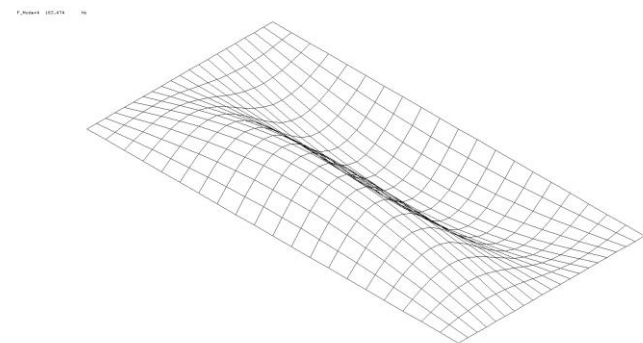


Fig. 16. Fourth eigen mode in free vibration analysis after optimization

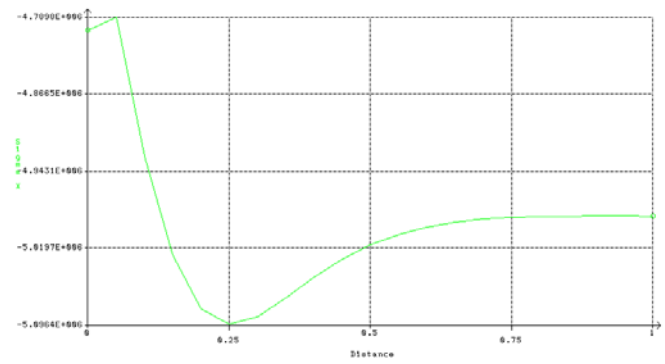


Fig. 17. Stresses σ_x for the bottom of the lower cover sheet along the mid-section

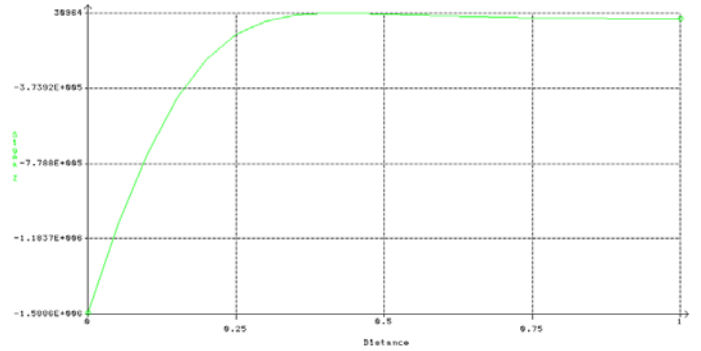


Fig. 18. Stresses σ_y for the bottom of the lower cover sheet along the mid-section

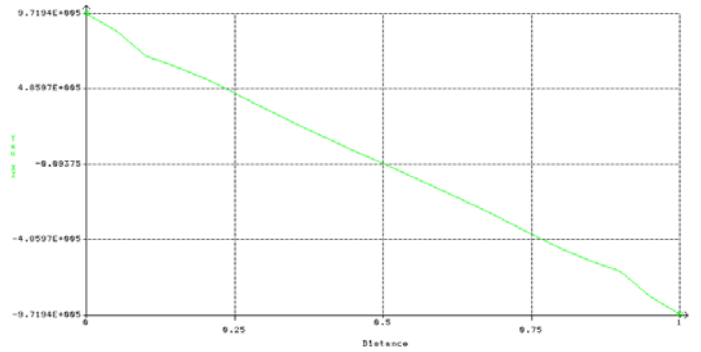


Fig. 19. Stresses τ_{xy} for the bottom of the lower cover sheet along the mid-section

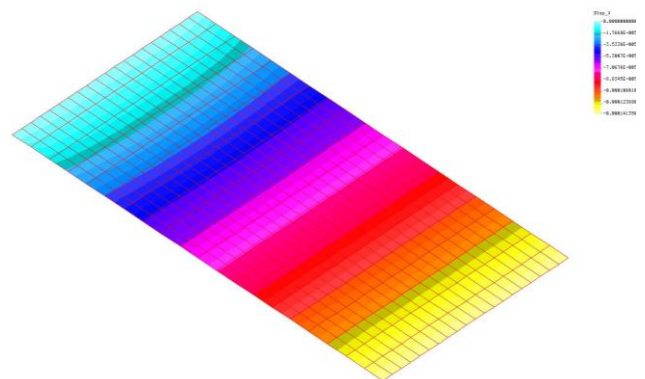


Fig. 20. Colour plot of displacements u

VII. CONCLUSION

From the sensitivity analysis (Fig. 8) one can see, that the fiber orientation of laminated facings $[\theta/\theta-60/\theta+60]_s$ has minor influence on the maximum failure index. The reason is the quasi-isotropic character of the laminate facings. Tsai-Wu criterion is violated, than failure load factor is 289.5. The results for the buckling factors are shown in Table 1. The first buckling load factor is 22.6 times minor than maximum failure load factor. The optimal design variable is $\theta = 45^\circ$. It means that fiber angle near 45° leads to the highest buckling load for a sandwich plate. Eigen modes in buckling analysis depend on fiber orientation and have another shapes than isotropic homogeneous plates. The buckling modes are symmetric to the symmetric axis in loading direction (Figs. 9-12). The first 10 frequencies in buckling and frequency analysis you can see in Table 2 and 3, respectively. The first ten frequencies in the buckling analysis are higher than in the free vibration analysis. Eigen modes in the buckling analysis are different than eigen modes in the free vibration analysis (Figs. 13-16). Within the static analysis there were calculated stresses σ_x , σ_y , τ_{xy} respectively (Figs. 17, 18, 19). In the Fig. 20 one can see the colour plot of displacements u in the static analysis.

The buckling and free vibration analyses of sandwich plates were done with continuity of their optimization and sensitivity analyses. There are significant differences between the behaviour of homogeneous and heterogeneous materials.

ACKNOWLEDGMENT

This paper has been supported by the project VEGA 1/0201/11 Progressive methods for the solution of structural elements made of composite and other new-age materials.

REFERENCES

- [1] H. Altenbach, J. Altenbach, and W. Kissing, *Structural analysis of laminate and sandwich beams and plates*, Lublin, 2001.
- [2] E. J. Barbero, *Finite element analysis of composite materials*, CRC Press, USA, 2007.
- [3] Z. Gürdal, R.T. Haftka, and P. Hajela, *Design and Optimization of Laminated Composite Materials*, J. Wiley & Sons, 1999.
- [4] E. Kormaníková, and I. Mamuzic, "Buckling analysis of a laminate plate," *Metalurgija*, vol. 47 (2), pp. 129-132, 2008.
- [5] M. Mihalíková et al., "Influence of strain rate on automotive steel sheet breaking," *Chemické listy*, vol. 105 (17), pp. 836-837, 2011.
- [6] J. Ďuraj, D. Tóthová, and E. Kormaníková, "Numerical analysis of elastic supported rectangular sandwich plate," in *Proc. Structural and physical problems of civil structures*, 2003, pp. 235-240.
- [7] J. Lovíšek, "Optimal design of sandwich plates with a rigid obstacle," *ZAMM-Z. angew. Math. Mech.* 69, vol. 7, pp. 191-201, 1989.
- [8] M. Žmindák, and M. Dudinský, "Computational Modelling of Composite Materials Reinforced by Glass Fibers," *Procedia Engineering*, vol. 48, pp. 701-710, 2012.
- [9] J. Králik, "Probability Nonlinear Analysis of Reinforced Concrete Containment Damage due to High Internal Overpressure," in *Proc. International Conference on Computing, Communications and Control Technologies: CCCT'04*, 2004, pp. 65-68.

- [10] I. Száva, M. Šejnoha, E. Kormaníková, et al., *Selected Chapters of Mechanics of Composite Materials III.*, Derc Publishing House U.S.A, 2013.
- [11] E. Carrera, "Theories and finite elements for multilayered, anisotropic, composite plates and shells," *Archives of Computational Methods in Engineering*, vol. 9 (2), pp. 87-140, 2002.
- [12] M. Šejnoha, and J. Zeman, "Micromechanical modeling of imperfect textile composites," *International Journal of Engineering Science*, vol. 46 (6), pp. 513-526, 2008.

Damping of structural vibrations by applications of elastomeric composite coatings

Fabrizia Ghezzi*¹, Xigeng Miao¹

¹Kuang-Chi Institute of Advanced Technology, Gaoxin Zhong 1st road, High Tech Industrial Estate, Nanshan District, Shenzhen, 518057 P.R. China

*fabriziaghezzi@gmail.com

Abstract— The use of elastomeric coatings for improving the ability of new or already existing structures to dissipate the energy originated from impact events has been investigated by many researchers in the past few decades and is today still an area of considerable interest. In recent years, polyurea has been successfully applied as a coating material for such a purpose and it demonstrates a remarkable improvement of the survivability of metallic and non-metallic structures subjected to severe shock and impact loading conditions. In this work we focused on improving the energy dissipation properties of this polymer by reinforcing it with two different classes of fillers, i.e. short fibers and ceramic particles. We present and discuss the results of the experimental characterization that we carried out on the reinforced polyurea composites and we compare them to those obtained from the pure polymer. The results conclude that these materials have higher performance than the pure polyurea and therefore can be used with remarkable benefits on the damage survivability of structures and components subjected to varying strain rate loading conditions.

Keywords— Coatings, Damping, Dynamic Mechanical Analysis, Differential Scanning Calorimetry, Elastomers, High Strain Rates.

I. INTRODUCTION

POLYUREA derives from the rapid reaction of an isocyanate and a polyamine based resin component. The first application of polyurea is dated 1948 [1]. In the early 1980's the two-component elastomeric polyurea was introduced in the market by Texaco as an improved material for the Reaction Injection Molding (RIM) technique [2-3]. Almost a decade later, the spray-on polymer technology [4] became popular and since then the technique has been used to produce polyurea coatings. Polyurea represents today one of the most successful materials developed for the coating industry. The success of polyurea in this field is certainly due to the fast curing even at very low temperatures, but also to the high chemical resistance, the high flexibility, high tear and abrasion resistance, tensile strength, as well as the low flammability and excellent durability if compared to polyurethanes. In addition to the above properties, polyurea presents high shear resistance and resilience and generally higher thermal properties such as high melting point and good stability at high temperature. At last, it shows excellent bonding properties to most materials, especially metals. Due to these characteristics, polyurea coatings have been introduced in many areas and applications.

Since the massive production, polyurea received considerable interest for coating structures and components exposed to severe dynamic and impulsive loadings caused by explosive events occurring either underwater or in air. The interest came from the observation that in the presence of such conditions the application of an elastomer coating on the structure improves the dissipation of the event's energy, thus limiting considerably the damage to the structure. Full scale explosive tests performed in the past demonstrated that coating the interior surfaces of the walls of a retrofitted building with polyurea could successfully prevent the failure, collapse and fragmentation of the structure, even in the case of a close detonation [5]. In some of these studies and experiments, fabrics like Kevlar, E-glass, carbon woven or mat material were used and bonded on the back side of structures such as structural walls by spraying polyurea on them. By doing so it was proven that the structure presented significantly enhanced shock resistance [6-7]. With particular attention to metallic structures, the dynamic response of circular and rectangular thin metallic plates to impulsive loads was studied both numerically and experimentally [8-12]. Based on these studies, it can be said that these layered systems demonstrate increased resistance at failure of the steel plate under high strain rate loading conditions preventing its fracture.

The phenomena involved to achieve the shock mitigation effects are very complex and many authors have conducted studies in order to clarify them. In the work [13] an explanation of the reason why the behavior of the elastomer while undergoing very high deformation is in favor of the dissipation of the impulsive energy was proposed. According to these authors the onset of failure of the thin metallic plate, i.e. the necking, is postponed in time due to the viscoelastic characteristic behavior of the elastomer and to its phase transition process from rubber-like to glass-like consistency; transition which always depends on the characteristics of the imposed loading conditions as confirmed elsewhere [14]. The microstructure and behavior of polyurea was proven to be, in fact, strongly pressure-strain dependent. In support to this explanation, it is in a recent study [15] that X-ray scattering tests conducted on impacted bi-layer (metal-polyurea) samples revealed that the mechanism of protection offered by the coating material is the strain hardening of the polyurea layer which augments the bilayer system's effective modulus and therefore increases the dissipation of the transmitted energy, retarding—in this way—the necking of the metallic plate. The

authors were able to demonstrate that the hardening of the polymer is – in part - dependent on the process according to which polyurea was made since the final molecular weights of the hard and soft segments that compose the polymer influence the response of the coating. At high strain rates of impact, in fact, the hard and soft segments that compose the polymer undergo a reformation and re-arrangement. Specifically, it is reported that the hard domains break under the high stress and reform in an oriented fiber form increasing the strain hardening and thus increasing the impact resistance. The nature of polyurea, composed by microphase soft domains with partially crystalline hard segments [16-18], contributes to the unique response of the material at high strain rate of impact.

A number of studies were then carried out to quantify at which extent stoichiometric variations of the polymer composition may influence its final mechanical properties. Several authors investigated the change of the properties of this polymer varying its composition [16-18] and also characterized its viscoelastic behavior both experimentally and numerically [13, 19-21]. Even though these contributions are valuable to understand the response of this polymer at low strain rates, it was observed that the resistance to ballistic penetration is unaffected by stoichiometric variations and with regard to polyurea coatings for impact energy mitigation their better performance requires radical changes in the structure and morphology than those that can be achieved by stoichiometric variations [18].

The objective of this work was to improve substantially the energy dissipation properties of polyurea under low or high strain rate conditions. From previous works in this field, it can be concluded that the response of the polymer at high strain rate is very different from the one at lower strain rates, since the transition from a rubbery to glassy state – phenomena that enhances the mitigation effects of the impact - only occurs at high impact energies and at these conditions stoichiometric variations have no effects on the performance of the polymer. It can be generally said that one way to improve the hardening and toughening of the polymer and its overall mechanical properties is by reinforcing it. Previous works on polyurea with nano-fillers are already present in the literature [22-23], however these works are not focusing on the effects of the fillers on the behavior of the polymer at high strain rate. In a study [24] target on the behavior of polyurea reinforced with multi-wall carbon nanotubes (MWCN), nanoclay particles and trisilanolphenyl-functionalized polyhedral oligomeric silsesquioxane (POSS) at high strain rates was presented. The experimental observations enabled the authors to conclude that no appreciable benefit on the performance at high strain rate can be seen by reinforcing polyurea with nano-fillers. Previous experimental work of the author [25-26] reported the enhancement of the energy dissipation of the reinforced polyurea coatings on metallic plates in impact events.

In this manuscript we report on the characterization of the quasi static and dynamic properties of a polyurea reinforced with two different types of fillers. The improved ability of dissipating energy presented by these materials was demonstrated by comparing their quasi static and dynamic behaviors with those of the pure elastomer. The characterization of these materials was conducted in order to

support the conclusions made in previous experimental observations where a few representative samples consisting of thin metallic plates coated with reinforced polyurea were subjected to high strain rate impact. The results demonstrated that these materials might have increased the survivability of the samples. As a consequence of those observations, a more comprehensive characterization of the properties was conducted on these materials. The evaluation of their dynamic behavior was considered as a way to quantify and characterize the damping ability of these materials as well as to verify the presence of potential changes in the segmental dynamics [24].

Unlike the work [24] where the increase of the toughness of polyurea was sought by adding nano-fillers which were then proven to disrupt the segmental dynamics of the polymer with no benefit to the performance of the material at high strain rate impact, our addition of a micron-size reinforcement was proved to have large benefit on increasing its overall mechanical properties and also increasing remarkably the survivability of the metallic component coated by such materials at high strain rate impact (10^4 s^{-1}). Based on these observations, we conclude that the optimization of the performance of the polymer for the mitigation of the impact energy is achieved by reinforcing it, but further studies are necessary to understand the additional mechanisms that are triggered in these composites when subjected to high strain rate loading conditions.

II. MATERIALS AND EXPERIMENTAL PROCEDURE

A. Material and samples preparation

The polyurea used in this work was derived from the combination of the following components: multifunctional Isonate® 143L [28], and high molecular weight oligomeric amine, Versalink® P1000 [29] in 1 to 4 proportions respectively. In this study, polyurea was reinforced with two types of fillers namely commercial milled E-glass fibers kindly provided by Hebei Yuniu Fiberglass Manufacturing Co., Ltd., with nominal fiber length of 0.3 mm and alumina powder ceramic grade (99.7 % purity) with $<1 \mu\text{m}$ diameter (typically of $0.3 \mu\text{m}$) from Zhengzhou Bihe Trade Co., Ltd. P.R. China. All the materials were used as received. The desired amount of fillers were first added to the blend resin component and the mixture was stirred for 6 hours in a three-neck round bottom reaction flask kept continuously under vacuum in order to evacuate the air bubbles present in the liquid. The isocyanate component was degassed in a separate glass flask, also under vacuum, and added to the rest of the mixture at later time. After the addition of the isocyanate, the whole mixture was stirred for about 15 seconds before being transferred into a teflon mould using a syringe. Once the degassing procedure was finalized, the overall material fabrication time required approximately 15 seconds for mixing all the components together and extra 20 seconds for casting the desired samples.

The samples consisted in un-confined quasi-static compression and dynamic mechanical analysis samples. Additional small specimens were used for scanning electron microscopy (SEM). The quasi static compression samples were obtained by pouring the mixed components into an open Teflon mould where cylindrical cavities of 10 mm height and

12 mm diameter were present. The dynamic mechanical analysis samples were cut from 1 mm thin and 6 cm by 6 cm sheets that were made by pouring the polymerizing mixture on a flat aluminum panel coated with a thin Teflon tape. To achieve the thickness of 1 mm and a flat surface finish, another aluminum plate coated with a 50 μm Teflon film was placed on top of the polymerizing mass squeezing it and letting it spread on the flat surface. Four precisely machined spacers of 1 mm thickness present at the corners supported the aluminum plate guaranteeing the uniform final thickness of the sample, i.e. 1 mm. Any part in Teflon which included the coating film and the mould parts were coated with mould release agent (by spraying) to facilitate the sample removal after their complete polymerization. In addition to these tests we also present a brief overview of some past achievements. The brief review of previous experimental results is necessary to highlight the reasons for which we conducted the study described in this work. In these past experiments, steel plates coated with polyurea composites made with the same fillers and concentrations were prepared using the same method as described in an earlier work [25-26]. The coating of the plates was realized by pouring the polymer mixture directly on a circular open cavity present on one side of the steel plates. The details of the geometry of this particular type of samples will be given in section 2.2.2 and Fig. 1. All the samples were left to cure for three weeks into an environmental chamber in a controlled level of humidity (kept below 10%). The two representative materials whose improved damping properties are discussed in this paper consist in a polyurea reinforced with 5.7% volume fraction (V_f) of alumina particles (Al_2O_3) and of 9% volume fraction of milled glass fibers respectively.

B. Materials characterization

1) Micrographic investigations

For the micro-structural analyses a scanning electron microscope, SEM, MIRA3 TESCAN, was used. All the samples were coated with a gold (Au) conductive film before they were loaded into the vacuum chamber of the SEM machine. Different magnifications were used. All samples were cut with a razor blade.

2) Impact tests

The high strain rate (10^4 s^{-1}) impact tests on a few representative samples were conducted on circular steel plates coated either with the pure or the reinforced polyurea. A few samples per material type (steel plates with either the milled glass fibers or the alumina reinforced polyurea coatings) were prepared to verify if the steel plates coated with these materials could sustain higher impact energies by showing no evidence of fracture after the impact event than steel plates coated with the pure polymer. The circular metallic plates, as the one shown in Fig. 1(a), were designed following the guidelines presented in the works [11, 30]. The samples presented a central section of about 1 mm thickness and 57 mm in diameter. This specific design was found to be optimal in order to avoid a dramatic shear failure at the edges of the plate. Some of the samples were coated with the pure polyurea and others with the reinforced polyurea. The coating process consisted in pouring the polymer into the inner section of the

sample via a syringe in such a way that a thick layer of polyurea materials fully covered the central part of the sample until reaching the level of the rim.

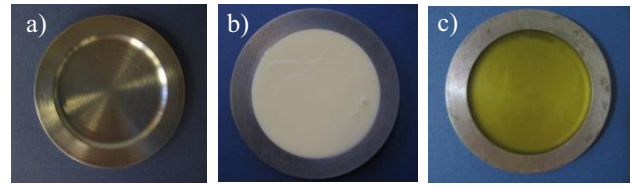


Fig. 1. Samples for impact tests: a) steel plate without coating; b) steel plate coated with alumina particle-polyurea ($V_f=5.7\%$) composite; and c) steel plate coated with milled glass-polyurea ($V_f=9\%$) composite {Picture is from the previous work [27]}.

To reproduce the effects caused by a shock wave due to an underwater explosion and transferred to a steel structure, a cylinder of polyurethane material was placed in front of the sample so that the impact force generated by a projectile could be transmitted first to the polyurethane and afterwards to the steel plate [11], Fig. 2.

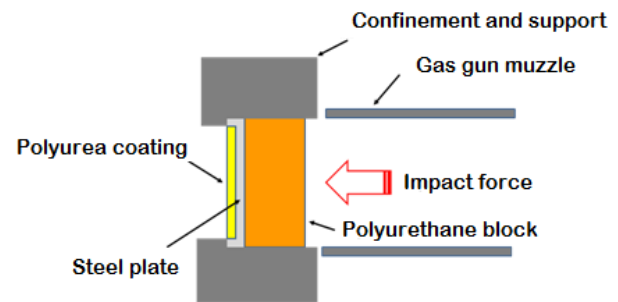


Fig. 2. Samples for impact tests: a) steel plate without coating; b) steel plate coated with alumina particle-polyurea ($V_f=5.7\%$) composite; and c) steel plate coated with milled glass-polyurea ($V_f=9\%$) composite {Picture from [27]}.

The sample with the elastomeric coating on the sample's surface opposite to the impact, as shown in the schematic of Fig. 2, was placed inside a cylindrical steel confinement which was part of the impact test apparatus, also known as gas gun. This cylindrical chamber presented at its end a cavity of a smaller diameter where the rim of the sample leaned against it in a simply supported mode leaving the central part, with the coating, exposed to the impact. The projectile was an aluminum alloy cylinder with known mass that was shot at a velocity which was accurately measured a posteriori by looking at the signals recorded using magnetic sensors located at known positions along the barrel. The projectile's impact velocities were calculated to be in the range of 60 to 74 m s^{-1} . The kinetic energy resulting from the test was simply calculated by the following equation:

$$E = \frac{1}{2} m_p v_p^2 \quad (1)$$

where m_p is the mass of the projectile and v_p the velocity measured by the sensors. The energy calculated by Eq. (1) was assumed to be fully absorbed by the sample during the impact and its effects on the materials were qualitatively estimated by comparing the failure modes observed. In particular, all the results were compared both with the typical failure mode of a circular steel plate without a coating and with the failure of a

steel sample coated with the pure polyurea. The failure mode was associated with the projectile's impact speed (m s^{-1}) and its kinetic energy (J cm^{-1}) divided by the thickness of the sample. The improvement, in terms of impulsive load bearing capability of the steel plate, was estimated by comparing the kinetic energy transferred to the plate and calculated by Eq. (1) normalized by the thickness of the sample. Overall, two samples per type were tested and two different coating thicknesses (3.7 mm and 2.2 mm) were considered. Even though the number of samples was not enough to derive some firm conclusions, the results of those experiments encouraged the work presented in this manuscript.

It resulted necessary to perform a comprehensive experimental materials characterization at low and high frequencies in order to fully investigate the behavior of these materials and the new phenomena that are responsible for the enhancement of the impact energy mitigation effects.

3) Unconfined compression

The unconfined compression tests were carried out using a universal mechanical testing machine, with the cross-head speed set at 0.1 mm s^{-1} . The cylindrical samples dimensions were measured before testing them.

4) Dynamic Analysis

The dynamic properties of the composite materials were measured by using a dynamic mechanical analyzer, (DMA), TA Instruments Q800. Milled glass fibers, alumina reinforced polyurea and pure polyurea samples were prepared for single cantilever beam tests. The average width of the samples was 6 mm while the length was fixed at 17.5 mm. The experiments were performed by imposing a fixed maximum strain of 1%. Storage and loss moduli of these materials were determined as a function of the temperature and the frequency. The damping of the materials was evaluated by observing the trend of the ratio of the loss modulus over the storage modulus, known also as the material's $\text{Tan } \delta$ [31]. The experiments were conducted by applying a temperature ramp from $-120 \text{ }^\circ\text{C}$ to $70 \text{ }^\circ\text{C}$ at the constant rate of $0.5 \text{ }^\circ\text{C min}^{-1}$ while the frequencies were changing from 0.1 to 20 Hz. Three samples per type were measured.

III. RESULTS AND DISCUSSION

A. SEM Analysis

The micrographic investigations were carried out on the samples 3 weeks after their preparation, allowing enough time for their curing. These investigations were necessary to explore the morphology of the material. Fig. 3 shows a section of a pure polyurea sample as fabricated. Based on this picture we assumed that all the samples fabricated were free of voids and presented no porosity. The cracks present in the sample and visible in these pictures are due to the cutting tool which inevitably produced some tearing forces at the edges of the material compound, damaging it. In Fig. 4(a), we can observe the typical morphology of a milled glass-polyurea sample. It can be noticed how the distribution of the short fibers – whose length was observed to be of the order of $300 \text{ }\mu\text{m}$ – is quite homogeneous as their random arrangement can be considered

as a 3D reinforcement. In Fig. 4(b), a magnified area around a fiber is shown. From this picture we can point out that the bonding between the fiber and the polymer looks poor. Notwithstanding the presence of porosity, the result of the impact tests revealed an improved resistance at high strain rate if compared to that displayed by the pure polymer. A further improvement of the properties of the material may be sought by choosing fibers with a sizing compatible with urea based polymers in order to enhance the bonding strength. In our case the fibers were chosen with no sizing. Such considerations though will need to be further investigated and experimentally proven. Finally, Fig. 5 presents the microstructure of an alumina-polyurea composite sample. The particles, which are of nanometer size, are present in the polymer in aggregates well distributed in the material. The bonding of these particles aggregates with the polymer seems to be quite good. The particles, in fact, look fully embedded into the polymer.

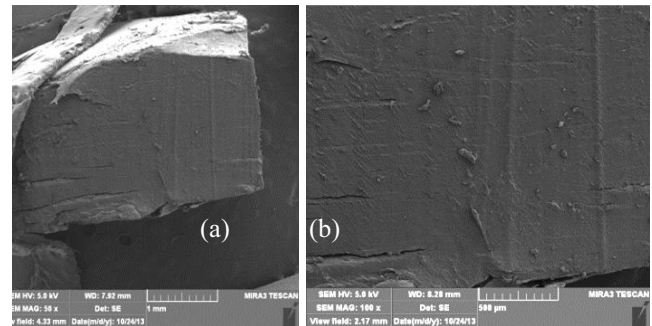


Fig. 3. The two SEM pictures present the inner appearance of a sample of pure polyurea. The material appears as dense and does not display any internal porosity. The cracks present in the small samples are due to the cutting procedure which induced some inevitable tearing.

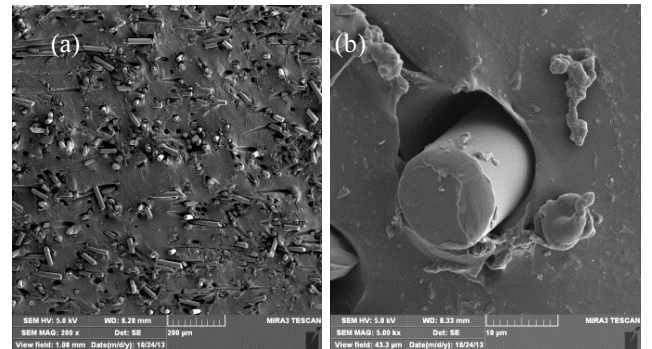


Fig. 4. The two SEM pictures are taken on the same sample of milled glass fiber polyurea. a) The fibers are randomly distributed in the sample, providing a 3D reinforcement. b) The diameter of the fiber is around 12 microns and the bonding of the polymer to the fiber seems to be poor

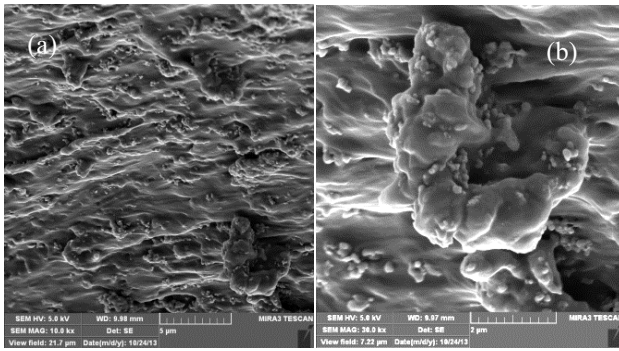


Fig. 5. The picture shows the morphology of one alumina polyurea sample. It can be observed how the nano-particles are present in the material in larger agglomerates. These agglomerates, however, seem to be homogeneously distributed in the material.

B. Impact tests

From the results of the impact tests it was first confirmed that a layer of polyurea backing a steel plate impacted with the same kinetic energy (per unit thickness) as the one that induced a dramatic failure of a bare steel plate significantly improved the absorption of the impact energy and, in all cases, prevented the failure of the sample. It is necessary to observe that the amount of fillers added to the polymer, is very small to appreciate any consistent change of weight for the entire sample as a consequence, inertia effects may be not claimed in this work partly responsible for the introduction of the improvements recorded during these tests. Said so, a dramatic failure such as the one shown in Fig. 6(a) was attributed to samples, with or without a coating, where a large central opening was displayed after the impact. A moderate failure, such as the one in Fig. 7(a), was attributed to those cases where the steel plate after the impact was highly deformed and presented evidence of cracks at the center.

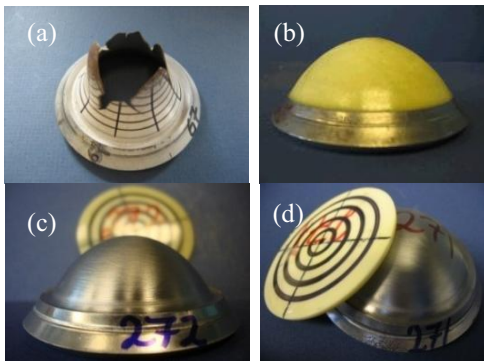


Fig. 6. Comparison of the impact results of some representative samples with 3.77 mm coating thickness: a) failure of steel plate S67 without coating at $15,347 \text{ J cm}^{-1}$ as reported in previous experimental results [11]; b) milled glass polyurea backing the steel plate MG249 impacted with the energy of $16,573.7 \text{ J cm}^{-1}$; c) milled glass fiber polyurea coating the plate MG272 impacted with $20,805 \text{ J cm}^{-1}$ energy; d) alumina reinforced polyurea coating the plate AL271 impacted with 21000 J cm^{-1} energy {Picture from [27]}.

No failure was instead attributed to those samples which presented a large deformation but no evidence of cracks as shown in Fig. 6(b), 6(c), 6(d) and Fig. 7(b). In Fig. 6(a), the reference steel sample impacted with the kinetic energy of $15,347 \text{ J cm}^{-1}$ and the correspondent projectile's speed of 62.18 m s^{-1} , displayed a severe failure, while the sample

coated with the milled glass fiber-polyurea shown in Fig. 6(b) displayed high deformation but no fracture when impacted with a energy level of $16,573.7 \text{ J cm}^{-1}$ and a projectile's speed of 63.34 m s^{-1} . In this specific case, Fig. 6(b), in addition to the improved impact resistance, the milled glass fiber-polyurea composites demonstrated the unique ability of remaining perfectly attached to the surface of the plate after the shock event. The effect may find an explanation in the high toughness that was observed to characterize this material, as reported in the next section. The highest impact resistance was displayed by samples coated with the alumina reinforced polyurea. In fact, as shown in the Fig. 6(d) one of these samples survived the impact after being shot with the energy of $21,000 \text{ J cm}^{-1}$ and the correspondent projectile's speed of 72.159 m s^{-1} . This was the highest impact energy recorded in these experiments. No steel plate coated with the pure polyurea or the milled glass fiber-polyurea survived at the same impact energy. A comparison made with the failure of a sample with the pure polyurea coating is presented in Fig. 7. The plate coated with the pure polyurea, Fig. 7(a), presented a moderate damage at impact energy of $17,945 \text{ J cm}^{-1}$ and projectile's speed of 66.26 m s^{-1} , while the plate coated with the milled glass fiber polyurea, in Fig. 7(b), survived when impacted with energy of $19,272 \text{ J cm}^{-1}$ and projectile's speed of 68.95 m s^{-1} . Once again, the reinforced polyurea coatings seemed to increase the survivability at impact of these layered systems.

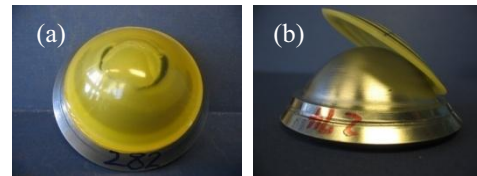


Fig. 7. Two representative samples where the thickness of the coatings was 2.2 mm. a) Moderate failure of steel plate coated with pure polyurea at impact energy of $17,945 \text{ J cm}^{-1}$; b) milled glass-polyurea coating a steel plate impacted with the energy $19,272 \text{ J cm}^{-1}$.

Overall, the improvement in terms of impact resistance of the samples was estimated to be 27% higher if compared to tests conducted on bare steel plates and 15% higher with respect to plates coated with the pure polyurea. The improvement was observed to be consistent for samples with two different coating thicknesses, i.e. 3.7 mm and 2.2 mm.

It can be argued that more experiments are necessary to confirm the improvement and some of the results can be questioned due to the small number of samples tested. However, these encouraging results gave a qualitative idea of the benefit that these materials may have over the pure polymer and suggested a more comprehensive characterization of the properties as presented in the following sections of this manuscript. It is important to add that, in these earlier studies, other types of reinforcement, such as flakes and longer fibers (both of the order of 1 cm in size), was used but with no or even negative effects on the performance of the coating at the same strain rates of impact. The works on the microphase composition of polyurea and the observations made on its behavior [18] along with these experiments brought the authors to assume that the hardening of the polymer through

addition of a filler which is big enough to not compromise the dynamics of the soft and hard segments at high strain rate [24] but smaller compared with the wavelength of the propagating pulse, could be a successful method for increasing the high and low strain rate energy mitigation ability. Based on previous findings we observed in fact that fillers with one dimension of the order 1 μm (or larger) did not have any effect on the mitigation of the impact energy; on the contrary, the filler probably acted as a stress concentrator and favored an earlier failure. This seems to imply that there exists an optimal size (and shape) of the filler along with optimal mechanical properties that can be found to enhance the performance of the polymer when subjected to high strain rates of impact. For lower strain rates and general mechanical properties characterization, the homogenization of the material properties based on the effective medium theory [32-33] leads to the conclusion that the reinforcement improved the overall materials mechanical properties with respect to those of the pure polymer. A comprehensive quantification of the improvement in terms of material dynamic properties was sought and the results of the measurements are reported in the following sections.

C. Compression tests

In Fig. 8 the curves for the pure polyurea and the polyurea-composites compressive behavior are presented. The curves are derived from the experiments conducted using a universal mechanical testing machine with cross-head speed set at 0.1 mm s^{-1} (low strain rate). The only remarkable fact is the very different toughness that characterizes and differentiates the polyurea composites from the pure polyurea. It can be observed in fact that the amount of energy (the area below the stress-strain curve) that can be absorbed by the two reinforced materials is much larger than that that can be absorbed by the pure polymer. Even though at the increasing of the strain rate the materials will behave differently [20], we can assume that the polyurea-composites will preserve the higher toughness characteristic.

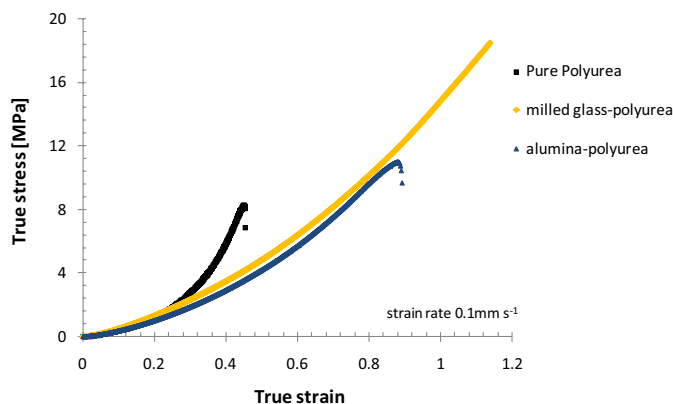


Fig. 8. Results of the compression tests conducted on samples of pure polyurea, milled glass-polyurea and alumina-polyurea composite at the strain rate of 0.1 mm s^{-1} .

The assumption is well supported by the experimental results obtained in high strain rates of impact. Particularly, the high deformability of the milled glass-polyurea composite combined with higher toughness can be considered as one of

the reasons for the higher survivability of the metallic-milled glass polyurea coating bilayer system at impact, Fig. 6(b).

D. Dynamic Analysis

For materials characterized by a viscoelastic behavior, such as in the case of most polymers and their derived composites, the evaluation of the damping efficiency is generally done by measuring the material loss modulus. Viscoelastic materials are in fact characterized by a modulus (in tensile, bending or shear loading conditions) composed of two parts, i.e. the real part known as the storage modulus which measures the energy stored by the material only by the elastic portion of its behavior; the imaginary part, i.e. is the loss modulus, which indicates the energy dissipated by heat [31]. The materials dynamic behaviors at different frequencies are shown in Fig. 9-13. It is necessary to point out that these tests were conducted at fixed imposed small strain and varying only the frequency of the load and the test temperature. Additional tests should be carried out in future studies to verify the effects in reinforced polyurea by varying the filler concentration [34].

Fig. 9 and 10 display the behavior of milled glass fiber-polyurea composite (named MG for convenience), and alumina-polyurea composite (AL) compared with those of the pure polymer. For clarity the plots show the behavior of these materials only at the selected frequencies of 0.1, 1, and 10 Hz.

To highlight their different behaviors we compared the dynamic behavior of both polyurea composites with that of the pure polyurea as shown in Fig. 11, while in Fig. 12 we report the trend of the ratio of the loss modulus to the storage modulus (i.e. the $\text{Tan}\delta$) which better presents the increased damping ability of a material. In fact, the higher $\text{Tan}\delta$ value the higher the part of the modulus that is responsible for the dissipation of the energy transferred to the material.

From Fig. 9 to 12 we can observe how the storage modulus of the polyurea at low temperature is remarkably higher, up to 30%, when the material is reinforced. At the same time, the loss modulus increases in the case of the reinforced materials up to almost 20% if measured at the peak displayed by its trend. The peak value observed for the trend of the loss modulus occurs at the glass transition temperature of the material [31]. The plots in Fig. 11(b) are proving information on the glass transition temperature of these materials. As it can be noticed, there is no appreciable change in the value of the glass transition temperature (from glass to rubber like behavior) of these materials.

The ratio of the loss modulus to the storage modulus ($=\text{Tan}\delta$) whose trend is shown in Fig. 12, can be used as an index of the energy dissipation ability of these materials. From these measurements, and particularly by looking at the behavior of these materials at the same frequency, it is clear how the damping properties of the two reinforced polyurea composites were higher than that of the pure polyurea and the improvement became really significant at frequencies above 5 Hz.

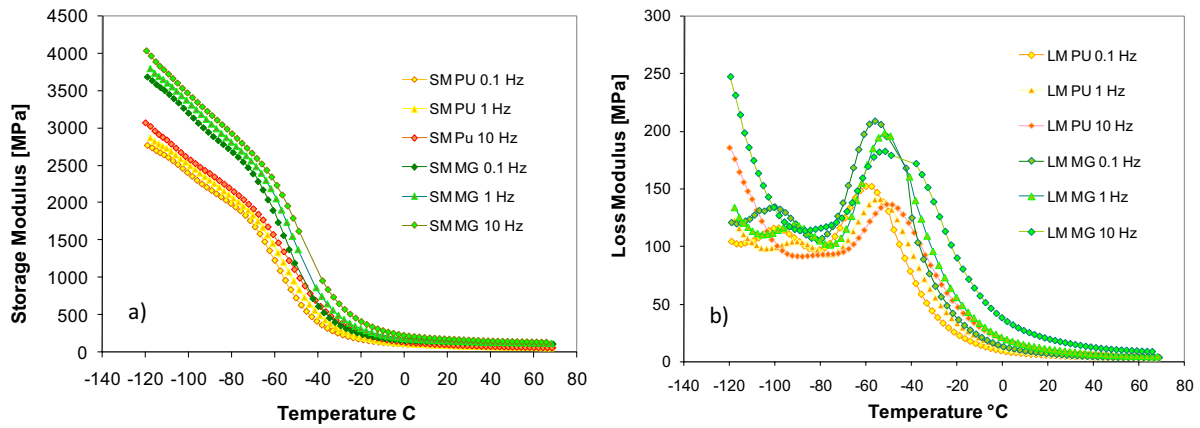


Fig. 9. Results of the dynamic mechanical analyses: a) storage modulus and b) loss modulus of pure polyurea (PU) compared with those of the milled glass fiber reinforced polyurea (MG), plotted at the selected frequencies of 0.1, 1 and 10 Hz.

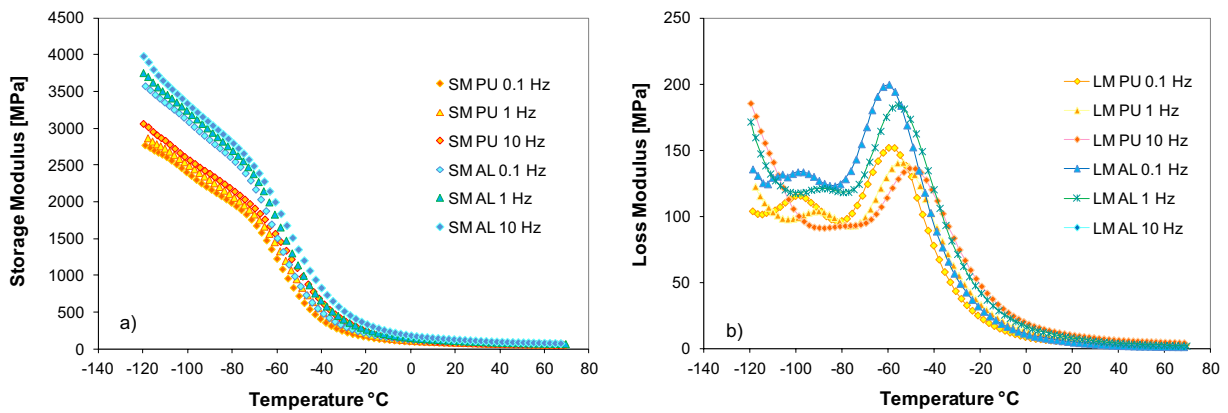


Fig. 10. Results of the dynamic mechanical analyses: a) storage modulus and b) loss modulus of polyurea (PU) compared with those of alumina-polyurea composite (AL) plotted at the selected frequencies of 0.1, 1 and 10 Hz.

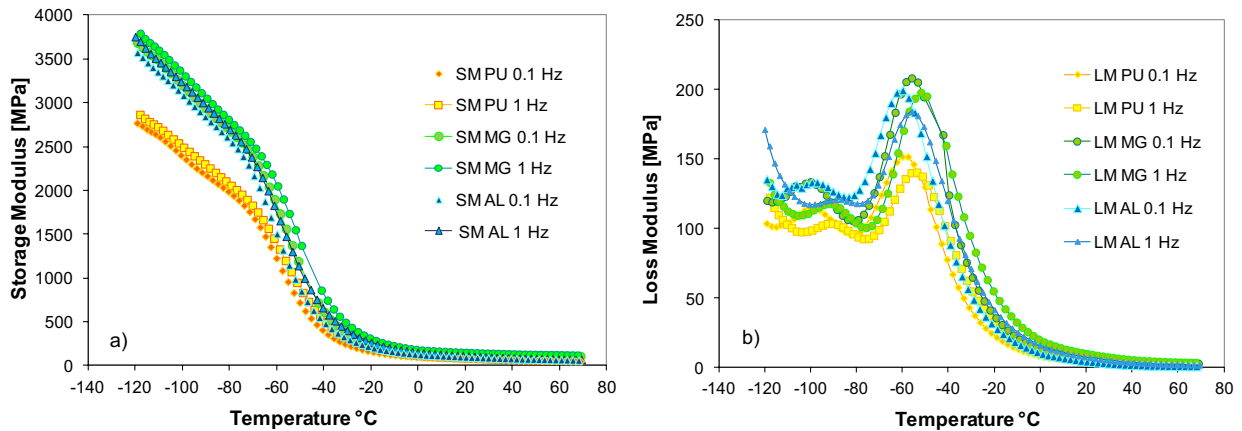


Fig. 11. Dynamic properties of the reinforced polyurea compared with the pure polyurea: a) storage modulus and b) loss modulus of polyurea (PU), milled glass-polyurea (MG) and alumina-polyurea composite (AL), plotted at the selected frequencies of 0.1 and 1 Hz for clarity.

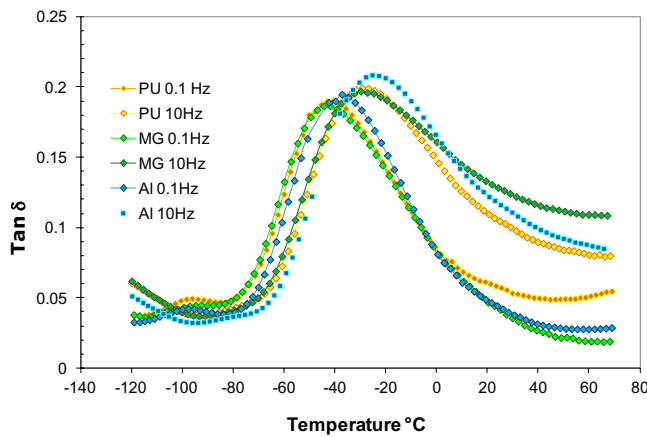


Fig. 12. Tan δ of the milled glass fiber and alumina polyurea composites compared with those of the pure polyurea at the selected frequencies of 0.1 and 10 Hz.

By considering the storage modulus, it is also evident how the strength of these composite materials increased substantially (in the range of 30%) if compared with that of the pure polyurea. We can therefore conclude that the dynamic response of the polyurea coatings subjected to high frequency pulses, like a shock impulse caused by a close detonation underwater, may be improved by using a polyurea coating resulting from the addition of a proper amount and type of filler. In fact, the heterogeneity of the microstructure and the toughening of the material by addition of the filler not only is in favor of the high dissipation abilities at low strain rates but may be also in favor of the higher energy mitigation effects occurring at high strain rates, supporting the results obtained from the impact tests.

IV. CONCLUSIONS

The behavior at high strain rates of impact and the quasi static and dynamic characterization at low frequency and low strain rates of a reinforced polyurea elastomer were presented in this work. Specifically, the improved damping properties of the polyurea were obtained by reinforcing the polymer with milled glass fibers and alumina particles. In a previous experimental investigation, a few steel samples coated with the pure polyurea and with the reinforced polyurea were impacted by a projectile whose speed was in the range of 60 to 75 m s⁻¹. From the observations made on the failure modes of the bi-layer system (steel plates and polyurea coatings) subjected to impact we concluded that when a thin layer of the reinforced polyurea material was backing a steel plate and the plate was then impacted with the same kinetic energy (per unit thickness) as the one that induced a dramatic failure of a steel plate coated with the pure polyurea, the plate presented a high deformation but did not fail. The explanation of these results was given by assuming that the energy dissipation ability of the material increased considerably by adding the fillers. The confirmation of this assumption was obtained by characterizing the dynamic properties of these materials. From the presented experimental study we can extract some important conclusions:

- The compression behavior of these materials shows that the polyurea composites are characterized by much higher toughness. This property, i.e. the ability of the material to store the energy before failure, is in support of the observed beneficial effects on the increase ability of mitigating the impact energy. These materials in fact display higher deformation ability, characteristic which was observed during the impact tests.
- The loss and storage moduli of milled glass fibers and alumina-polyurea composites are generally higher than that of the pure polyurea. The increase is remarkable at low temperature and particularly close to the glass transition region but the improvement can be clearly noticed also at temperatures above 20 °C. The dynamic behavior of the loss modulus characterizes the viscoelastic behavior of the material and indicates the ability of the material to dissipate energy. The property increases with the increase of the frequency of the applied load. These observations are also proving the better performance recorded at impact.
- The glass transition temperature of the reinforced polyurea composites, as shown by the trend of the loss modulus, does not change from that of pure polyurea. This means that the fillers – in our case - seem to not disrupt the polymer soft and hard domain composition as noticed in previous works present in the literature.
- The morphology of the polyurea composites, as from the scanning electron microscopy analysis (SEM), shows that milled glass fibers-polyurea composite are characterized by a presence of distributed micro-porosity due to a poor bonding between the fiber and the matrix while alumina-composites are dense and the particles are fully embedded into the matrix. These two different morphologies are both helpful to explain the improved - but different - behavior of these materials at impact. The presence of a poor bonding between the fibers and the polymer in the former case, favors the higher energy dissipation at impact by triggering additional friction phenomena. The latter case instead, the presence of a well bonded ceramic filler hardens the matrix and allows the polymer to sustain much higher impact force, as verified by conducting the experiments.

To conclude, it is possible to increase substantially the impact energy mitigation ability of the polyurea coatings by addition of fillers. Fillers of different type imply different micro-mechanical and dynamic behavior at impact. Inclusions larger than a nanometer size seem to not disrupt the segmental dynamics of the polymer and, instead, add extra internal dissipation phenomena or hardening at the benefit of the increased survivability of the system. In order to optimize the behavior of these materials, further studies and experiments are needed for the full understanding of the phenomena involved. We also think that an optimal response can be achieved by the material if the range of frequency of the impact event is known (or can be predicted). In such a way the material's damping properties can be specifically designed for having a maximum at such a frequency or in a range of frequencies close to that of an event concerned.

ACKNOWLEDGMENT

This work was partially supported by the Shenzhen Innovative R&D Team Program (Peacock plan), No. KQE201106020031A.

REFERENCES

- [1] R. Hill, and E.E. Walker, "Polymer Constitution and Fiber properties," *J. Polym. Sci.*, vol. 3, no. 5, pp. 609-630, 1948.
- [2] R.A. Grigsby Jr., and D.M. Rice, "Some recent advances in Polyurea RIM," *J. Cell. Plast.*, vol. 22, pp. 484-495, 1986.
- [3] F. Sann Jr., "Improved RIM polyurea body panels," *J. Cell. Plast.*, vol. 28, pp. 14-23, 1992.
- [4] J. Primeaux Dudley, "Spray polyurea elastomer using chopped glass roving," U.S. Patent 5118728, Jun 2, 1992.
- [5] K.J. Knox, M.I. Hammons, T.T. Lewis, and J.R. Porter, "Polymer Materials for Structural Retrofit," Force protection branch, Air Expeditionary Forces Technologies Division, Air Force Research Laboratory, technical report, Tyndall AFB, Florida, 2000.
- [6] J.E. Crawford, "Modeling blast-resistant protection systems composed of polymers and fabric," Karagozian & Case, technical report.
- [7] J.E. Crawford, and L. Shengrui, "Design and implementation of protective technologies for improving blast resistance of buildings," Enhancing Building Security Seminar, Singapore, 2005.
- [8] G.N. Nurick, and J.B. Martin, "Deformation of thin plates subjected to impulsive loading-A review, Part I: theoretical considerations," *Int. J. Impact Eng.*, vol. 8, no. 2, pp. 159-170, 1989.
- [9] G.N. Nurick, and J.B. Martin, "Deformation of thin plates subjected to impulsive loading-A review, Part II: Experimental Studies," *Int. J. Impact Eng.*, vol. 8, no. 2, pp. 171-186, 1989.
- [10] W. Mock, and E. Balizer, paper presented at Polyurea Properties and Enhancement of Structures under Dynamics loads Airlie, VA, 2005.
- [11] M.R. Amini, "Effect of Polyurea on the dynamic response and fracture resistance of steel plates under impulsive loads," PhD Dissertation, Dept. Mech. Aero. Eng., Uni. California San Diego, 2007.
- [12] Z. Xue, and J.W. Hutchinson, "Neck retardation and enhanced energy absorption in metal-elastomer bilayers," *Mech. Mater.*, vol. 39, pp. 473-487, 2007.
- [13] J. Yi, M.C. Boyce, G.F. Lee, and E. Balizer, "Large deformation rate-dependent stress-strain behavior of polyurea and polyurethanes," *Polymer*, vol. 47, pp. 319-329, 2006.
- [14] R.B. Bogoslovov, C.M. Roland, and R.M. Gamache, "Impact-induced glass transition in elastomeric coatings," *Appl. Phys. Lett.*, vol. 90, 221910-3, 2007.
- [15] E. Balizer, J. Fedderly, Gilber Lee, S. Bartyczak, and W. Mock Jr., "Investigation of microstructural changes in impacted polyurea coatings using small angle X-ray scattering (SAXS)," *Powder Diffraction*, vol. 26, no. 2, pp. 149-154, 2010.
- [16] W. R. Willkomm, Z.S. Chen, C. W. Macosko, D.A. Gobran, and E.L. Thomas, "Properties and phase separation of reaction injection molded and solution polymerized polyureas as a function of hard block content," *Polym. Eng. Sci.*, vol. 28, no. 14, pp. 888-900, 1988.
- [17] A. J. Ryan, J.L. Stanford, and A.N. Wilkinson, "Structure properties relations in non-linear segmented copolyureas formed by reaction injection moulding, RIM," *Polym. Bull.*, vol. 18, pp. 517-523, 1987.
- [18] D. Fragiadakis, R. Gamache, R.B. Bogoslovov, and C.M. Roland, "Segmental dynamics of polyurea, effect of stoichiometry," *Polymer*, vol. 51, pp. 178-184, 2010.
- [19] C.M. Roland, J.N. Twigg, Y. Vu, and P.H. Mott, "High strain rate mechanical behavior of polyurea," *Polymer*, vol. 48, pp. 574-578, 2007.
- [20] C.M. Roland, and R. Casalini, "Effect of hydrostatic pressure on the viscoelastic response of polyurea," *Polymer*, vol. 48, no. 18, pp. 5747-5752, 2007.
- [21] A.V. Amirkhizi, J. Isaacs, J. McGee, and S. Nemat-Nasser, "An experimentally-based viscoelastic constitutive model for polyurea, including pressure and temperature effects," *Philos. Magazine*, vol. 86, no. 36, pp. 5847-5866, 2006.
- [22] W. Awad, and C. Wilkie, "Investigation of the thermal degradation of polyurea: the effect of ammonium polyphosphate and expandable graphite," *Polymer*, vol. 51, no. 11, 2010.
- [23] X. Qian, B. Yu, C. Bao, L. Song, B. Wang, W. Xing, Y. Hu, and R.K.K. Yuen, "Silicon nanoparticles decorated graphene composites: preparation and their reinforcement on the fire safety and mechanical properties of polyurea," *J. Mater. Chem. A*, vol. 1, pp. 9827-9836, 2013.
- [24] R. Casalini, R. Bogoslovov, S.B. Qadri, and C.M. Roland, "Nanofiller reinforcement of elastomeric polyurea," *Polymer*, 53, pp. 1282-1287, 2012.
- [25] F. Ghezze, A. V. Amirkhizi, S. Nemat-Nasser, "Highly deformable polyurea composites," submitted for patent application in 2008, filed document UCSD Docket no SD2008-021; Remained unpublished.
- [26] F. Ghezze, "Materials with integrated distributed sensing," presented at the Cellular Concepts for the mitigation of localized high intensity dynamic loads Conference, University of California Santa Barbara, Mar. 26-28, 2008.
- [27] F. Ghezze, and X. Miao, "Composite coatings with high vibration damping properties," presented at the 11th International Conference on Vibration Problems, ICOVP, Lisbon, Portugal, 9-12 Sept., 2013.
- [28] Isonate® 143L, the Dow Chemical Company, Modified MDI, 2001, Midland.
- [29] Versalink P1000, Air Products and Chemicals, Inc., 2003, Allentown, PA.
- [30] S. Nemat-Nasser, J.B. Isaacs, and J.E. Starrett, "Hopkinson techniques for dynamic recovery experiments," *Proc. R. Soc. A*, vol. 435, pp. 371-391, 1991.
- [31] J.D. Ferry, *Viscoelastic properties of polymers*. 3rd Edition: Wiley, 1980.
- [32] M.S. Jhon, R.J. Metz, and K.F. Freed, "Effective medium theory for elastic matrix composites containing dispersed particulates," *J. Stat. Phys.*, vol. 52, no. 5/6, pp. 1325-1342, 1988.
- [33] L.E. Nelson, *Mechanical properties of Polymers and Composites*. New York: Marcel Dekker, 1974
- [34] C.G. Robertson, C.J. Lin, M. Rackaitis, and C.M. Roland, "Influence of particle size and polymer-filler coupling on viscoelastic glass transition of particle-reinforced polymers," *Macromolecules*, vol. 41, pp. 2727-2731, 2008.

Negative Stiffness Materials for Vibration Damping: a Material Realization of a Nonlinear Bistable Element

Jan Heczko¹, Zuzana Dimitrovová*², Hélder C. Rodrigues³

¹Department of Mechanics, Faculty of Applied Sciences, University of West Bohemia, Pilsen

²Departamento de Engenharia Civil, Faculdade de Ciências e Tecnologia, Universidade Nova de Lisboa and LAETA, IDMEC, Instituto Superior Técnico, Universidade de Lisboa, Lisboa, Portugal

³LAETA, IDMEC, Instituto Superior Técnico, Universidade de Lisboa, Lisboa, Portugal

* zdim@fct.unl.pt

Abstract— This paper addresses material and shape design of a prototype exhibiting a negative stiffness over a finite range of global strains. The objective is to define a design loop, where, starting from the actual material realization, a corresponding finite element model is developed and associated to a bistable discrete one-dimensional mechanical system composed of pre-compressed springs, a stabilizing spring and a damper. The discrete model can easily be analyzed and optimized for improved vibration damping properties. This will allow the determination of an alternative specification of a new optimized prototype. If confirmed by finite element analysis, then an improved prototype can be produced accordingly. This paper presents the first results: the material realization and the corresponding discrete model identification exploring also the finite element model. Optimization will be subject of further research. It is concluded that the specimen behaves according to the expectations, i.e. the negative stiffness region is well-formed and the discrete correspondence is easily obtainable. Such a structure can be used as a negative-stiffness element to achieve extreme mechanical properties of a composite or as a structure with improved damping properties.

Keywords—Experimental Testing, Finite Element Modelling, Negative Stiffness, Nonlinear Bistable Element, Vibration control.

I. INTRODUCTION

RECENT PROGRESS in material processing and manufacturing has stimulated strong scientific and industrial interest in material design optimization. Tailoring material properties to achieve the optimal response to a given solicitation provides an important input to the development of new materials. New horizons in novel materials can be opened if the concept of the structural negative stiffness is considered.

Materials with adequate mixtures of carefully selected phases, including also a negative stiffness phase, have been shown to possess the ability of reaching extreme properties, such as stiffness or vibration damping [1, 2]. Apart from many studies exploring theoretically advances achieved in materials incorporating negative stiffness constituents [3] there are also real world applications that had proven utility of this concept. Attempts to manufacture such materials were made using unstable structures [4, 5], which exhibit negative stiffness in the vicinity of the unstable equilibrium point. In this case one has to constrain the negative stiffness components in order to

ensure that the structure really operates smoothly along the negative branch of the force-displacement graph and does not jump into one of the stable states.

Negative stiffness dampers are already available on the global market. Starting from Platus' patent [6] and related article [7], Minus K Technology [8], founded in 1993 by Dr. Platus, is the leading industry manufacturing negative stiffness dampers. Nevertheless, advantages of such mechanisms were already documented in Russian monograph that was later on translated to English [9]. One of the most recent alternative realizations is given in [10]. In [10] pre-compressed beams represent the negative stiffness component that is stabilized by another spring. The specimen was produced by 3D systems Sinter station Hi QTM selective laser sintering machine. It was proven that with the increasing pre-compression, implying decrease in fundamental frequency, also the decrease in resonance peak in displacement transmissibility is verified. Nevertheless, it is still a challenging task to design a continuous isotropic three-dimensional material, easy to manufacture, that would globally act in the same way as a discrete mechanism.

In this paper a material produced from polyethylene foam sheets is examined. Such a material is often used for packing protection and it is known for its several other useful properties like easy forming and possibility of heat-welding. In order to integrate an inherent bistable element in such sheets, additional semi-circumferential cuts were introduced. The advantage of this realization is that the material, apart from additional cuts, does not need any special manufacturing technique as the one described in [10]. The base material is easily accessible and cheap. The work presented here is an extension of the preliminary results published in [11], which was developed in continuation with [12].

The new contribution of this paper consists in the innovative realization of a material exhibiting negative stiffness over a range of finite strains and in the development of a method that links this material with a discrete mechanism exploiting also the finite element model. Future work will address its performance optimization.

The paper is organized in the following way. In Section II the polyethylene foam material is described and results of experimental tests are given. In Section III finite element model is developed and numerical results are presented and compared with the experimental testing. A procedure of

linking the continuous model to a discrete mechanism is described in Section IV. New achievements and further challenges are summarized in Section V.

II. POLYETHYLENE FOAM

The polyethylene foam is a cellular material that can be used for packing protection. In the application described in this paper it is utilized as a base material of a periodic arrangement that can exhibit negative stiffness over a certain range of global finite strains. The sheets formed by two light polyethylene foam plates of density $20 \text{ kg} \cdot \text{m}^{-3}$ glued together were provided by 100metros company [13]. The original sheet size was approximately $260 \times 260 \times 20\text{-}23 \text{ mm}$. No information about mechanical properties was supplied by 100metros company. Literature and internet searches on polyethylene foam properties provided large range of material data, but not the mechanical ones. Therefore it was decided to accomplish own tests to estimate the mechanical properties.

Two kinds of specimens were prepared: homogeneous ones for the analysis of the base material properties and specimens with semi-circumferential cuts as a representation of the material with the inherent bistable element (Fig. 1), i.e. of the material exhibiting the negative stiffness. The bistable elements (basic cells) were repeated in one direction to form a periodic material. A simple electric saw was used for straight cuts. Semi-circumferential cuts of 50 mm diameter were added with the help of a heated blade. By simply observing it, it was concluded that the elliptical shape of the bubbles predetermined two directions of orthotropy. The axis of symmetry of the bistable basic cell was aligned with the stiffer direction, that is, the direction of the rising of the foamed cells. Unfortunately, the two plates were not always glued together in the same manner, because such a requirement is not necessary for common applications, and therefore the material testing results showed significant discrepancy.

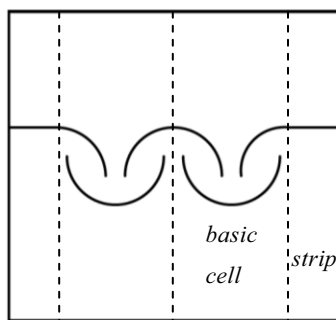


Fig.1. Schematics of the specimen: semi-circular cuts forming the bistable element – two basic cells of the periodic structure with lateral strips

Specimens for uniaxial tension, compression and cyclic loading were prepared at DEC/FCT/UNL (Department of Civil Engineering, Faculdade de Ciências e Tecnologia, Universidade Nova de Lisboa) and tested at the same place and at DEM/IST/UL (Department of Mechanical Engineering, Instituto Superior Técnico, University of Lisbon). Only the most significant results will be shown. Dimensions of the

specimens, results of which are presented, are summarized in Table I.

	Width [mm]	Thickness [mm]	Length [mm]	Uniaxial Test
T01L	37.45	22.78	125	Tension (9mm/min)
T02T	39.92	22.38		
C01L	21.9	38.26	24.46	Compression (3mm/min)
C02T	21.93	38.63	24.45	
C03T	22.1	38.69	24.89	
C04L	25.14	39.1	24.97	
TS01	174	21.39	154	Tension (4mm/min)
TS02	174	21.39	154	Tension (9mm/min)

Table I. Summary of the characteristics of the specimens used in the experimental testing

The notation of the samples is related to the test performed, to the specimen type and to the specimen number. In this sense, first “T” means traction and “C” denotes compression. “01” and similar is the sample number. Homogeneous specimens have additional designation: “L” means that the stiffer direction was the longitudinal one, i.e. in the direction of the applied force, and “T” that it was the transversal one, i.e. in the direction perpendicular to the applied force. “S” is used for the specimen with the circumferential cuts.

The specimens were tested on a universal testing machine (model 5566, Instron Corporation Canton, USA) with a load cell of 10 kN. The cross-head velocity was in the range of 3 to $9 \text{ mm} \cdot \text{min}^{-1}$. The base material is viscoelastic and thus strain rate dependent, hence decrease in stiffness was recorded in higher load rates. Nevertheless, only the tests where the loading was induced in a quasi-static manner, not activating either the viscous behaviour or the inertial properties, are presented here. Results of the tension test on specimens T01L and T02T are shown in Fig.2.

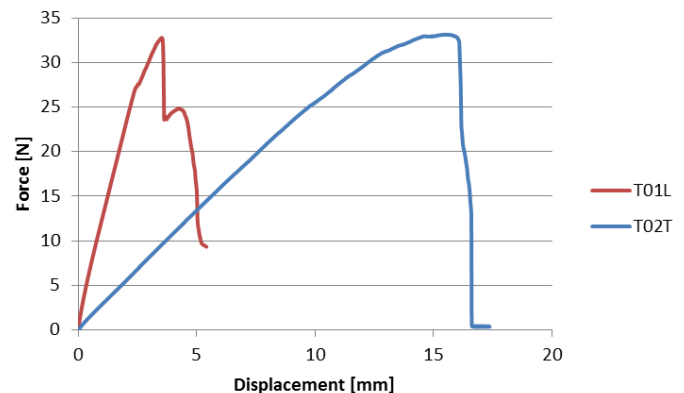


Fig.2. Uniaxial tension of homogeneous specimens

It is necessary to point out that these tests cover very large range of strains and therefore the non-linear behaviour is not clearly visualized in Fig. 2, but there is an initial Young's modulus that is significantly higher than the one fitting the

most of the force-displacement curve. In Fig. 3 secant modulus is plotted in each force increment and overlaid by a trend line obtained by a moving averaging method of rank 4.

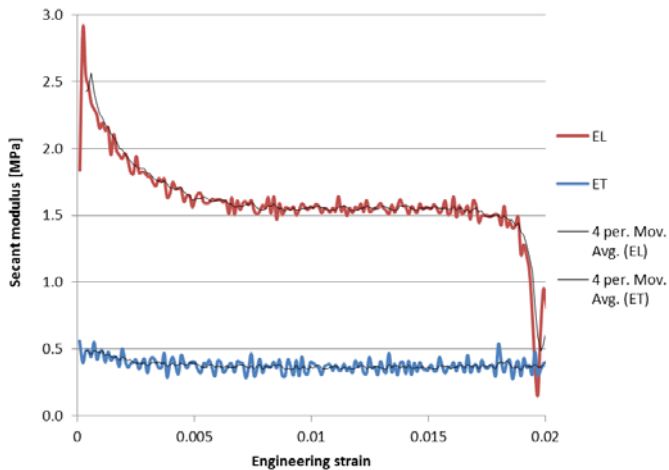


Fig.3. Secant modulus and trend lines obtained by a moving average method related to the initial part of the force-displacement curve from Fig. 2

Regarding the stiffer direction, the elastic modulus decreases exponentially from the initial value of 3 MPa to 1.6 MPa at approximately 0.008 engineering strain and then it drops to 1 MPa at 0.02 engineering strain. Regarding the softer direction, the modulus starts at 0.5 MPa, slowly decreases to 0.4 MPa and the specimen is able to bear very large engineering strains, reaching 0.1, when the modulus starts to decrease again. As expected, the behaviour in compression is quite different and the elastic moduli are significantly lower. Experimental curves are shown in Fig. 4.

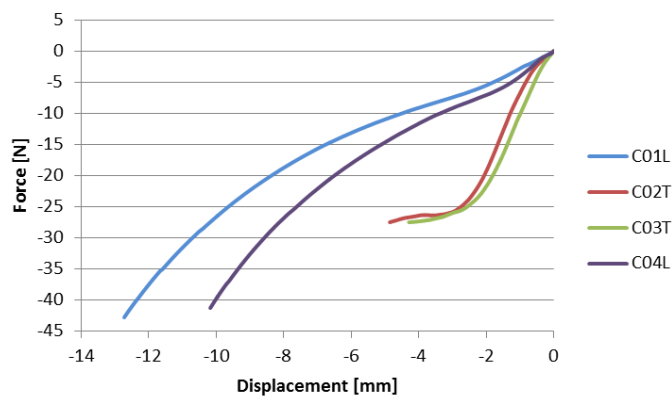


Fig.4. Uniaxial compression of homogeneous specimens

It is seen that for the longitudinal direction the strength is higher in compression than in tension, but the stiffness is significantly lower. There is also a significant difference in longitudinal and transversal directions. Roughly speaking, the stiffness ratio between the stiffer and the softer direction around 4. Moduli in transversal direction do not show significant difference when related to tension and compression, but in longitudinal direction the ratio of tension and compression modulus is around 20.

Furthermore, the bistable structure was tested. As expected, one basic cell of the bistable material was not sufficient to provide the required behaviour, because there was insufficient lateral constraint, and therefore the specimen was unable to show the negative branch in the global stiffness. These results will not be shown here. Specimens with two basic cells and lateral strips (Fig.1.) were tested instead. The lateral strip provided necessary constraint and facilitated a smooth snap through the unstable equilibrium. Two displacement rates were implemented as $4 \text{ mm} \cdot \text{min}^{-1}$ and $9 \text{ mm} \cdot \text{min}^{-1}$, but no significant differences were found between the results. Different phases of the loading are shown in Fig. 5, the negative branch is verified between stages (b) and (c).

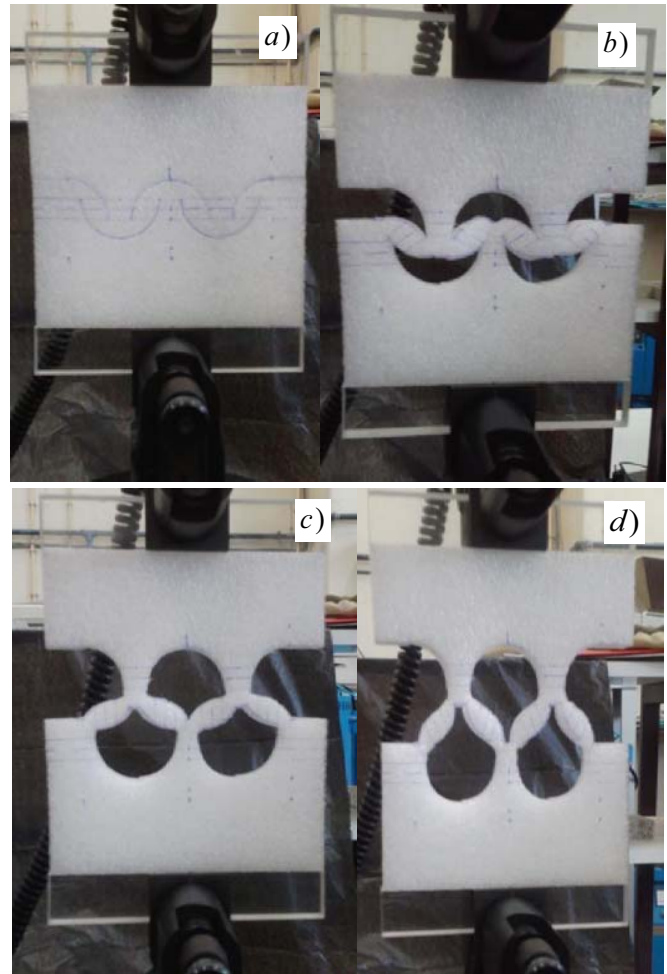


Fig. 5. Tension test on the bistable material: (a) initial position, (b) beginning of the negative stiffness, (c) new beginning of the positive stiffness, (d) initiation of failure

Monotonic displacement-control tests revealed that the negative stiffness region in force-displacement curve is well-formed. However, a visible out-of-plane deformation helped to reach the next stable equilibrium at lower global force, than it would be required by a perfectly plane specimen. Fortunately this fact did not affect the global performance, but in future works some preventive measures have to be taken, like for instance reinforce the specimen by a stiffer thin plate that would prevent out-of plane deformations. The force-

displacement curves related to the experiment described above are shown in Fig. 6.

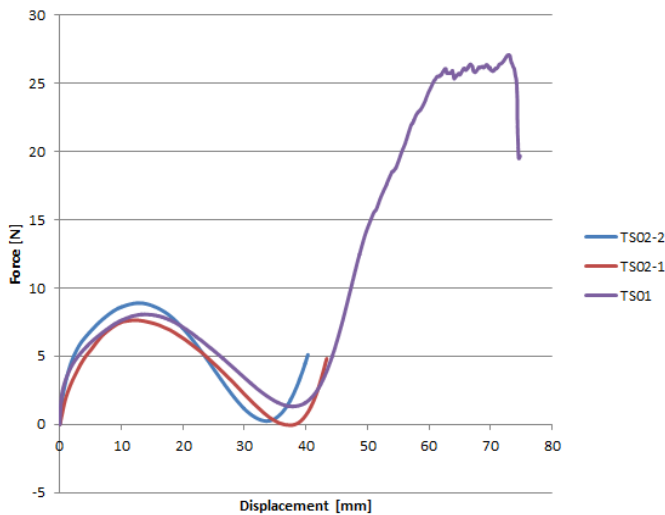


Fig.6. Tension tests on the bistable material

In Fig.6 caption “-1” and “-2” stand for the number of the test performed on the same specimen TS02. Specimen TS01 was left until the failure.

In addition, cyclic tests were performed on the specimen TS02. The objective of the cyclic tests was to show that in displacement control regime the specimen can operate solely over the negative stiffness region. Results are shown in Fig.7.

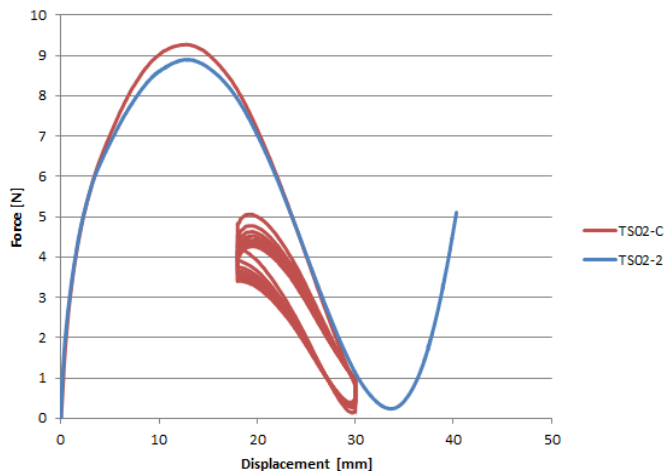


Fig.7. Cyclic test on the bistable material (comparison with the tension test)

Induced displacements in cyclic tests varied between 18 and 30 mm with a short time delay at each extreme position. The gradual displacement increase and decrease had the same duration of 15 s, which was also the time delay at extreme positions. Sharp corners of loading and unloading paths show that during the pause the specimen entered in relaxation, i.e. there is a noticeable decrease in load on the same displacement level in time. Without pausing in the experimental test, the unloading curve would basically follow the same path in each branch because the hysteresis loop is

quite narrow. In the legend of Fig.7 “-C” stands for the cyclic test. In Fig. 7 it is also seen that the strain energy is not fully recovered, the main difference being in the first unloading path.

III. FINITE ELEMENT MODEL

The finite element model was created in ANSYS [14] assuming plane stress. Only half of the tested structure was modelled due to the symmetry. The finite element mesh was tested on sensitivity, but relatively fine mesh as shown in Fig. 8 was used, because the calculations were quite fast. A small gap of 0.5 mm was introduced in the cut region to avoid unsuitable element shapes in sharp corners. Regarding the boundary conditions, symmetry condition is used on the left border, the bottom border is fixed in vertical direction and a vertical displacement is imposed on the top. The right border is left free.

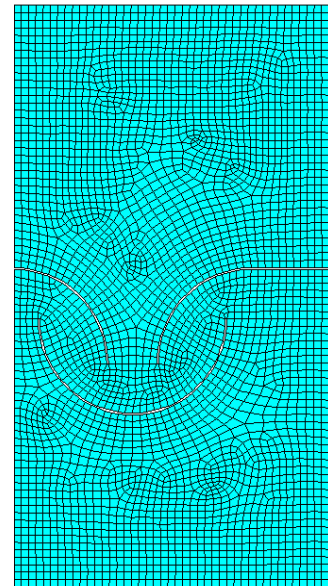


Fig. 8. Finite element mesh in undeformed position

Several material models were tested, starting from the simplest one, the linear elastic material. After several attempts it was concluded that none of the features detected experimentally on homogeneous specimens should be omitted. Thus, the material model must account for orthotropy as well as for elastic non-linearity with different secant moduli in tension and in compression. It was impossible to introduce all these features, because material models available in commercial software like ANSYS and ABAQUS have some limitations.

Hyperelastic models did not perform well, because they usually assume higher stiffness in compression than in tension, but the experimental results obtained here showed the opposite tendency. Main advantage of hyperelastic models was that they did not reveal significant convergence difficulties along the loading path. The disadvantage was that there was no possibility to induce the strong initial non-linearity showed by experimental testing. Hence, the global initial stiffness that

yielded approximately the same maximum force at the onset of the negative branch was significantly lower. The deformation proceeded smoothly without a possibility to create a noticeable “snap-through” effect. The smooth passage over the unstable equilibrium prevented to achieve the zero force level again.

The results presented here were obtained in ANSYS, because in ANSYS it was possible to combine elastic non-linearity (material model MELAS) with orthotropic engineering constants. Unfortunately, this non-linearity is based on von Mises stress-(von Mises total) strain curve and therefore there was no possibility to introduce different tension and compression behaviours. This was the reason, why it was decided to fit the material model to the experimental tests, exploiting some general features obtained experimentally on homogeneous specimens. Regarding the orthotropy, ratio of elastic moduli between the soft and stiff direction was estimated as 4, according to the experimental tests. Since no experiments were performed to estimate other properties, shear modulus was set equal to the soft Young’s modulus and Poisson’s ratio was estimated. Using APDL (ANSYS Parametric Design Language) an identification optimization module was developed to fit the material data describing the non-linearity to the experimental results.

Non-linear curve was established by a step-by-step procedure, where the slope of the stress-strain curve was tuned to achieve the expected global force, in accordance with the test TS02-2. In this ANSYS material model, none of the posterior slopes can be higher than the initial; also none of them can be negative. The fitting procedure provided sufficient results, but, as expected, sometimes the slope value was not possible to tune, because it affected only a limited region of the finite element model, and therefore it was not sufficient to induce the required changes in the global force.

E_L [MPa]	E_T [MPa]	G_{LT} [MPa]	ν_{LT}
2.25	0.55	0.55	0.3

Table II Engineering constants defining the orthotropy

$\epsilon_{T,vM}$	σ_{vM} [Pa]	E [MPa]
0	0	2.2
$3.2 \cdot 10^{-04}$	700	0.93
$7.5 \cdot 10^{-04}$	1100	0.39
$1.6 \cdot 10^{-02}$	7000	0.063
0.35	28000	0.034
5.35	200000	0

Table III Values defining the elastic non-linearity

It was concluded that sufficient coincidence with experimental results can be achieved by a material model with orthotropic properties given in Table II and stress-strain curve given in Table III. When confronted with the measured data, it is observed that the initial moduli in Table II are approximately verified by the tension tests on homogeneous

specimens. The moduli from Table II decrease proportionally according to Table III (in Table III the values related to the stiffer direction are given) and this decrease is justified by highly compressed localized regions of the model, where compression moduli, i.e. moduli that are much lower, should be used. Thus the corresponding strain where an onset of another slope is specified is lower than the one in Fig. 3. Further decrease in high strains is justified by the non-linearity of the tension as well as compression moduli.

In this way it is possible to fit the material model in a way that main part of the experimental force-displacement curve is the same, the force at the onset of the negative branch achieved experimentally is 8.9 N at 12.6 mm and numerically 8.9 N at 12.5 mm, Fig. 9.

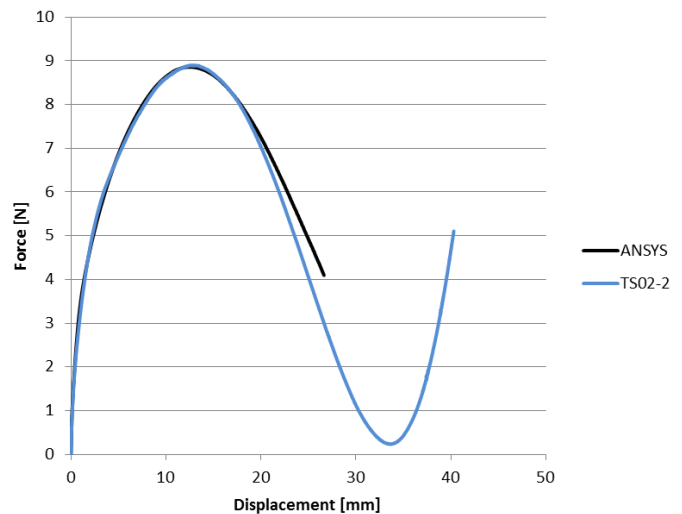


Fig.9. Force-displacement curve: the experimental, ANSYS non-linear elastic material with orthotropic base

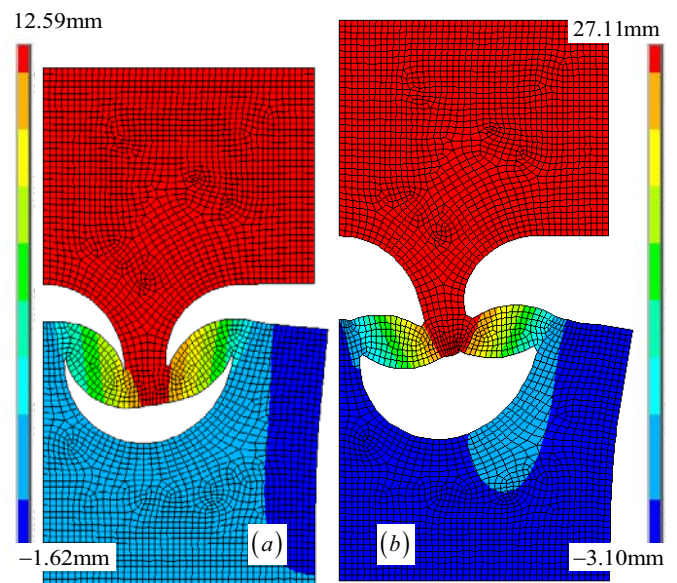


Fig.10. Onset of the negative stiffness (a) and last position (b) determined in ANSYS

In Fig. 10 the distribution of the vertical displacement at the onset of the negative branch and at the final position where

convergence was lost, are shown. Unfortunately, full negative branch was not possible to follow numerically due to convergence difficulties.

This can be explained by the fact that at these stages highly compressed localized regions are present. As the initial part was adjusted to significant tension, it cannot work perfectly well in significant compression, where the material performance should be in general softer. If this additional feature would be possible to introduce, the loading path would have been completed. Also, as written above, during the experimental tests visible out-of-plane deformation occurred and this fact was not modelled numerically. These facts are not related to the finite element mesh. Indeed these limitations come from the material model, and not from the necessity of remeshing as can be seen in Fig. 11 where deformed shapes are obtained for hyperelastic behaviour.



Fig.11. Confirmation of the mesh suitability, hyperelastic (neo-Hookean) behaviour in ANSYS

In summary, it can be concluded that the material identified by the fitting procedure verifies reasonably the data obtained experimentally. It does not work over the full loading path due to software limitations. It would be necessary to introduce a user defined behaviour, which will be accomplished in future work. Hence, the finite element model is ready for shape optimization, because the match with the experimental data is reasonable and very good regarding the initial global stiffness and the maximum force achieved. Future works in this part will avoid three dimensional modelling, because it is preferable to adapt the specimen as already explained.

IV. DISCRETE MECHANISM

The main purpose of this identification is to obtain a model with low computational cost, which can be easily analysed, optimized for dynamic behaviour and provide better insight into physical phenomena involved. The discrete system that is investigated is schematically depicted in Fig. 12. It consists of two pre-compressed spring elements, k_H , a stabilizing spring element, k_V , a viscous damping element, c , and a mass, m . The original length of the horizontal springs is L and the

amount of pre-compression is denoted by d . The mechanism is symmetric around the vertical axis. Regarding the dynamic performance two variants of excitation can be considered: (i) kinematic loading, prescribed as time-dependent base excitation, $x_0(t)$, and (ii) force, $F(t)$.

The equation of motion of the one-dimensional system described above reads as:

$$m\ddot{x} + c(\dot{x} - \dot{x}_0) + F_V = F(t) \tag{1}$$

where the elastic vertical non-linear force F_V is given by

$$F_V = \left(k_V + 2k_H \left(1 - \frac{L}{\sqrt{(x-x_0)^2 + (L-d)^2}} \right) \right) (x-x_0) \tag{2}$$

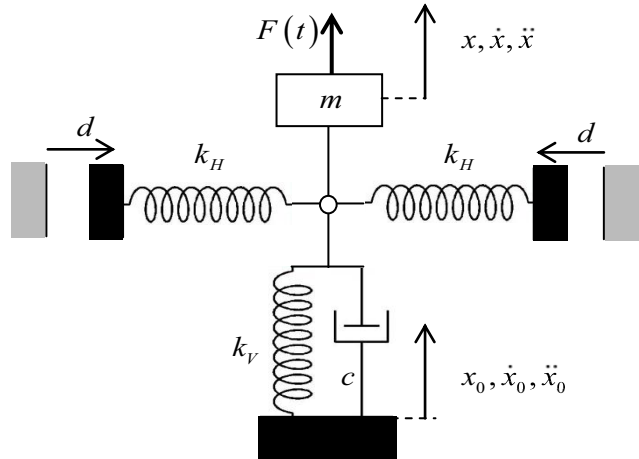


Fig.12. Complete discrete model

Considering only static behaviour and the specimen described and tested in previous sections, then the model can be represented as shown in Fig.13.

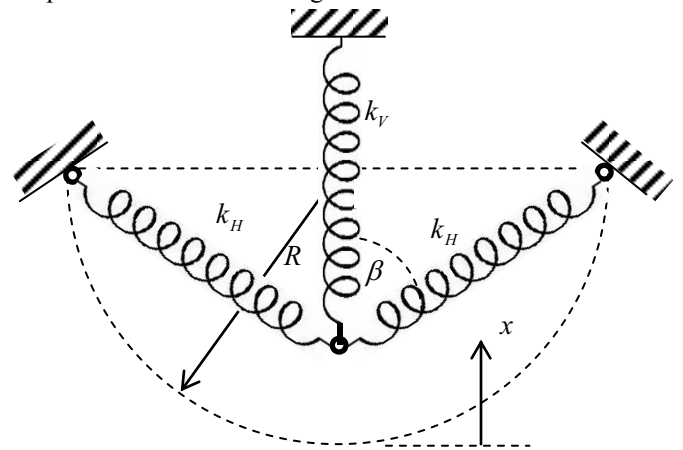


Fig. 13. Spring representation of the tested specimen

In accordance with the experimental tests, it is assumed that the undeformed springs have their free extremities at the position $x = 0$. Other geometrical details are related to the semi-circumferential cuts in the structure. The non-linear force representing the system above can be written as:

$$F_V = k_V x - 2 \cos \beta N = k_V x - 2 \frac{R-x}{\sqrt{R^2 + (R-x)^2}} k_H \left(\sqrt{R^2 + (R-x)^2} - R\sqrt{2} \right) = k_V R + k_V R \xi - 2 \xi k_H R \left(1 - \sqrt{\frac{2}{1+\xi^2}} \right) \quad (6)$$

$$k_V R \xi - 2(1-\xi) k_H R \left(1 - \frac{1}{\sqrt{1-\xi+\xi^2/2}} \right) \quad (3)$$

where $\xi = x/R$ and N stands for the elastic force developed in the inclined springs. The objective is to tailor force-displacement curve of this model to be reasonably proximate to the behaviour of the physical model. The parameter connected to the specimen geometry, R , is equal to 25 mm. Consequently, there are only two variables k_V and k_H and 4 essential conditions to fulfil. The essential conditions require placing positions of zero stiffness in terms of the elastic force as well as displacement. The sum of absolute value of these four differences can be taken as the objective function. Optimal parameters, $k_V = 0.18\text{N/mm}$ and $k_H = 1\text{N/mm}$ are obtained by parametric optimization, global performance comparison is shown in Fig. 14.

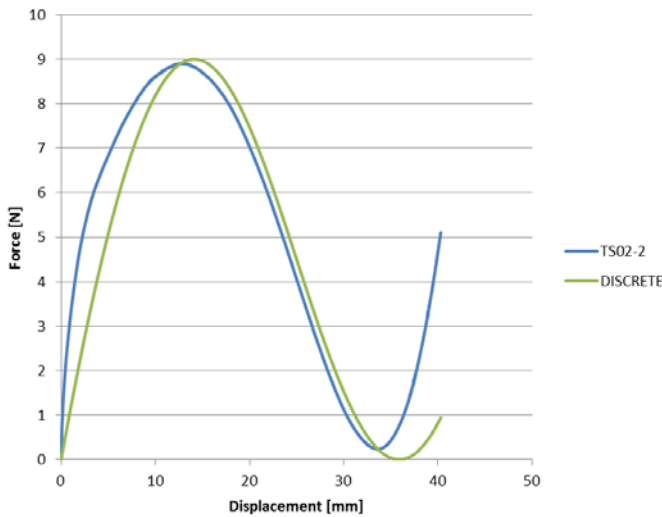


Fig.14. Force-displacement curve: the experimental and the discrete model

As already stated, the discrete model can be easily analysed. Stationary points are determined by:

$$\xi_1 = 1 - \frac{1}{k_V + 2k_H} \sqrt{-(k_V + 2k_H)^2 + 2\sqrt{3}k_H^2(k_V + 2k_H)^4}$$

$$\xi_2 = 1 + \frac{1}{k_V + 2k_H} \sqrt{-(k_V + 2k_H)^2 + 2\sqrt{3}k_H^2(k_V + 2k_H)^4} \quad (4)$$

Under the assumption that

$$8k_H(k_V + 2k_H)^2 \geq (k_V + 2k_H)^3 \quad (5)$$

Numerical values for optimal parameters are $\xi_1 = 0.573$ and $\xi_2 = 1.427$, that are, as expected, symmetrically placed around value 1. A shift can be introduced as $\hat{\xi} = \xi - 1$, yielding

where the first term expresses the pre-compression of the vertical spring. Then the model is equal to the one in Eqs. (1-2). Detailed analysis of this model is presented in [10].

V. CONCLUSIONS

A bistable nonlinear material that exhibits negative stiffness over a finite range of global strain was analysed experimentally and numerically. Correspondence with a finite element model and a discrete model was established. For the discrete model standard methods of analysis can be utilized. In future works the discrete model will be optimized for vibration damping. Shape optimization of semi-circumferential cuts will be performed on the finite element model and conclusions will be tested experimentally.

ACKNOWLEDGMENT

The authors would like to express their gratitude to 100metros company for providing the polyethylene sheets. They also greatly appreciate the help of Ph.D. students at FCT/UNL, especially of MSc. Hugo Fernandes and support to experimental testing given by Ph.D. student at IST/UL MSc. Ana Catarina Vale under supervision of Prof.^a Fátima Vaz (IST/UL).

REFERENCES

- [1] T. Jaglinski, D. Kochmann, D. Stone, and R.S. Lakes, "Materials with Viscoelastic Stiffness Greater than Diamond," *Science*, vol. 315, pp. 620-622, Feb. 2007.
- [2] R.S. Lakes, "Extreme Damping in Composite Materials with a Negative Stiffness Phase," *Phys. Rev. Lett.*, vol. 86(13), pp. 2897-2900, 2001.
- [3] J. Prasad, and A.R. Diaz, "Viscoelastic Material Design with Negative Stiffness Components using Topology Optimization," *Struct. Multidisciplinary Optimizat.*, vol. 38, pp. 583-597, 2009
- [4] R.S. Lakes, "Extreme Damping in Compliant Composites with a Negative-Stiffness Phase," *Phil. Mag. Lett.*, vol. 81(2), pp. 95-100, 2001.
- [5] H. Kalathur, and R.S. Lakes, "Column Dampers with Negative Stiffness: High Damping at Small Amplitude," *Smart Mater. Struct.*, vol. 22(8), 084013-21, 2013.
- [6] D.L. Platus, "Vibration Isolation System," WIPO Patent Application WO/1991/002921, 1991.
- [7] D.L. Platus, "Smoothing out Bad Vibes," *Mach. Des.*, vol. 26, pp. 123-130, 1993.
- [8] <http://www.minusk.com/index.html>
- [9] P. Alabuzhev, A. Gritchin, L. Kim, G. Migirenko, V. Chon, and P. Stepanov, *Vibration Protecting and Measuring Systems with Quasi-Zero Stiffness*. Hemisphere Publishing Corporation, 1989 (published in Russian in 1986).
- [10] L. Kashdan, C.C. Seepersad, M. Haberman, and P.S. Wilson, "Design, fabrication, and evaluation of negative stiffness elements using SLS," *Rapid Prototyping J.*, vol. 18(3), pp. 194-200, 2012.
- [11] J. Heczko, Z. Dimitrovová, and H.C. Rodrigues, "Composite material with negative stiffness inclusion for vibration damping: The effect of a nonlinear bistable element," in *Proc. 11th Int. Conf. on Vibration Problems (ICOVP-2013)*, Lisbon, Portugal, 9-12 September 2013.
- [12] J. Heczko, Z. Dimitrovová, and H.C. Rodrigues, "Optimization of linear and non-linear one-dimensional visco-elastic isolators for passive vibration control," in *Proc. 2nd Int. Conf. on Eng. Optimizat. (EngOpt2010)*, Lisbon, Portugal, 6-9 September 2010.
- [13] www.100metros.pt/
- [14] Release 12.1 Documentation for ANSYS, Swanson Analysis Systems IP, Inc., 2009.

Design Criteria for a Pendulum Absorber to Control High Building Vibrations

F. S. Oliveira¹, A. L. Z. Gomez¹, S. M. Avila ^{*2}, and J. L. V. Brito¹

¹Civil and Environmental Engineering Department, University of Brasilia, Brazil

²Gama Engineering College, University of Brasilia, Brazil

*avilas@unb.br

Abstract—The increasing development of structural analysis techniques, the appearance of more resistant materials, and the high cost of construction in big metropolis, caused an elevation on the height of buildings, making these structures considerably more vulnerable to actions of dynamic loads such as wind and earthquakes. Due to the problems caused by the action of these dynamic loads, vibration control has become a relevant issue in Civil Engineering. One of the most used vibration control systems is the Tuned Mass Damper (TMD). It basically consist of a mass-spring-damper system attached to the main structure, the frequency of the damper is tuned to a particular frequency, with the goal of making the TMD vibrate out of phase with the main system, thus transferring the energy system to the damper. The present study purpose is to evaluate the efficiency of a pendulum TMD when the structure is subjected to dynamic loads such as random excitation, given by power spectral density functions, and harmonic loads. Analytical expressions are derived, minimizing the mean square value of the power spectral density. Also parametric studies are performed to define design criteria, performing frequency response function minimization, searching its minimum maximum amplitudes iteratively. The behavior of a ten storey shear building is analyzed, reducing it to one degree of freedom through modal analysis. A pendulum TMD is attached to it, considering the optimal parameters obtained in this work. A set of general dimensionless optimal parameters for a pendulum TMD are presented in this study, they can be employed to the design of a pendulum to control any tall building, subjected to random dynamic loads, with different mass and damping ratios.

Keywords—Passive Control, Structural Control, Structural Dynamics, Tuned Mass Damper

I. INTRODUCTION

The increasing development of structural analysis techniques, the appearance of more resistant materials, and the high cost of construction in big metropolis, caused an elevation on the height of buildings, making these structures considerably more vulnerable to actions of dynamic loads such as wind and earthquakes. This kind of vibrations is undesirable, not only because of structural safety but also human comfort [1].

Thus concern about civil structures protection including its contents and occupants is a global reality. An alternative, widely studied in the last years, is the structural control. Originally developed in aerospace engineering, this technology was extended for civil engineering problems to protect bridges and high buildings from excessive dynamic loads. Structural control fundamentally changes structure stiffness and damping properties, adding external device or applying external forces. It is classified on passive, active, hybrid or semi-active control [1-2].

Widely studied in the last years, passive control consists in adding one or more devices to the structure to absorb or transfer part of the energy from to the main structure. Passive control typical mechanisms are: mass dampers that control structural response by transferring the energy between the main structure and an auxiliary mass; structural dampers that dissipate energy while deforming themselves and base isolation systems that uncouple structure moving from seismic soil vibrations.

A tuned mass damper (TMD) is a device composed by a mass-spring-dashpot attached to the structure aiming to reduce structural vibration response [2]. The beginning of TMD appliance to civil structures was at the sixties on high buildings, bridges, towers and industrial chimneys to control vibrations caused by wind forces. A TMD tuned to the first structure natural frequency reduces substantially the response associated to the first mode vibration while little reducing or even increasing the response associated to higher modes. Moreover, a single TMD is more sensitive to discrepancies on the first natural frequency and/or damping ratio considered on the design. These limitations can be overcome by adding more than one damper, each one of them tuned to a different vibration natural frequency [3].

One of the alternative geometries of the TMD is the pendulum shape [4]. The pendulum is attached to the structure and its movement excites the device transferring portion of the energy from one system to another, reducing this way structural member request of energy dissipation. This type of damper has its vibration period depending on the length of the cable, and can only be considered a linear device when the vibration amplitudes are small.

Lourenço [5] described the design, construction, implementation and performance of a prototype adaptative pendulum tuned mass damper (APTMD), demonstrating the performance improvements obtained when the tuned mass damper (TMD) parameters are optimized. In his study was considered the effect of adjusting the APTMD tuned frequency and damping ratio on a two storey test structure subjected to broadband and narrowband excitation.

Orlando and Goncalves [6] evaluated a pendulum TMD to control excessive vibrations in slender towers, it is presented a parametric analysis of non-linear oscillations of a tower-damper system searching the best configurations to reduce vibrations and tower construction.

Gerges and Vickery [7] studied the behavior of a pendulum TMD to reduce the structure rms displacement subjected to force and accelerations simulating random excitations such as white noise. A numerical studied was performed to obtain

optimal parameters to a damped main system subjected to seismic and wind loads.

Morga and Marano [8] investigate two different optimization criteria of TMDs applied to a slender structure excited by wind load: the reduction of the maximum displacement at the top of the structure; the reduction of the maximum inertial acceleration at the top of the structure. The wind load is defined by a superposition of the mean wind velocity and a filtered white noise.

The present study purpose is to evaluate the efficiency of a pendulum TMD when the structure is subjected to dynamic loads such as random excitation, given by power spectral density functions, and deterministic harmonic loads.

The behavior of a high building is analyzed, reducing it to one degree of freedom through modal analysis [2]. Two load cases are studied, the structure subject to a dynamic force and to a base acceleration. A pendulum TMD is attached to it in order to reduce excessive dynamic response.

Optimum parameters for the undamped case are obtained analytically minimizing the mean square value of the dimensionless displacement, considering an excitation of a white noise random force. Considering damping effects it is no longer possible to obtain an analytical solution, so in these cases parametric studies were performed. This numerical procedure is based on the MinMax method [9]. The design criteria are obtained through frequency response function minimization searching its minimum maximum amplitudes. This minimization is achieved by an optimization iterative process.

A set of general dimensionless optimal parameters for a pendulum TMD are presented in this research, they can be employed to the design of a pendulum to control any tall building, subjected to deterministic or random dynamic loads, with different mass and damping ratios.

II. MATHEMATICAL FORMULATION

1) Response frequency function to a system excited by harmonic force and base acceleration

Fig. 1 shows a schematic description of a pendulum TMD attached to a main system composing a two degree of freedom model DOF, the main system is reduced to a 1 DOF model corresponding to the mode to be controlled [2]. Fig. 1 presents the main system subjected to a force $F_s(t)$ and Fig.2 the system subjected to a base acceleration $\ddot{y}_0(t)$.

The equation of motion considering small displacement to Fig. 1 system are:

$$(M_s + M_p)\ddot{y} + M_p L \ddot{\theta} + C_s \dot{y} + K_s y = F_s(t) \quad (1)$$

$$M_p L \ddot{y} + M_p L^2 \ddot{\theta} + C_p \dot{\theta} + (K_p + M_p g L) \theta = 0 \quad (2)$$

and to Figure 2 system are:

$$(M_s + M_p)\ddot{y} + M_p L \ddot{\theta} + C_s \dot{y} + K_s y = -(M_s + M_p)\ddot{y}_0(t) \quad (3)$$

$$M_p L \ddot{y} + M_p L^2 \ddot{\theta} + C_p \dot{\theta} + (K_p + M_p g L) \theta = -M_p L \ddot{y}_0(t) \quad (4)$$

Where M_s : main system modal mass; C_s : main system modal damping; K_s : main system modal stiffness; M_p : pendulum mass; C_p : pendulum damping; K_p : pendulum stiffness; L : cable length; g : gravity acceleration; $F_s(t)$: excitation modal force; $y(t)$: main system displacement; $\theta(t)$: pendulum angular displacement; $y(t) = y_1(t) - y_0(t)$; $y_1(t)$: main system absolute displacement; $y_0(t)$: base displacement; $\ddot{y}_0(t)$: base acceleration. The pendulum natural frequency is $\omega_p = \sqrt{(K_p + M_p g L) / M_p L^2}$.

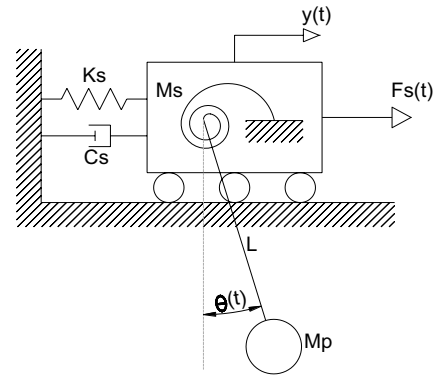


Fig. 1 Structure with a linear pendulum attached: excitation due to a force $F_s(t)$

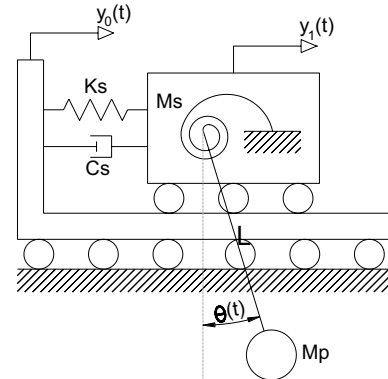


Fig. 2 Structure with a linear pendulum attached: excitation due to a base acceleration $\ddot{y}_0(t)$

These equations can be rewritten using the following dimensionless terms:

$$\alpha = \frac{\omega_p}{\omega_s}, \beta = \frac{\omega}{\omega_s}, \delta = L/H, \tau = \omega_s t \quad (5)$$

$$\mu = M_p / M_s, \eta = \frac{y}{H}, f_s(t) = F_s(t) / M_s \omega_s^2 H \quad (6)$$

$$\eta_0 = \frac{y_0}{H} \quad (7)$$

Substituting Eqs.(5-7) into Eqs. (1-4) the following equations are obtained:

$$(1 + \mu)\ddot{\eta} + \mu\delta\ddot{\theta} + 2\xi_s\dot{\eta} + \eta = f_s(t) \quad (8)$$

$$\ddot{\eta} + \delta\ddot{\theta} + 2\xi_p\alpha\delta\dot{\theta} + \alpha^2\delta\theta = 0 \quad (9)$$

to the system excited by an harmonic force and:

$$(1 + \mu)\ddot{\eta} + \mu\delta\ddot{\theta} + 2\xi_s\dot{\eta} + \eta = -(1 + \mu)\ddot{\eta}_0 \quad (10)$$

$$\ddot{\eta} + \delta\ddot{\theta} + 2\xi_p\alpha\delta\dot{\theta} + \alpha^2\delta\theta = -\ddot{\eta}_0 \quad (11)$$

to the system subjected to a base excitation.

Where η : dimensionless ratio between relative displacement and structure highness; α : frequency ratio; β : forced frequency ratio; μ : mass ratio; ξ_s : mains system damping ratio; ξ_p : pendulum damping ratio; δ : ratio between cable length and

structure highness $f_s(t)$: dimensionless excitation modal force; $\theta(t)$: pendulum angular displacement, and $\dot{\eta} = d\eta/d\tau$; $\dot{\theta} = d\theta/d\tau$; $\ddot{\eta} = d^2\eta/d\tau^2$; $\ddot{\theta} = d^2\theta/d\tau^2$. Considering $f_s = e^{i\omega t} = e^{i\beta\tau}$, $y_0(t) = \ddot{e}^{i\omega t} = e^{i\beta\tau}$ and, substituting this values into Eqs 8, 9, 10 and 11, and solving the linear equation system, it is obtained the dimensionless frequency response functions $H_\eta(\beta)$ e $H_\theta(\beta)$ to both excitation cases considered. These equations are shown on Tables 1 and 2.

TABLE I
DIMENSIONLESS FREQUENCY RESPONSE WHEN THE STRUCTURE IS SUBJECTED TO AN HARMONIC LOADING

	$H_\eta(\beta) = \frac{-\beta^2 B_2 + i\beta B_1 + B_0}{\beta^4 A_4 - i\beta^3 A_3 - \beta^2 A_2 + i\beta A_1 + A_0}$		
Structure	$B_0 = \alpha^2$	$B_1 = 2\xi_p\alpha$	$B_2 = 1$
	$A_0 = \alpha^2$	$A_1 = 2\xi_p\alpha + 2\xi_s\alpha^2$	
	$A_2 = 1 + 4\xi_p\alpha\xi_s + \alpha^2(1 + \mu)$		
	$A_3 = 2\xi_s + 2\xi_p\alpha(1 + \mu)$	$A_4 = 1$	
	$H_\theta(\beta) = \frac{-\beta^2 B_2 + i\beta B_1 + B_0}{\beta^4 A_4 - i\beta^3 A_3 - \beta^2 A_2 + i\beta A_1 + A_0}$		
Pendulum	$B_0 = 0$	$B_1 = 0$	$B_2 = 1$
	$A_0 = \delta\alpha^2$	$A_1 = -2\delta\xi_p\alpha - 2\delta\xi_s\alpha^2$	
	$A_2 = -\delta - 4\delta\xi_p\xi_s\alpha - \delta\alpha^2(1 + \mu)$		
	$A_3 = -2\delta\xi_s - 2\delta\xi_p\alpha(1 + \mu)$	$A_4 = -\delta$	

2) Power spectral density

White noise spectrum is an idealized spectrum that covers the entire range of frequencies like it happens with white light. Although being an idealized spectrum it provides an analytical form for random vibration structures and provides useful approximations of real excitations. It has been widely used to study seismic and wind force vibrations [7].

The optimal parameters of the pendulum TMD in the undamped case of structures subjected to random vibrations can be obtained analytically (frequency ratio, α , and damping ratio for the pendulum, δ). The two necessary conditions for this in each of the cases are given by:

$$\frac{\partial E[\eta^2]}{\partial \alpha} = 0 \quad (12)$$

and

$$\frac{\partial E[\eta^2]}{\partial \xi_p} = 0 \quad (13)$$

where $E[\eta^2]$ is the mean square value of the dimensionless displacement. Solving simultaneously Eqs (12) and (13), it is possible to obtain analytical expressions of optimum parameters.

III. OPTIMAL PARAMETERS REDUCING MEAN SQUARE VALUE

1) Undamped structure subjected to white noise random force

The spectral density function of the excitation $x(t)$ and the spectral density of the response $y(t)$ can be recalled as follow

$$S_y(\omega) = |H(\omega)|^2 S_x(\omega) \quad (14)$$

Thus the mean square value of the response is given by

$$E[y^2] = \int_{-\infty}^{\infty} S_y(\omega) d\omega = \int_{-\infty}^{\infty} |H(\omega)|^2 S_x(\omega) d\omega \quad (15)$$

Considering the two degree-of-freedom system shown in Fig. (1), if the spectral density function of the excitation is a white noise type, $S_x(\omega) = S_0$, the displacement mean square

value is given by

$$E[\eta^2] = \int_{-\infty}^{\infty} S_0 |H_\eta(\beta)|^2 d\beta = S_0 \int_{-\infty}^{\infty} |H_\eta(\beta)|^2 d\beta \quad (16)$$

Considering the equation of $H_\eta(\beta)$, given by Table 1, the integral of Eq. (16) are carried out according to the table given by [10].

TABLE II
DIMENSIONLESS FREQUENCY RESPONSE WHEN THE STRUCTURE IS SUBJECTED TO AN HARMONIC BASE ACCELERATION

	$H_\eta(\beta) = \frac{-\beta^2 B_2 + i\beta B_1 + B_0}{\beta^4 A_4 - i\beta^3 A_3 - \beta^2 A_2 + i\beta A_1 + A_0}$		
Structure	$B_0 = \alpha^2(1 + \mu)$	$B_1 = 2\xi_p \alpha(1 + \mu)$	$B_2 = 1$
	$A_0 = -\alpha^2$	$A_1 = -2\xi_p \alpha - 2\xi_s \alpha^2$	
	$A_2 = -1 - 4\xi_p \alpha \xi_s - \alpha^2(1 + \mu)$		
	$A_3 = -2\xi_s - 2\xi_p \alpha(1 + \mu)$	$A_4 = -1$	
	$H_\theta(\beta) = \frac{-\beta^2 B_2 + i\beta B_1 + B_0}{\beta^4 A_4 - i\beta^3 A_3 - \beta^2 A_2 + i\beta A_1 + A_0}$		
Pendulum	$B_0 = 1$	$B_1 = 2\xi_s$	$B_2 = 0$
	$A_0 = -\delta \alpha^2$	$A_1 = -2\delta \xi_p \alpha - 2\delta \xi_s \alpha^2$	
	$A_2 = -\delta - 4\delta \xi_p \xi_s \alpha - \delta \alpha^2(1 + \mu)$		
	$A_3 = -2\delta(\xi_s + \xi_p \alpha \mu)$	$A_4 = -\delta$	

Solving simultaneously Eqs. (12) and (13) and performing algebraic manipulations the following expressions are obtained

$$\alpha = \sqrt{\frac{2\mu+4}{4\mu^2+8\mu+4}} \quad (17)$$

$$\xi_p = \frac{\sqrt{2}}{4} \sqrt{\frac{(3\mu+4)\mu}{3\mu+2+\mu^2}} \quad (18)$$

3) Undamped structure subjected to white noise random base acceleration

Analogously to the previous case for a two degree-of-system, shown in Fig. (2) subjected to a random base acceleration with white noise spectral density function, $S_x(\omega) = S_0$, the displacement mean square value is given by Eq. (16).

Performing the same optimization described to the white noise random force the following optimum expressions are obtained

$$\alpha = \frac{1}{2} \sqrt{\frac{4-2\mu}{(1+\mu)^2}} \quad (19)$$

$$\xi_p = \frac{\sqrt{2}}{4} \sqrt{\frac{(\mu-4)\mu}{\mu^2-\mu-2}} \quad (20)$$

IV. NUMERICAL STUDY

When taking damping effect into account, it is no longer possible to obtain the analytical solution for the optimum parameters of the pendulum, so in these cases it is necessary to use a numerical search procedure.

This work used MinMax numerical procedure to minimize the maximum amplitude of the frequency response when the structure is subjected to an harmonic force.

Tsai and Lin [9] showed for undamped system cases that the reduction of resonance peak to its lowest value occurs using Den Hartog [11] values, as well as, through MinMax numerical search in which are performed various parameter combinations in order to store those representing the lowest maximum amplitude.

Therefore, repeated tries are performed varying each one of the parameters in the frequency response function, in every try the parameter range to be analyzed is fixed as well as the

discretization of this range. When the numerical search is completed, a new range with values near of those that improve the TMD performance is considered to perform a new try.

The computational routine varies the system parameters (mass ratio, pendulum damping ratio, main structure damping ratio, frequency ratio, forced frequency ratio) and calculates the frequency response function value for each one of the analyzed cases. After it is stored the less response value found in all parameter combinations. The numerical search is ended when all parameters are combined, and the combination that produced the lowest response provides the optimal parameters.

Fig. 3 compares the frequency response obtained to an undamped case using Den Hartog [11] parameters, the

MinMax parameters and considering the uncontrolled case. It can be observed a similar behavior between the two controlled cases.

Vibration amplitudes for damped systems with $\xi_s \neq 0$ don't have the same behavior of the undamped systems. Frequency response curves to different damping ratios don't have fixed points, therefore closed solution for optimal parameters cannot be determined in the same way of the undamped case. However, optimal parameters can be found through a numerical search in a way to minimize the response peak.

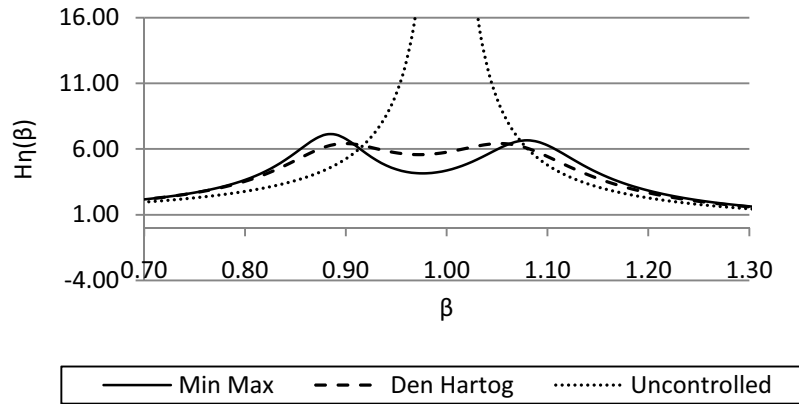


Fig.3 – Dimensionless frequency response of the structure subjected to an harmonic force with Den Hartog and MinMax parameters ($\mu = 0,05$ $\xi_s = 0,00$)

To determine optimal values to $\xi_p, H\eta$ e α to specific values of μ e ξ_s , it is performed a numerical iterative procedure where various values of ξ_p e α are combined on the response function equation in a way to define maximum amplitudes values. Once found and stored the maximum amplitudes, a new search is performed to find the lowest of them, in other words, the parameters that define the minimum maximal amplitudes are found. It is noteworthy that parameters presented on Tables 3 and 4 are general and therefore valid to any structure.

Figs. 4 and 5 compare optimal values of damping ratio (ξ_p), frequency ratio (α) obtained by [9] with the results here obtained varying mass ratio and considering ($\xi_s = 0,02$). It is noticed good agreement between the two analyses.

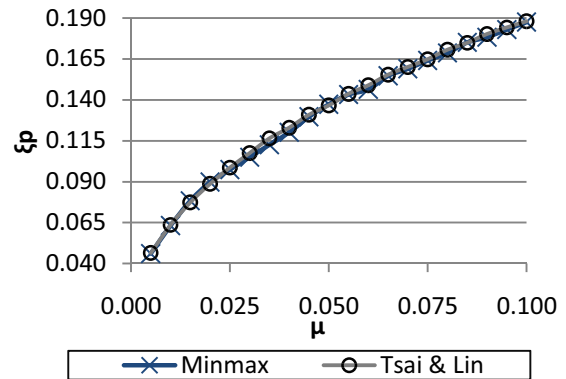


Fig. 4 – Optimaldampingratiocomparison.

TABLE III
OPTIMAL PENDULUM PARAMETERS FOR A STRUCTURE SUBMITTED TO AN HARMONIC FORCE

$(\xi_s = 0,00, \xi_s = 0,02, \xi_s = 0,05 \text{ E } \xi_s = 0,10)$

μ	$\xi_s = 0,00$			$\xi_s = 0,02$			$\xi_s = 0,05$			$\xi_s = 0,10$		
	ξ_p	α	H η									
0,0050	0,0426	0,9952	20,0962	0,0461	0,9930	11,7447	0,0495	0,9875	7,1093	0,0550	0,9740	4,2743
0,0100	0,0616	0,9900	14,1965	0,0632	0,9870	9,4717	0,0675	0,9807	6,2521	0,0700	0,9672	3,9774
0,0150	0,0749	0,9852	11,5941	0,0784	0,9810	8,2800	0,0821	0,9743	5,7197	0,0875	0,9580	3,7668
0,0200	0,0849	0,9805	10,0574	0,0898	0,9760	7,4581	0,0923	0,9683	5,3370	0,0987	0,9511	3,6085
0,0250	0,0954	0,9756	9,0053	0,0974	0,9710	6,8722	0,1024	0,9624	5,0400	0,1095	0,9440	3,4822
0,0300	0,1037	0,9709	8,2303	0,1050	0,9660	6,4228	0,1108	0,9568	4,8000	0,1176	0,9384	3,3735
0,0350	0,1122	0,9662	7,6295	0,1126	0,9610	6,0571	0,1216	0,9512	4,5996	0,1270	0,9314	3,2793
0,0400	0,1207	0,9615	7,1461	0,1202	0,9560	5,7510	0,1273	0,9458	4,4272	0,1323	0,9256	3,1947
0,0450	0,1278	0,9569	6,7459	0,1297	0,9510	5,4910	0,1367	0,9405	4,2785	0,1380	0,9199	3,1219
0,0500	0,1345	0,9523	6,4081	0,1373	0,9460	5,2691	0,1407	0,9353	4,1462	0,1439	0,9139	3,0566
0,0550	0,1399	0,9479	6,1177	0,1433	0,9413	5,0731	0,1478	0,9302	4,0288	0,1520	0,9082	2,9964
0,0600	0,1456	0,9434	5,8648	0,1464	0,9368	4,9020	0,1547	0,9251	3,9234	0,1567	0,9028	2,9413
0,0650	0,1514	0,9390	5,6419	0,1547	0,9320	4,7469	0,1590	0,9203	3,8273	0,1620	0,8973	2,8920
0,0700	0,1562	0,9346	5,4438	0,1590	0,9275	4,6085	0,1643	0,9154	3,7398	0,1705	0,8921	2,8446
0,0750	0,1628	0,9302	5,2657	0,1641	0,9230	4,4827	0,1690	0,9106	3,6595	0,1732	0,8868	2,8017
0,0800	0,1668	0,9259	5,1051	0,1687	0,9185	4,3679	0,1744	0,9059	3,5854	0,1813	0,8816	2,7611
0,0850	0,1723	0,9216	4,9589	0,1751	0,9139	4,2622	0,1781	0,9013	3,5167	0,1834	0,8766	2,7231
0,0900	0,1765	0,9174	4,8253	0,1783	0,9097	4,1653	0,1832	0,8966	3,4527	0,1927	0,8716	2,6875
0,0950	0,1810	0,9132	4,7025	0,1830	0,9053	4,0753	0,1892	0,8920	3,3929	0,1932	0,8668	2,6540
0,1000	0,1859	0,9090	4,5893	0,1875	0,9010	3,9915	0,1925	0,8875	3,3368	0,1972	0,8620	2,6222

TABLE IV
OPTIMAL PENDULUM PARAMETERS FOR A STRUCTURE SUBMITTED TO AN HARMONIC BASE ACCELERATION
($\xi_s = 0,00, \xi_s = 0,02, \xi_s = 0,05 \text{ E } \xi_s = 0,10$)

μ	$\xi_s = 0,00$			$\xi_s = 0,02$			$\xi_s = 0,05$			$\xi_s = 0,10$		
	ξ_p	α	H η									
0,005	0,0438	0,994	20,1853	0,0452	0,9896	11,7928	0,0521	0,9828	7,1268	0,0544	0,965	4,2711
0,010	0,0619	0,9882	14,3966	0,0657	0,9828	9,5354	0,0688	0,9733	6,2864	0,0736	0,9524	3,9841
0,015	0,0737	0,9807	11,8361	0,0767	0,9755	8,3407	0,0798	0,9644	5,7725	0,0889	0,9416	3,7898
0,020	0,0874	0,9759	10,2393	0,0893	0,9688	7,5575	0,0949	0,9568	5,4022	0,101	0,9317	3,6425
0,025	0,098	0,9698	9,1959	0,1007	0,9622	6,9893	0,104	0,949	5,1191	0,1109	0,9222	3,5239
0,030	0,1042	0,9635	8,4149	0,1101	0,9557	6,5511	0,1123	0,9415	4,8914	0,1217	0,9135	3,425
0,035	0,1161	0,9578	7,8331	0,1157	0,949	6,1996	0,122	0,9344	4,7024	0,1296	0,9048	3,3406
0,040	0,1192	0,9518	7,3607	0,1256	0,9429	5,9092	0,1297	0,9273	4,5418	0,138	0,8966	3,2673
0,045	0,1279	0,9461	6,9717	0,1307	0,9365	5,6641	0,1374	0,9205	4,4033	0,1444	0,8884	3,2026
0,050	0,1346	0,9404	6,6461	0,1382	0,9304	5,4532	0,1431	0,9135	4,2821	0,1523	0,8807	3,145
0,055	0,1409	0,9347	6,3675	0,1461	0,9245	5,2703	0,1499	0,9069	4,1747	0,1584	0,873	3,0933
0,060	0,1462	0,929	6,1265	0,151	0,9184	5,1089	0,1563	0,9004	4,0787	0,1655	0,8657	3,0462
0,065	0,1523	0,9235	5,9139	0,1565	0,9124	4,9653	0,1622	0,894	3,9924	0,1704	0,8582	3,0036
0,070	0,1599	0,9181	5,726	0,1619	0,9066	4,8369	0,1699	0,8875	3,914	0,1778	0,8514	2,9643
0,075	0,1653	0,9127	5,5581	0,1693	0,901	4,7209	0,1735	0,8814	3,8424	0,1839	0,8446	2,9284
0,080	0,1703	0,9073	5,4068	0,1728	0,8951	4,6155	0,1794	0,8754	3,7769	0,1883	0,8375	2,895
0,085	0,1746	0,9018	5,2701	0,1788	0,8896	4,5193	0,1841	0,8693	3,7166	0,1943	0,8309	2,8641
0,090	0,18	0,8966	5,1455	0,1833	0,8839	4,4312	0,188	0,8631	3,6609	0,1997	0,8244	2,8355
0,095	0,1845	0,8913	5,0316	0,188	0,8784	4,3499	0,1948	0,8576	3,6092	0,2033	0,8175	2,8086
0,100	0,1893	0,8861	4,927	0,1934	0,87**31	4,2748	0,1998	0,8516	3,5611	0,2098	0,8115	2,7835

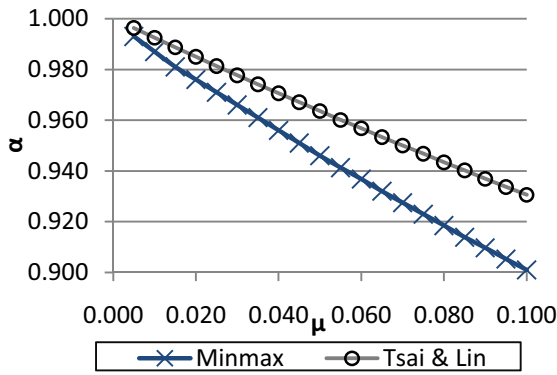


Fig. 5 – Optimal mass ratio comparison

Figs.6 to 9 shows a comparison between optimal parameters obtained via numerical search and those obtained analytically considering the undamped case $\xi_s = 0$, considering the two excitation cases: force and base acceleration.

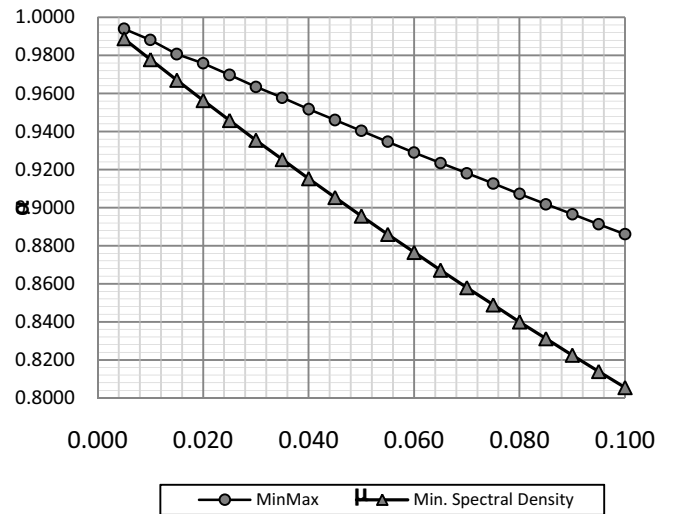


Fig.8 – Optimal frequency ratio (base acceleration)

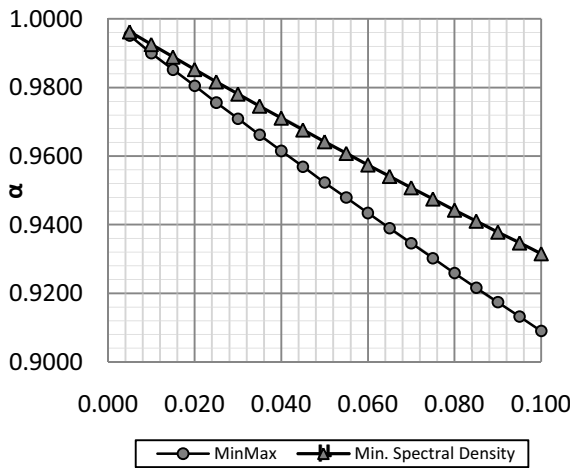


Fig 6 – Optimal frequency ratio (force)

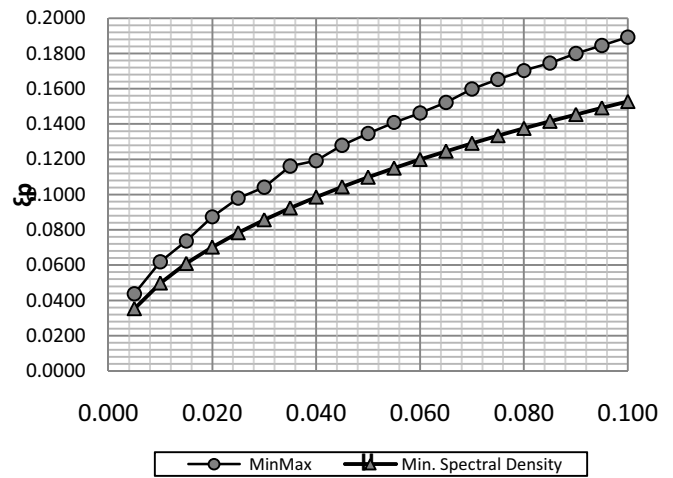


Fig9 – Optimal damping ratio (base acceleration)

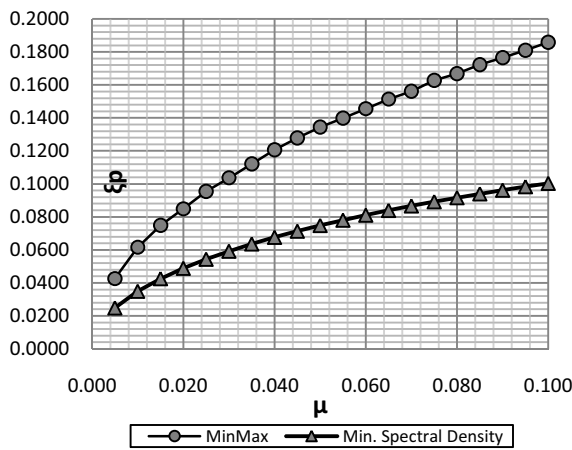


Fig 7 – optimal damping ratio (force)

In a way to verify the pendulum TMD effectiveness using the optimized design criteria, the main structure is subjected to a Kanai-Tajimi spectrum representing random seismic base acceleration.

The power spectral density function of Kanai Tajimi can be interpreted as an ideal white noise excitation filtered by underground soil extracts on site, which is given by

$$S_g(f) = \frac{1+4\xi_g^2(f/f_g)^2}{[1-(f/f_g)^2]^2+(2\xi_g f/f_g)^2} S_0 \quad (21)$$

where S_0 is the white noise spectrum, f the frequency, and ξ_g and f_g are the ground damping and frequency respectively. The values assigned in numerical simulations in this work are: $\xi_g=0.6$ and $f_g= 2.39$ Hz (15 rad/s).

Fig. 9 shows the dimensionless displacement time-history without control and controlled by the two proposed design criteria, considering the structure subjected to records resulting from Kanai-Tajimi spectrum. It can be observed that

the two design criteria lead to very similar response reducing it most of the time analyzed.

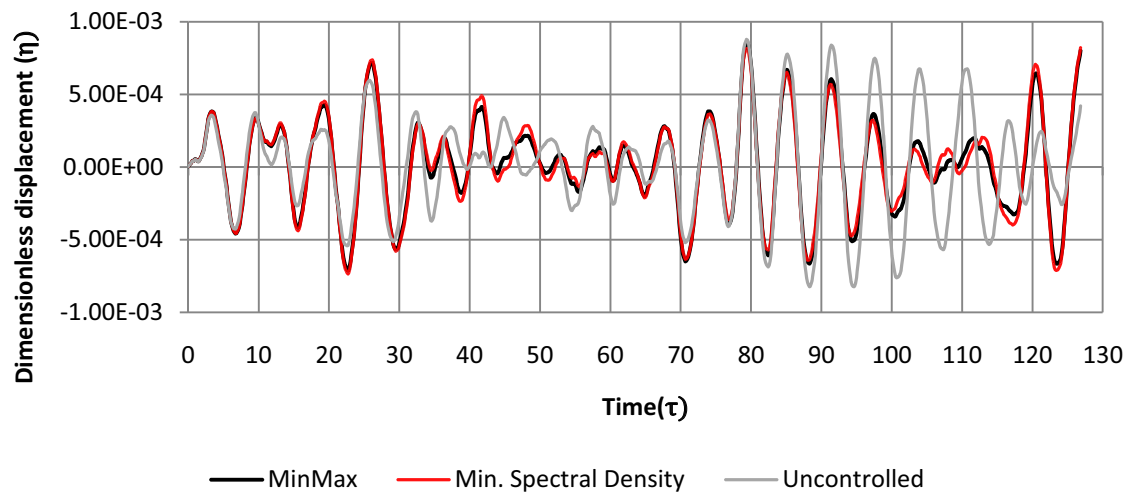


Fig. 10 Dimensionless displacement time-history (Kanai-Tajimi)

V. CONCLUSIONS

The TMD optimization aiming to reduce response function amplitude to an undamped structure subjected to an harmonic force was originally performed by Den Hartog [11]. However, all types of structural systems have some level of damping, moreover civil structures are subjected to random loads such as wind forces and earthquakes. An alternative geometry to the auxiliary system of the TMD is a pendulum, which fits very well to be installed in high buildings in practice. This work proposes design criteria to TMD pendulum types installed on high buildings subjected to different types of deterministic and random loadings. Performing minimization procedures a set of optimal parameters depending on the mass and damping of the main structure are proposed. It is noteworthy that parameters presented are valid to any tall building. It was verified that Minmax procedure is an efficient tool to pendulum TMD optimization. Using the suggested parameters in this work will improve considerably pendulum performance on reducing amplitude vibrations.

VI. REFERENCES

- [1] S. M. Avila, "Hybrid control for vibration attenuation in buildings", PhD thesis, Catholic University of Rio de Janeiro, Rio de Janeiro, Brazil, 2002. (In Portuguese)
- [2] T. T. Soong, T. T. and G. F. Dargush, *Passive Energy Dissipation Systems in Structural Engineering*. Chichester: John Wiley & Sons, 1997.
- [3] R. B. Carneiro; S. M. Avila and J. L. V. Brito, "Parametric study on multiple tuned mass dampers using interconnected masses", *International Journal of Structural Stability and Dynamics*, vol. 8, pp. 187-202, 2008.
- [4] F. S. Oliveira, "Design Criteria for Pendulum Type Absorber for Vibration Control in Tall Buildings", Master's Dissertation – Dep. of Civil Eng, University of Brasilia, 2012. (In Portuguese)
- [5] R. Lourenco, "Design, Construction and Testing of an Adaptive Pendulum Tuned Mass Damper", Master's Dissertation - Waterloo, Ontario, Canada, 2011.

- [6] D. Orlando and P. B. Goncalves, "Hybrid nonlinear control of a tall tower with a pendulum absorber", *Structural Engineering and Mechanics*, vol. 46, pp. 153-177, 2013.
- [7] R. R. Gerges and B. J. Vickery, Optimum design of pendulum-type tuned mass dampers. *The Structural Design of Tall and Special Buildings*, vol. 14(4), pp. 353-368, 2005.
- [8] M. Morga, and G. C. Marano, "Optimization criteria of TMD to reduce vibrations generated by the wind in a slender structure", *Journal of Vibration and Control*, v.0(0), pp. 1-13, 2013 (published online).
- [9] H. C. Tsai and G. C. Lin, "Optimum tuned-mass dampers for minimizing steady-state response of support-excited and damped systems", *Earthquake Engineering and Structural Dynamics*, vol. 22(11), pp. 957-973, 1993.
- [10] Crandall S. H. and Mark M. D., *Random Vibration in Mechanical Analysis*, Academic Press, 1963
- [11] J. P. Den Hartog, *Mechanical vibrations*. McGraw-Hill, New York, 1956.

Seismic Performance of a Tall Diagrid Steel Building with Tuned Mass Dampers

Andre R. Barbosa*¹, and Garlan Ramadhan**²

¹Assistant Professor, School of Civil and Construction Engineering, Oregon State University, Corvallis, OR 97331, USA

²Graduate Student, School of Civil and Construction Engineering, Oregon State University, Corvallis, OR 97331, USA

*andre.barbosa@oregonstate.edu, **garlan.ramadhan@gmail.com

Abstract— The steel diagrid structural system is a recent load bearing and lateral resisting structural system for tall building structures that is relatively unexplored in the western United States. One possible reason for the little use of diagrid systems in earthquake prone regions is the lack of guidelines and application examples illustrating the design and analysis of these structures. In this work, a 72-story prototype building is used as an example for which the design and analysis of the diagrid system is performed. To mitigate the possible large displacement and base shear demands that these structures may undergo under seismic events, two new design solutions consisting of one or two friction tuned mass damper (TMD) units are explored. In the first solution, a TMD is placed on the top four stories of the building and is tuned to reduce the contribution of the fundamental mode of vibration of the structure, in both horizontal directions. In the second solution, a double TMD system is added at mid-height of the building, in which a second TMD unit is tuned to the second period of the structure.. Using a nonlinear finite element model of the tuned mass damper, the effectiveness of the friction mass damper design is studied. The mass damper system consists of a concrete tank containing sand or water. The tank is placed in between the building reinforced concrete structural core and the exterior steel diagrid system. This mass damper is connected to the structure using friction pendulum isolators that are chosen due to their ability to undergo large deformations. The models are then subjected to accelerograms from historical shallow crustal earthquakes and subduction zone earthquakes. Parametric studies are carried out to understand the influence of different parameters of the mass damper design in improving the seismic performance of the building. Improvement of the seismic performance is assessed in terms of minimization of inter-story drift ratios, base shear forces, as well as floor absolute accelerations. The results show that the single TMD system can reduce significantly the peak base reaction and inter-story drift envelopes. Addition of the second TMD provides further improvements in terms of reducing the peak base reactions, while also producing notable reductions in peak absolute floor accelerations, which are not observed when only one TMD unit is used.

Keywords— Cascadia Subduction Zone Earthquakes, Diagrid, Earthquakes, Friction Pendulum Isolator, Nonlinear Structural Analysis, Seismic Design, Steel Structures, Tall Buildings, Tuned Mass Damper.

I. INTRODUCTION

THE FIRST tall buildings were built in United States of America in the late nineteenth century [1]. There is no set definition for what constitutes a tall building, but often buildings that are 14 stories or more are considered as tall

buildings (50 m or taller). At present times, many tall buildings have been built around the world and The Council on Tall Buildings and Urban Habitat contains information on more than ten thousand tall buildings [2]. Several structural systems have also been developed to realize mankind's dream in pursuing new heights and allow for the design of tall buildings. Out of many structural systems, the outer steel diagrid structural system with reinforced concrete inner core is but one of them. The diagrid structural system gets its name from the diagonal columns that form triangular trusses. Diagrid is an abbreviation for "diagonal grid" of trusses. The diagonal trusses are connected by horizontal rings (steel beams), which provide support for the floors and column buckling restrains. The diagonal members carry gravity loads as well as lateral loads, and thus steel is typically used in diagrid structures. The main difference between conventional steel exterior-braced frame trusses (X, K, V, and Chevron type braces) is that in the diagrid structural system almost all vertical columns are typically eliminated. The interior reinforced concrete core typically consists of walls and is designed not only to resist lateral loading, but also to allow for the vertical communication and transport of people (elevator shafts and stairwells), heating, ventilation, and air conditioning, plumbing, electrical, and fire protection systems.

The diagrid structural system is known for its redundancy, continuous and uninterrupted load paths, and is thus considered to be a very efficient structural system [3]. However, these efficiencies also come with drawbacks. Most new structures that have been designed and built using this system are lighter and more flexible than conventional tall building systems, and thus can suffer large displacements, especially under wind and seismic loading. Some prime examples of this kind of structures are the Hearst Tower, in New York City, the China Central Television (CCTV) Headquarters in Beijing, China, and the Tornado Tower in Doha, Qatar.

The diagrid structural system is relatively new and unexplored in the Western United States and other high-seismic regions of the world, and hence engineers lack the guidelines and examples that can be used to promote the design of tall buildings using such a structural system. This paper addresses this gap in the literature, as the main objective of this paper is to provide an example in the design and analysis of diagrid structural systems for seismic regions, by

discussing and studying the sensitivity of solutions using tuned friction mass dampers to mitigate seismic demands on the structure.

In this study, a prototype 72-story building is developed. For the seismic design, the focus is placed on mitigating large displacements and shear forces that may appear in these structures. First, a system using a single tuned mass damper (TMD) unit placed at the top of the building is explored. The mass damper is connected to the structure with friction pendulum isolators, which are chosen due to their ability to undergo large deformations. A parametric study is carried out in order to optimize the mass damper design in terms of improving the seismic performance of the building structure. Second, the performance of a double tuned mass damper system is also investigated. In this system, an additional TMD unit is installed at mid-height of the building. In all, this paper provides a first example, which serves as guidance into design of diagrid structures in regions prone to seismic loading, including single or double tuned mass damper systems.

The building studied herein is designed for a location in downtown Seattle, Washington, USA and thus both shallow crustal earthquake motions as well as subduction zone earthquake motions are used in the analysis. Shallow crustal motions are typical of what is generated in intracontinental faults, while subduction zone motions are often generated in intercontinental faults [4]. Since a preliminary deaggregation of the seismic hazard for this site showed that the seismic hazard is contributed equally by crustal and subduction earthquakes, the same number of records (7+7) is used in this study. According to past research [5], the peak displacement demands obtained from using both types of motions are mostly identical, but the subduction zone motions induce a much larger number of inelastic excursions indicating that structures excited to these long-duration motions must be carefully designed to avoid low-cycle fatigue.

II. SOLUTIONS FOR IMPROVING SEISMIC PERFORMANCE OF DIAGRID STEEL STRUCTURES

Two main systems have been proposed to date to improve the seismic performance of the diagrid system, including the use of base isolation or viscous dampers. In a first alternative, Arup (2009) [6] proposed a diagrid structure combined with a base isolation system as a method for reducing the potential for damage induced by earthquake shaking. In this solution, a 20-story office building was completed in 2006 in Sony City, Japan. The isolation solution was effective since the period of the base isolated building was shifted and the seismic lateral forces applied to the structure were substantially reduced. Base isolation typically adds 5% of the construction cost [7], even after considering the reduction in structural material in the superstructure. The extra cost arises due to the extra floor structure that needs to be constructed in between the building and the foundation in support of the base isolators. Furthermore, design of services and elevator shafts, passing through the isolation requires careful design for allowing for the lateral movement between the foundation and the isolated structure. In a second alternative, Lago et al. (2010) [8]

proposed a vertically distributed isolation system. In this solution, the diagrid exterior structure was isolated from the main seismic mass of the building interior along the height of the structure. The distributed isolation was achieved by attaching viscoelastic dampers between floor diaphragms and horizontal rings of the diagrid structure. Lago et al. showed that this system has the potential to significantly reduce the damage to the architectural façades.

Even though the two systems described in the previous paragraph are unique and have several advantages for mitigating seismic demands, they are not suited for very tall building structures. The base isolation system is only effective for relatively stiff structures, since the period of the base isolated structures is typically set in the 2.0 sec to 3.0 sec range [9]. Tall building structures are typically very flexible and often have fundamental periods close to and above 5.0 sec and therefore the base isolation system is not effective. Following similar discussions, Lago et al. also stated that the vertically distributed isolation system is not effective for tall building structures. Based on numerical results, the authors showed that for a 20 story building the dampers had already experienced a stroke on the order of 0.8 m. Any form of extrapolation to the prototype 72-story building studied herein, would translate roughly to the need for dampers with approximately 4 m in length, which is beyond the scope of the proposed solutions.

Herein, a third alternative for mitigating seismic demands is proposed for use in tall buildings consisting of a diagrid structural system, which makes use of tuned mass dampers (TMDs) to mitigate lateral motion due to earthquake excitations at the base. Even though the particular system being proposed is new and the application of this new solution in diagrid systems has never been proposed, the concept of using TMD units have been applied in many skyscrapers built around the world. Examples are: (i) Taipei 101 in Taipei, Taiwan; (ii) One Wall Centre Hotel in Vancouver, Canada; and (iii) Shanghai World Financial Center in Shanghai, China. The TMD systems installed in these three buildings are all unique. Taipei 101 featured the heaviest TMD in the world with 660 metric-tons; the One Wall Centre fosters a tuned liquid (water) damping system; and the Shanghai World Financial Center holds a double TMD system. In these three building designs, the TMDs were installed at the top of the buildings and were shown to successfully mitigate the effects of the lateral loading. The TMD concept in this paper is somewhat similar to the used in the One Wall Centre Hotel [10]. Further explanation of the concept and its modeling details are provided in the following sections.

III. TUNED MASS DAMPERS AND IMPLEMENTATION

Tuned mass dampers (TMDs) have been studied extensively by many researchers (e.g. Chopra 2001 [11], Inaudi and Kelly 1992 [12]). TMDs are placed in structures to improve their performance by providing counteracting (out-of-phase) forces that mitigate the vibration response of the original structure. Earlier studies included implementation of single mass damper units to mitigate wind-induced vibrations of building

structures [13]. In the literature (e.g. Sadek et al. 1997 [14], Hadi and Arfiadi 1998 [15]), researchers have tuned the mass dampers by adjusting the stiffness and damping of the device or the mass of the TMD unit. In most cases in which TMDs have been used in buildings, these were placed near the top of buildings. The utilizations of multiple TMD units have also been discussed. To the authors's knowledge, the pioneering work by Xu and Igusa (1992) [16] proposed the first system with multiple damped oscillators and showed that multiple TMD units can be more effective than a single TMD with the same mass in mitigating vibrations induced motion (displacements). Chen and Wu (2001) [17] showed that multiple dampers are strictly necessary if the objective is to also reduce peak floor absolute accelerations of the building structure to impulsive (seismic) loading. Nonetheless, Lucchini et al. (2013) [18] concluded that the effectiveness of the TMD solutions consisting of two units is reduced if the uncertainty in the characteristics of the earthquake are considered.

IV. FRICTION PENDULUM ISOLATORS

The TMDs solutions proposed in this study are supported on friction pendulum system (FPS) isolators [19]. The FPS isolators consist of a spherical sliding surface, which realize a pendulum system with a fundamental period that is related essentially to the length of the pendulum and radius of curvature of the pendulum. This is one of the unique characteristics of the FPS isolators, in which the fundamental period of vibration is essentially independent of mass. The dynamic response is strictly related to the friction characteristics of the sliding (curved) surfaces. In the interest of conciseness, the reader is directed to [19] for more details on FPS isolators, which are well-established for use in mitigating seismic demands in building and bridge structures. In this study, the computational model used to characterize the dynamic response of the FPS consists of a gap in the axial direction coupled the friction properties for two shear deformations with post-slip stiffness in the shear directions due to the radius of the sliding surfaces, and linear effective-stiffness properties in the torsional deformation. This friction model is based on the one proposed by Wen (1976) [20] and Park et al. (1986) [21]. The pendulum local axis of 1, 2, and 3 correspond to the global Z, X, and Y direction, respectively. More details on the modeling approach used are described by Ramadhan (2013) [22].

V. METHODOLOGY

A. Building Design

A 72-story prototype building with uniform floor height of 4 meters was designed following current US codes and standards for component design verification. This building is assumed to be located in Seattle, Washington, USA. The assumed latitude and longitude are $47^{\circ}36'17.43''\text{N}$ and $122^{\circ}19'51.88''\text{W}$, respectively. As shown in Fig. 1, the building has a $36\text{m} \times 36\text{m}$ floor plan and floors are supported by diagonal columns that cross every four floors. With this

configuration, the diagonal columns form isosceles triangles with an angle of 69° . This is the optimal configuration for slender diagrid structures greater than 60 stories according to empirical studies carried out by Moon (2008) [23]. All beams, except horizontal rings in floor diaphragms, are designed to carry gravity load only, and thus are designed and modeled as pin-connected at both ends.

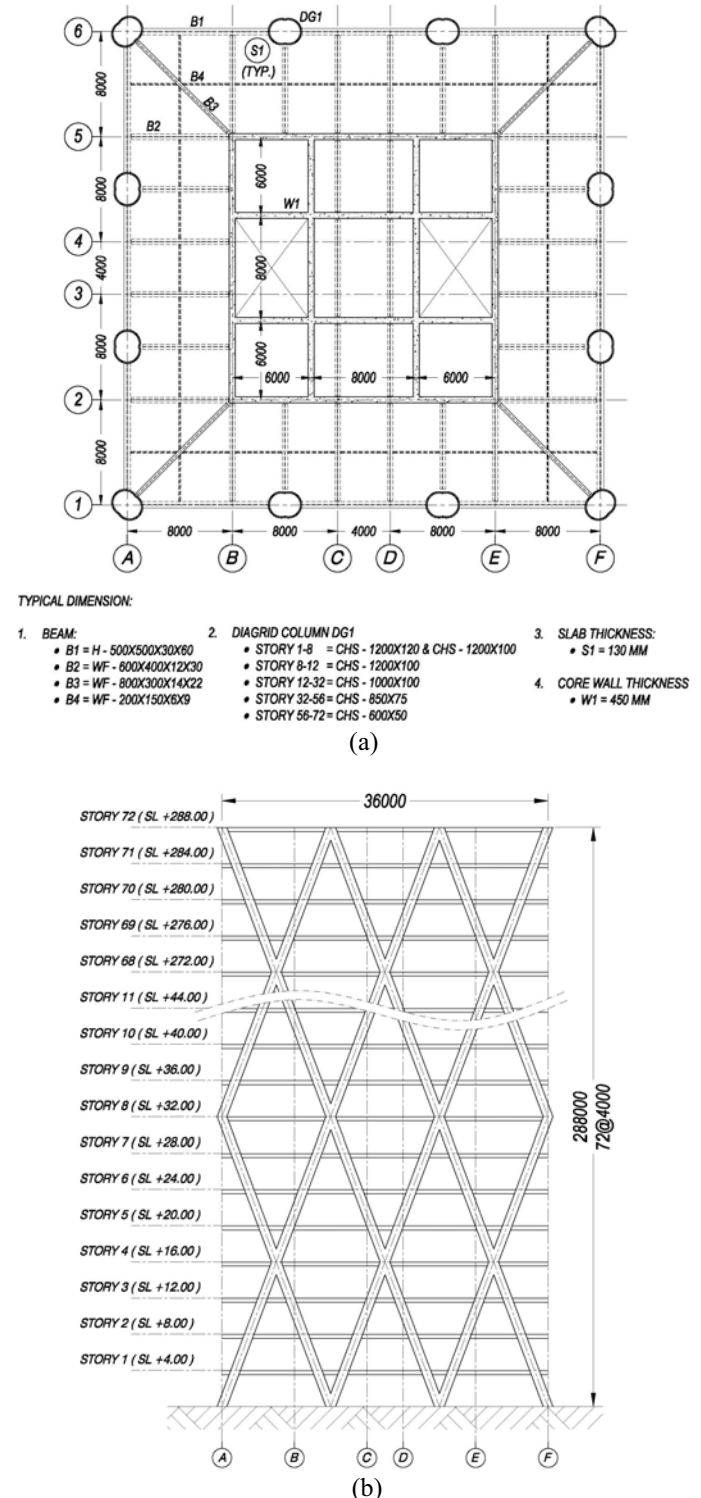


Fig. 1. Prototype building drawing: (a) plan view, (b) truncated elevation view; all dimensions are in mm.

A two staged design and design verification was performed: (1) In a first stage, the building was designed not considering the effects of the TMDs. Models of the building were developed and dimensions of all components of the building were first estimated using engineering judgment. Final dimensions were obtained through an iterative design process, in which the forces and displacements in the building were obtained using the response spectrum method for the prototype building (without the TMD units); (2) In a second stage of the design, the friction TMD system was incorporated to the model and design obtained in the previous model. In this second stage, nonlinear models were considered for the TMD units, and therefore the response spectrum method was not valid for use. Instead, nonlinear time-history response analysis was performed as described next in this methodology section. It is worth noting that the finite element models used are also described next.

B. TMD Unit Design

The TMD units consist of a concrete container with sand or water inside it, which is connected to the main structure using friction pendulum isolators. A similar concept to the one proposed herein can be found in One Wall Centre Hotel in Vancouver, Canada, which holds a tuned water damping system at the top level of the building [10]. The volume of sand or water can be adjusted according to optimal mass obtained from modeling and analysis. The reference model has the friction TMD unit placed at story 68 to alleviate the response from the first mode of the structure as shown in Fig. 2a.

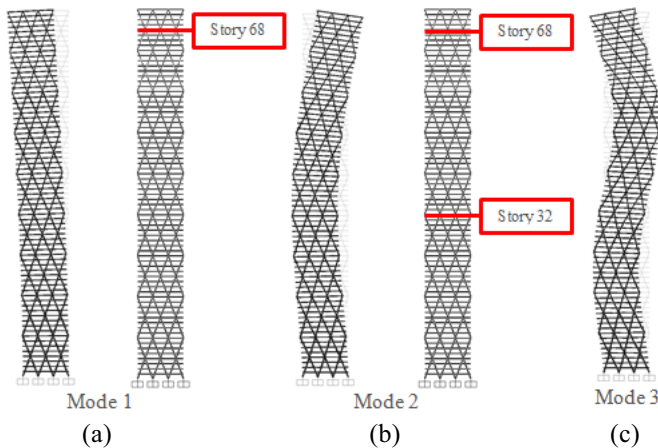


Fig. 2. Mode shapes of the original structure and mass dampers placement: (a) Mode 1 and solution with only one TMD unit, (b) Mode 2 and solutions with two TMD units, (c) Mode 3.

The top friction TMD unit extends from story 68 to story 72 to provide improved load transfer from the mass damper to the stiffer floors, that is, floors at which the diagonal columns of the diagrid cross. It also serves as a room for the additional required mass that is provided by the sand or water. This TMD unit is illustrated in Fig. 3. For the model with two friction TMD units, the first unit is the same as the reference model, while the second is placed at story 32, extending to story 34.

The second TMD unit is illustrated in Fig. 4. Implementing the second mass damper unit aims at reducing the contribution of the second lateral mode of vibration (see Fig. 2). Due to the usual shape of the seismic design response spectrum (as well as the shape of the response spectra of the ground motions considered) base shear forces due to the second mode (or even the third mode) have significant contributions to the floor accelerations and to the total base shear, as confirmed in the results section.

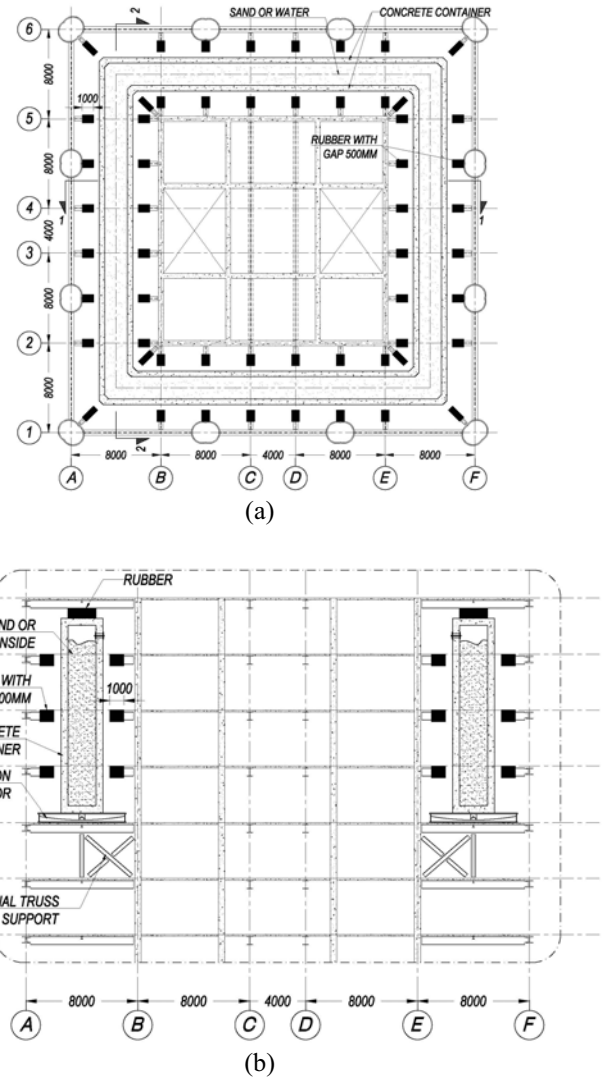


Fig. 3. First TMD unit: (a) plan view at story 69 to 71, (b) cross section 1-1. All dimensions are in mm.

Protective shock absorbers (rubber bearings or an equivalent system) are placed between the outer horizontal rings of the exterior diagrid and the TMD units. These bearings are also placed between the TMD units and the inner reinforced-concrete core. In the reference model, the TMD unit (at story 68) has absorbers – with thickness of 1 meter – placed in stories 69, 70, and 71. Initial gaps of 500 mm are provided, and absorbers are only engaged after the gaps are closed. For the model with double TMD units, the second TMD unit (at story 32) has absorbers – with thickness of 1.5

meters – placed at story 33. The second absorbers do not have gaps. This allows for tuning of the period of the second mass damper to be close to the second mode of the building. Absorbers are also placed above the container to prevent impact due to overturning. Lastly, additional stiff truss beams are provided at the floor below the TMD units, to transfer the vertical loads directly to the inner core. The design of the braces was done to ensure that the solution was possible.

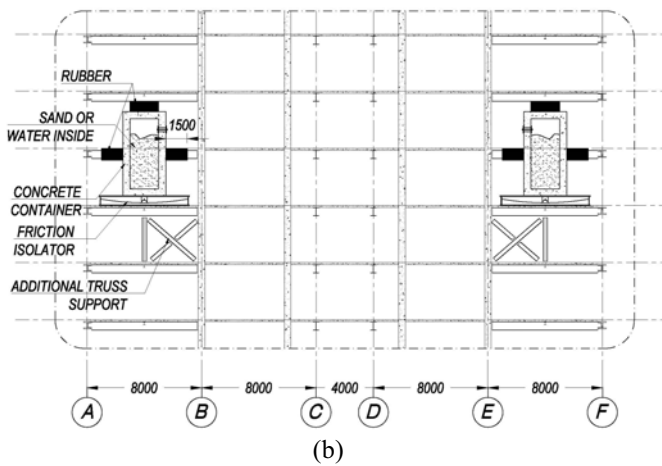
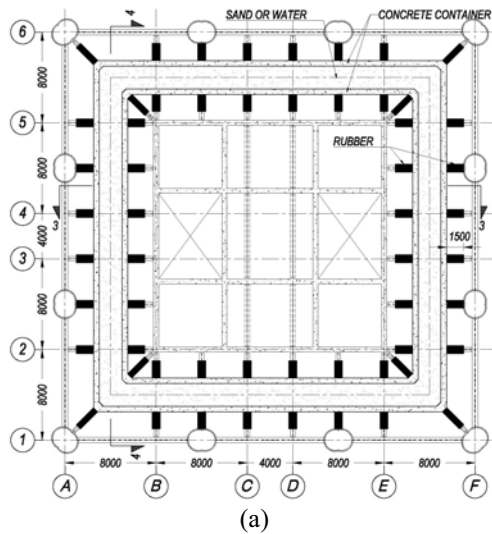


Fig. 4. Second TMD unit: (a) plan view at story 33, (b) cross section 3-3. All dimensions are in mm.

C. Ground Motion Selection

The selection and scaling of horizontal component ground motion acceleration time histories are crucial to produce meaningful results and adequate comparisons of the responses of structures subjected to these ground motions. The selection performed herein has the primary objective of producing acceleration histories which are consistent with the seismic hazard at the site.

Seven (7) crustal earthquakes, listed in Table I, were chosen and scaled from the 2011 PEER Ground Motion Database. The target spectrum is based on ASCE 7-10 [24] with design earthquake spectral response acceleration parameters, $S_{ds} = 0.911g$, $S_{d1} = 0.529g$, and $T_L = 6$ sec. The target design

response spectrum is shown in Fig. 5 and Fig. 6. The Pacific Earthquake Engineering Research Center (PEER) Center makes a ground motion database available and has a web tool linked to it for selection and scaling of acceleration time histories [25]. In the selection of the earthquake records, some parameters have to be input in the web tool. Readers are referred to the PEER manual for details on all the variables described next. The range of earthquake moment magnitudes is set to $M_w = 6$ to 7.25. D_{5-95} , which is the time duration for the intensity to rise from 5% to 95% is set to 0 to 300 seconds. Joyner-Boore distance (R_{JB}) and the rupture distance (R_{rup}) is set to 0 to 20.5 km. The range of average shear wave velocity in the top 30 m of soil (V_{s30}) is set to 190 to 350 m/s. The scale factor, for linear scaling of the ground motion records, is limited to 1/3 to 3.0. Lastly, the root-mean-squared errors (RMSE) between the ASCE7-10 target response spectra and the geometric mean of 5%-damped linear response spectra obtained for two orthogonal directions are used as a measure of goodness-of-fit. The RMSE are assessed in periods ranging between 1.0 second and 10 seconds, which covers a range below 0.2 and 1.5 of the fundamental period of the building structures analyzed herein. Fig. 5 shows the target spectrum as well as geometric mean of the selected response spectra of scaled acceleration time histories. The records selected for the crustal shallow motions are listed in Table I. It is worth noting that these records have the lowest root-mean-squared errors between the target response spectra and the response spectra of all ground motion records, and had the lowest usable frequency with a maximum value of 0.12 Hz (8.33 s).

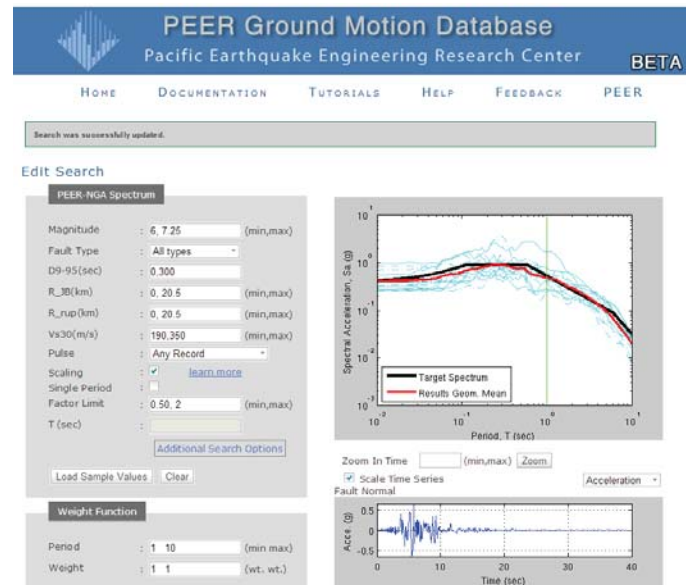


Fig. 5. Input parameter for selecting and scaling the earthquake time series in PEER ground motion database.

Seven (7) subductions earthquakes, shown in Table II, were chosen and scaled from Japan [26] using the method described in [27]. Those 7 earthquake records are obtained from the “2011 Tohoku Earthquake” of March 11, 2011. The response spectra for all selected earthquakes are shown in Fig. 6. It is

worth noting that prior to this earthquake event, only very limited data was available for large magnitude earthquake motions, especially for the very large period range of interest of the building structure in analysis. Thus, all motions were selected from a single earthquake event, which may induce some bias in the results. From the database of Japanese ground motions used, there are a very small number of records that could be used for the analysis in this study due to the very large fundamental period of the tall structures. A minimum value for the lowest useable frequency was set to 0.12 Hz (highest useable period is $T = 8.33$ s), which allows for analyzing these tall building structures will a large degree of confidence. Often, two different components of the same earthquake need to be filtered using different corner frequencies. Thus, the records shown in Table II are applied to the two horizontal directions of the building, which was the basis for selection of the ground motions. Finally, it is worth noting that the records for the subduction earthquakes chosen herein have larger RMSE than the shallow crustal motions.

TABLE I
Properties of selected crustal earthquake records obtained from [25].

Event	Imperial Valley-06	Imperial Valley-06	Duzce-Turkey	Imperial Valley-06	Northridge-01	Imperial Valley-06	Northridge-01
Year	1979	1979	1999	1979	1994	1979	1994
Station	El Centro Array #8	Brawley Airport	Duzce	El Centro Array #10	Newhall - W Pico Canyon Rd.	Parachute Test Site	Newhall - Fire Sta
NGA#	183	161	1605	173	1045	187	1044
Scale Factor	1.194	1.986	0.743	1.479	0.906	2.000	0.911
RMSE	0.015	0.027	0.039	0.046	0.248	0.267	0.271
Pulse (FN/FP)	Yes/No	Yes/No	No/Yes	Yes/Yes	Yes/Yes	No/No	Yes/No
TP (FN/FP)*	5.4/--	4/--	--/5.6	4.5/2	2.4/2.2	--/--	2.2/--
Magnitude	6.53	6.53	7.14	6.53	6.69	6.53	6.69
Mechanism	Strike-Slip	Strike-Slip	Strike-Slip	Strike-Slip	Reverse	Strike-Slip	Reverse
Rrup (km)	3.9	10.4	6.6	6.2	5.5	12.7	5.9
Corner Freq**	0.12	0.12	0.1	0.12	0.12	0.12	0.12

*TP is pulse period in seconds as defined by Baker (2007) [28].
*lowest usable frequency.

TABLE II
Properties of selected subduction zone earthquake records obtained from [26].

Event	Tohoku Earthquake						
Date	March 11, 2011						
Station	11031114-46	11031111-446	11031111-446	11031111-446	11031111-446	11031111-446	11031111-446
File Name	AOMH16-EW-Surface	FKSH10-EW-Surface	FKSH16-NS-Surface	FKSH20-EW-Surface	IWTH11-NS-Surface	IWTH24-NS-Surface	TCGH16-NS-Surface
Scale Factor	3.000	3.000	3.000	1.252	3.000	2.806	1.573
RMSE	0.606	0.520	0.667	0.823	0.778	0.173	0.356
Magnitude	9.000	9.000	9.000	9.000	9.000	9.000	9.000
Corner Freq	0.120	0.120	0.120	0.100	0.080	0.090	0.100

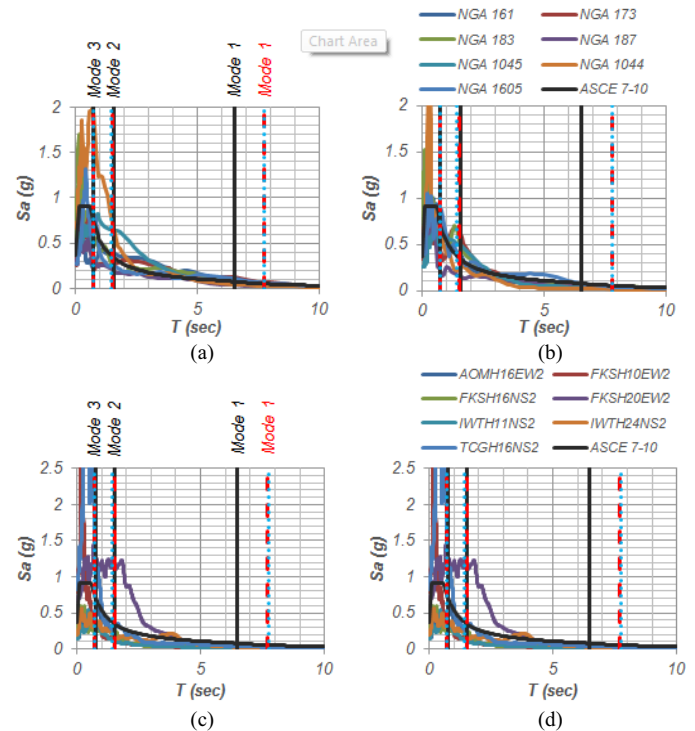


Fig. 6. Response spectrum of each tested ground motions: (a) crustal – fault normal applied in X-dir, (b) crustal – fault parallel applied in Y-dir, (c) subduction – applied in X-dir, (d) subduction – applied in Y-dir; straight line legend: (i) without TMD [–], (ii) reference model (with TMD) [– –], (iii) with double TMD units [· · ·].

D. Modeling

Structural modeling corresponds to the creation of a mathematical model that can be solved and analyzed. In this paper, SAP2000 [29] is the software used to analyze all building structural models. Sap2000 uses the finite element method to model all structural elements in the building. The diagrid structure is modeled using linear elastic frame elements with geometric and mechanical properties defined based on Fig. 1a. The inner reinforced concrete wall core is modeled using linear elastic shell elements. The effective Young’s modulus of the walls is taken as 35% of the nominal concrete modulus E_c . Floor diaphragms consist of a grid of steel beams supporting a concrete slab, which are modeled as rigid diaphragms for lateral loading. The effective Young’s modulus of the floor slabs are taken as 25% of the nominal concrete modulus in accordance to ACI 318-11 [30] section 10.10.4.1. Additional plan eccentricities in this regular prototype structure were not explicitly considered. The SAP2000 model of the prototype building consists of 8536 frame elements, 60275 joints, and 57624 shell elements. The total number of degrees of freedom in the model is exceeds 360,000.

For modeling purposes, the concrete container (with its content) is represented by a single wall, which is placed at mid-distance between the outer diagrid and the inner core. The single wall is modeled as linear elastic shell elements with thickness and mass defined as to represent the container and its content. It should be noted that sloshing effects of the water surface is neglected as it will not have a considerable effect in

seismic loads and performance of the TMD. In the reference model, the ratio between the mass of the TMD unit and the mass of the main structure is approximately 4.7%. For the model that has two TMD units, the second TMD unit has approximately half the mass of the first.

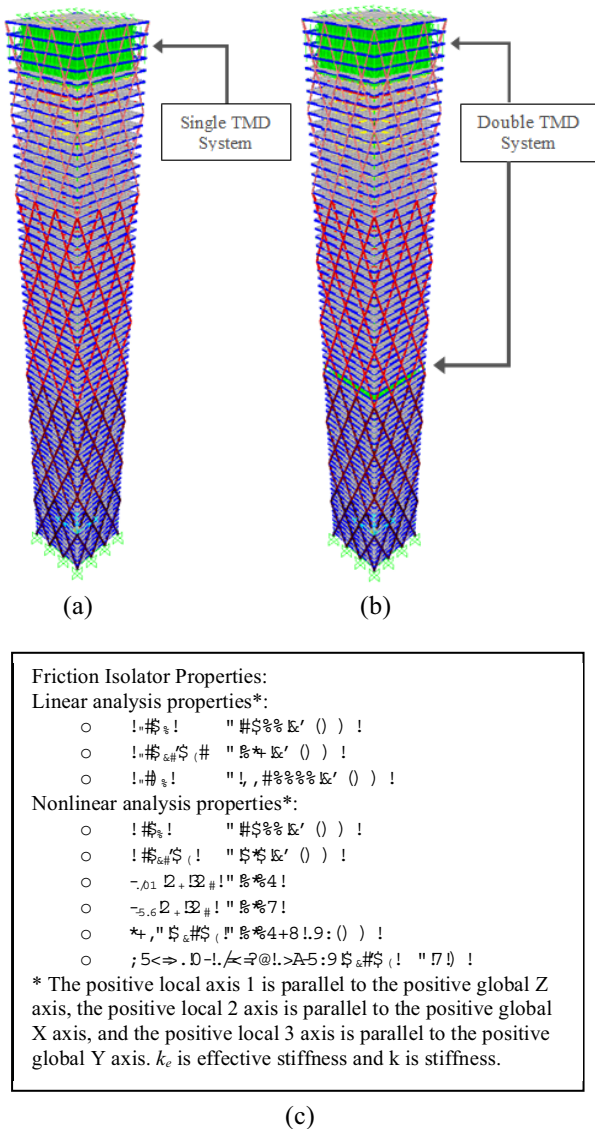


Fig. 7. Building model in SAP2000: (a) with single friction TMD unit, (b) with double friction TMD units, (c) friction isolator properties.

The material nonlinearity in this model was only explicitly considered in the links provided between the TMD and the main structure. A total of 392 links were placed in the model for each TMD unit. These nonlinear links simulate: (i) the friction pendulum isolator; (ii) the shock absorbers; and (iii) gap springs. First, in the definition of the links for the friction pendulum isolators, the model by Scheller and Constantinou (1999) [31] was chosen as the preferred model. Full details on the behavior of the FPS modeled using the friction isolator is available in the referred publication. The properties for all friction isolator links in the reference model are listed in Fig. 7. Second, linear springs were provided for the shock

absorbers, with stiffness values of 1 kN/mm. Lastly, two types of gap links were provided – in parallel to each other – representing the shock absorbers. The first gap link corresponds to a gap of 500 mm followed by a linear elastic stiffness branch. The second gap link has a gap of 1500 mm, followed by a large stiffness to model contact between the TMD and exterior structure. The stiffness of the first gap links is 1 kN/mm with 500 mm opening (707.1 mm for diagonal links). The stiffness of second gap links is 2449 kN/mm (1725 kN/mm for diagonal links) with 1500 mm opening (2121.3 mm for diagonal links). The stiffness of the second gap link is proportional to the length of the beam member which the rubber is attached to. The behavior of absorbers for the second TMD unit are almost the same as the first, except the first gap links are replaced by uniaxial springs with stiffness values of 1 kN/mm.

E. Analysis Methodology

The nonlinear finite element analysis of the models is divided into three stages. In the first stage a linear static analysis of gravity loads and wind loads (for design verification only) are applied to the building. The second stage involves performing an eigen analysis to compute natural frequency, mode shapes, and mass participation ratios of the building models following a gravity load analysis. In the design verification of the prototype building (without TMDs), the third stage corresponds to performing a response spectrum analysis, using the appropriate target spectrum for analysis of mainly steel structures as the input. For models with TMD units, the third and final stage includes the nonlinear time-history analysis for computing the response of the building to the applied earthquake acceleration ground motions time-histories. Duration of analysis was at least the duration of the accelerograms and integration time step of 0.005 second was used for computing the building’s responses to shallow crustal motions. On the other hand, the building’s responses to subduction earthquake records are computed with analysis duration of 350 seconds and integration time step of 0.005 second. These time steps used herein provide sufficient accuracy in the displacement responses for the structure with the large fundamental periods, while the duration of the analysis is done to allow for the free-vibration period post-earthquake. Constant acceleration Newmark integration was used for numerical time integration, and Newton-Raphson was used to solve the nonlinear system of equations. Structural constant damping is set to be 2% for all modes.

F. Parametric Studies

There are 4 variables addressed in this research: friction coefficients of the TMD unit, height distribution of the TMD, mass of the TMD, and number of TMD units. In each model, 7 shallow crustal motions and 7 subduction zone motions are applied to the models. Each of the crustal motions has three components of acceleration time series and they are assigned randomly in either X- or Y- directions. Vertical components of motion were also used. The properties of each of earthquake record are listed at section V.C.

In all, the number of nonlinear time history performed for this parametric study (tornado type analysis) is 98 [14×(1+2+1+1+2)] analyses. The perturbations from reference models are:

- (A) 3 levels of friction coefficient values for parametric studies are: (i) $f_{slow} = 0.01, f_{fast} = 0.02$; (ii) reference ($f_{slow} = 0.04, f_{fast} = 0.06$); (iii) $f_{slow} = 0.08, f_{fast} = 0.12$;
- (B) 2 levels for height distribution of the TMD: (i) 4 stories (reference); (ii) 2 stories;
- (C) Mass of the TMD (3 levels): (i) reference; (ii) increase by 20%; (iii) decrease by 20%;
- (D) Number of TMD units (2 levels): (i) Single TMD system, (ii) Double TMD system.

VI. RESULTS

A. Design Verification

There are two design aspects that are verified for the reference structure containing the TMD, which are (i) demand over capacity (D/C) ratios of the steel diagrid exterior members, and (ii) peak displacements of the TMD unit. For the member design check, the 7 crustal ground motions are averaged and incorporated in the design combinations following ASCE 7-10. The design check was performed based on AISC 360-05 [32]. A peak D/C ratio of 0.90 was obtained over all diagrid members. The TMD has limited movement. For this design, the displacement limit is ±1.5m. From the reference design the absorbers are proven to safely limit the TMD movement.

B. Comparison with Reference Model

TABLE III

Natural period and mass participation ratios of the main structure: (a) without TMD and (b) reference model (with one TMD unit)

(a) Without TMD

Mode	Period-X	Period-Y	UX	UY	RX	RY
1	6.487	6.546	0.600	0.600	0.970	0.970
2	1.546	1.549	0.210	0.210	0.028	0.027
3	0.740	0.732	0.069	0.070	0.003	0.003

(b) Reference model (with TMD)

Mode	Period-X	Period-Y	UX	UY	RX	RY
1	7.718	7.765	0.424	0.429	0.760	0.753
2	1.506	1.509	0.196	0.195	0.023	0.023
3	0.729	0.723	0.065	0.066	0.003	0.002

The improvements in terms of seismic response from the prototype building model to the reference model with one TMD unit can first be examined from the comparison of modal parameters and mass participation factors shown in Table III. By placing the TMD at the top of the building, the mass participation ratios of the first mode shape in the X- and Y-direction are decreased by 29.3% and 28.5%, respectively. From this preliminary observation, it is reasonable to expect a

significant (about 30%) reduction in the base shear for earthquake ground motions that excite mainly the first mode of the building. Minimal seismic performance improvements are expected for any records that mainly excite the building at the higher modes.

Fig. 8a shows that the utilization of a TMD system provides improvements in the peak base shear response to all shallow crustal motions, averaging (over both directions) 17.6% in reduction. Significant improvements can be seen for a few earthquake motions, with reductions of approximately 30% in base shears and base overturning moments. These improvements are related to the fact that these ground motion records excite mainly the first mode, which is the mode to which the TMD is tuned to. On the other hand, poor improvements can be seen at the base shear for NGA 1045 FN (X-dir), NGA 1044 FN (X-dir), and NGA 1605 FP (Y-dir), since those earthquakes have large contributions to the building response from higher modes.

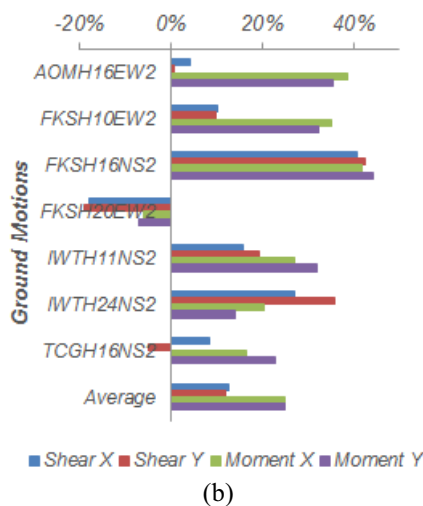
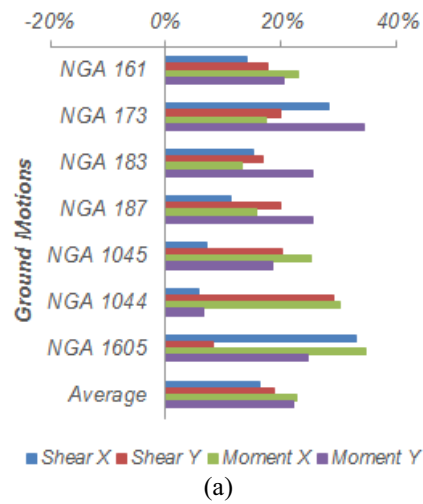


Fig. 8. Improvements peak base reactions from basic diagrid building: (a) shallow crustal earthquakes, (b) subduction zone earthquakes.

Observing the result of subduction earthquakes, the average (over both directions) improvement of peak base shears is 12.2%. This percentage is lower than the one obtained for the

shallow crustal because the setting of the TMD system is not suitable for one of the earthquake tested, that is the FKSH20EW2. However, significant improvements can still be seen at some of the earthquakes, with the reductions in maximum base shears of 40%.

Fig. 9 shows the geometric mean of peak inter-story drift, peak floor displacements, and peak absolute floor acceleration X- and Y-direction responses. It is worth noting that even though the building model (steel diagrid and reinforced concrete core) is linear, the displacements obtained from these analyses are expected to be identical to the ones that would be obtained using a nonlinear building model because the period of the building is relatively large and the “equal displacement” rule applies [11]. As seen in Fig. 9, the reference structure (with TMD) reduces the floor displacements (on average over all floors) by 19.8% for crustal earthquakes and 22.5% for subduction earthquakes. It also provides inter-story drift improvements of 17.5% for crustal earthquakes and 21.8% for subduction earthquakes. However, this TMD system is not as effective to reduce the floor accelerations as it only provides average reductions of 8.1% for crustal earthquakes and less than 1% for subduction earthquakes. This is because floor accelerations are usually controlled by higher modes which are not affected by this TMD system.

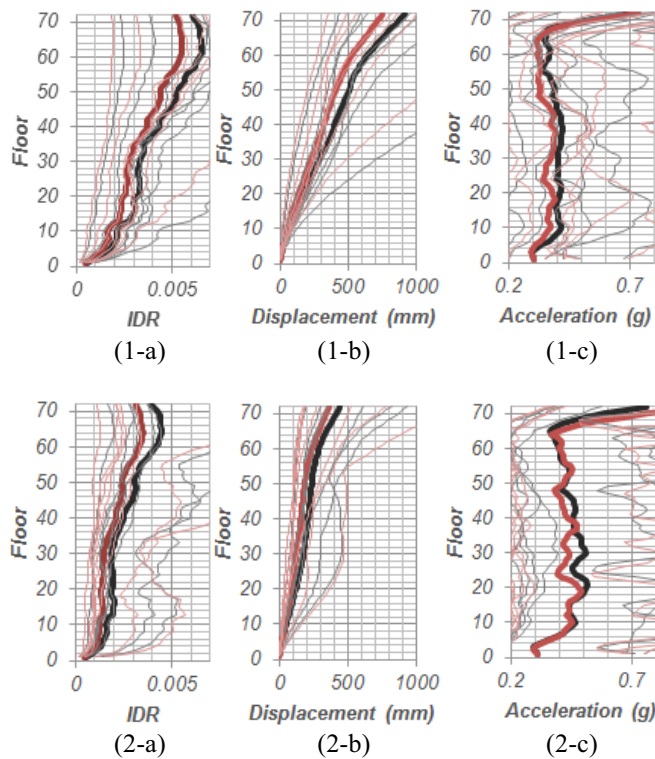


Fig. 9. Geometric means of envelope responses due to (1) crustal earthquakes and (2) subduction earthquakes for: (a) inter-story drift (IDR), (b) floor displacement, (c) absolute floor acceleration; thin lines are the responses of each model (grouped by colors) due to individual earthquake; legend: (i) **black line** is without TMD; (ii) **red line** is with TMD.

C. Variation of FPS Friction Coefficient

The parameters used in the reference structure with the

TMD unit are $f_{slow} = 0.04$ and $f_{fast} = 0.06$. To study the effect of changing the friction coefficients of the friction isolators two new levels of friction coefficients are introduced: low friction ($f_{slow} = 0.01, f_{fast} = 0.02$); and high friction ($f_{slow} = 0.08, f_{fast} = 0.12$). The friction coefficient of $f_{fast} = 0.12$ can be produced by the friction of two lubricated hard steel materials [33].

From observation of the base shears in Fig. 10, it can be seen that the structure performance is improved when friction is increased. This conclusion had also been reached elsewhere [34]. In shallow crustal motions, improvements can be seen at almost all tested ground motions. Significant reductions in base shear can be seen in NGA 161 FP (Y-dir) and NGA 173 FP (Y-dir) in which additional reductions of approximately 13% from the reference model. However, increasing the friction does not significantly affect the overall improvements in peak base shear due to subduction zone earthquakes. Nevertheless, maximum additional reduction of 14% in base shear is still observed in subduction zone motion’s response. On the other hand, lowering the friction coefficients results in smaller friction forces than those required to counteract the seismic forces and therefore, the results in the observed response are worse.

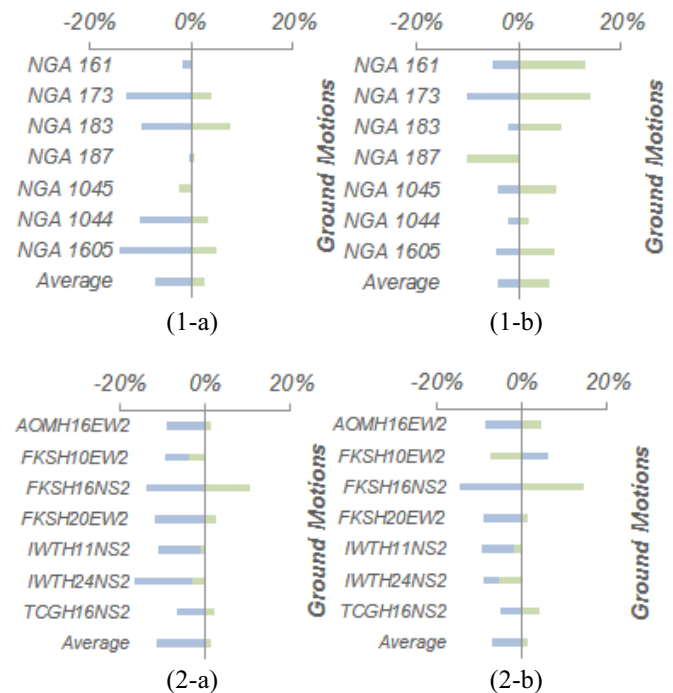


Fig. 10. Tornado plots for peak base reactions due to variations of the friction coefficient about the reference model: (1) crustal shallow motions and (2) subduction zone motions; (a) base shear X, (b) base shear Y; legend: (i) **blue bar** is low friction, (ii) **green bar** is high friction.

It is worth noting that the envelopes of inter-story drift, floor displacement, and peak absolute floor acceleration due to shallow crustal motions are not sensitive to changes in friction coefficient, as can be seen in Fig. 11. Increasing friction introduces negligible changes in those floor responses. Also, by reducing the friction, the observed floor responses due to crustal shallow motions only increase by approximately 3%. However, for subduction-zone motions, the floor

displacements are still not sensitive to changes in the friction coefficient, but the inter-story drift ratios and absolute floor acceleration are quite sensitive. High friction provides significant absolute floor acceleration reductions of 10.5% while low friction increases the inter-story drift by 7.9%.

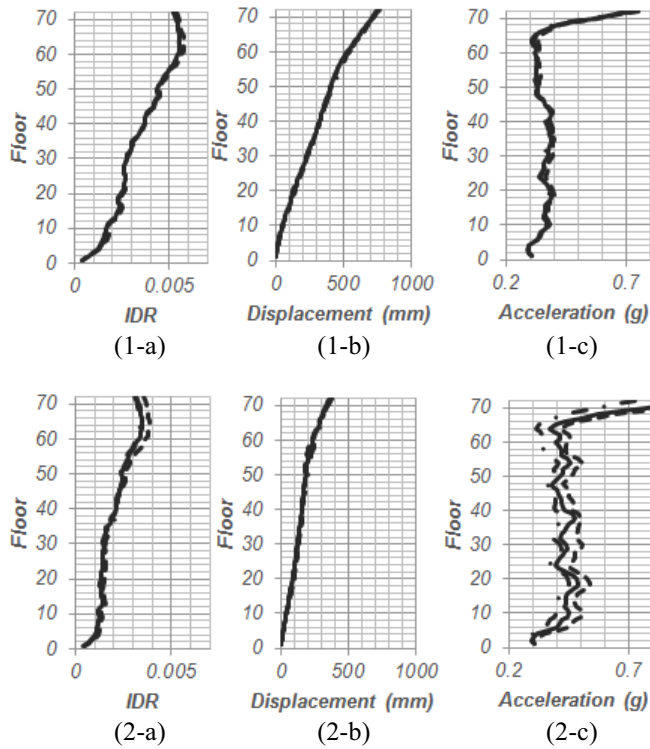


Fig. 11. Floor responses due to variations in friction coefficient: (1) shallow crustal motions and (2) subduction zone motions; (a) inter-story drift, (b) floor displacement, (c) floor absolute acceleration; legend: (i) low friction [---], (ii) reference [—], (iii) high friction [· · · · ·].

D. Variation in Height Distribution and Mass of TMD Unit

As stated in the methodology section, the configuration for the TMD system needs the mass damper to be extended for four floors for optimal load transfer to the exterior diagrid structure. Fig. 12 illustrates the sensitivity of base reactions change in height and mass of the TMD unit. It can be seen from this figure that concentration of the same mass over half the height results in an increase in base shear forces (average of both directions) of approximately 3.8% for shallow crustal motions and a decrease of 1.6% in subduction zone motions compared to the reference model. No significant changes are observed in displacement and acceleration floor responses due to crustal earthquakes compared to the reference model (with one TMD unit) as ±3% differences were observed in Fig. 13. In subduction zone earthquake’s responses, the floor drift and displacement also show insignificant changes, but the absolute floor acceleration decrease by 6.0% from the reference model.

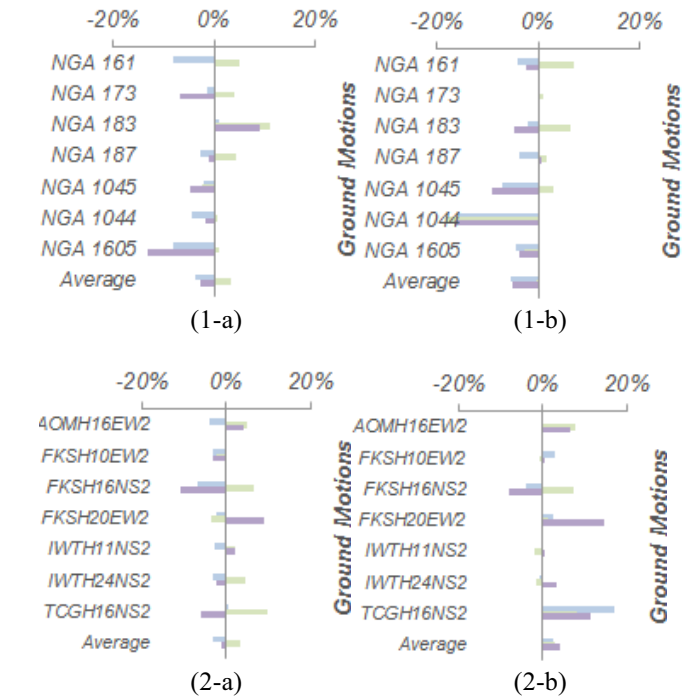


Fig. 12. Tornado plots for peak base reactions due to variation in height and mass of TMD about the reference model: (1) shallow crustal motions and (2) subduction zone motions; (a) base shear X, (b) base shear Y; legend: (i) blue bar is decrease mass, (ii) green bar is increase mass, (iii) purple bar is reduce height.

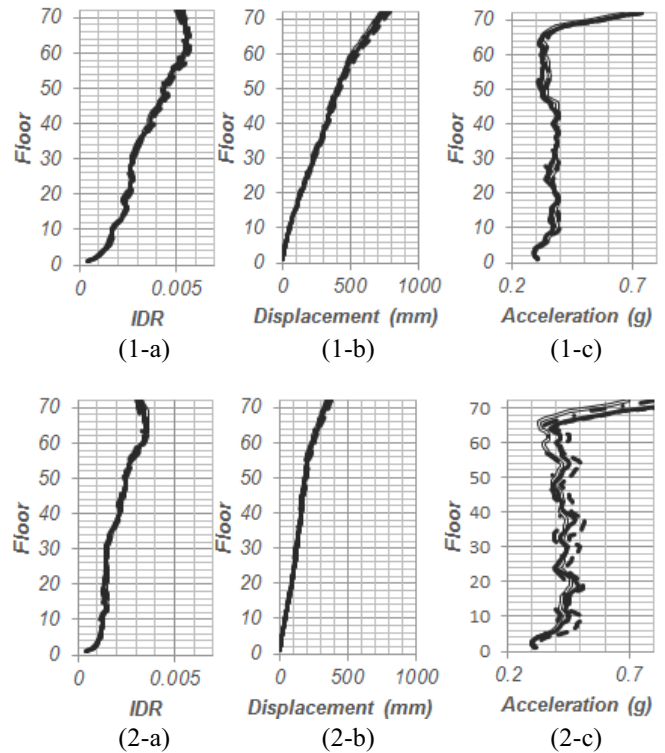


Fig. 13. Floor response due to variation in height and mass: (1) shallow crustal motions and (2) subduction zone motions; (a) inter-story drift, (b) floor displacement, (c) floor absolute acceleration; legend: (i) decrease mass [---], (ii) reference [—], (iii) increase mass [· · · · ·]; reduce height [=].

Finally, Fig. 12 also shows the results obtained by maintaining the height and friction parameters fixed to the values of the reference model as the mass was varied by two levels (+20% and -20%). By reducing the mass by 20%, the overall base shears improvements for X and Y directions due to shallow crustal motions decrease by 3 and 5%, respectively, compared to the reference model. On the other hand, the average base reaction changes due to subduction zone motions are still irregular. Nonetheless, decreasing the mass of the TMD is still decreasing the overall base reactions improvements compared to the reference model. Additionally, increasing the mass by 20% corresponds to overall base shear improvements of only 3% from the reference for shallow crustal motions and 4% for subduction zone motions. As seen from Fig. 13, the changes in mass are also not affecting the displacement and acceleration floor response for shallow crustal motions. The observed floor responses only fluctuated by approximately 3.3%. However, the changes are reasonably significant in subduction earthquakes. While floor displacements do not differ much, increasing the mass by 20% increase the overall floor absolute accelerations improvement by 7.6% while decreasing the mass will do the contrary.

E. Comparison with Double TMD System

TABLE IV
Fundamental periods and mass participation ratios of the main structure with double TMD system.

Mode	Period-X	Period-Y	UX	UY	RX	RY
1	7.727	7.775	0.427	0.431	0.761	0.754
2	1.433	1.435	0.142	0.140	0.017	0.017
3	0.728	0.722	0.065	0.066	0.003	0.002

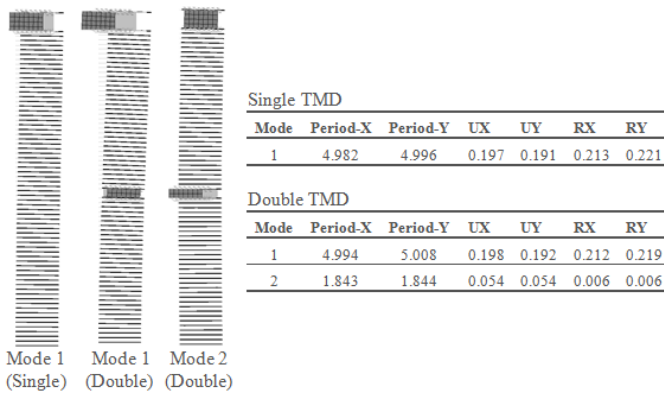


Fig. 14. Mode shapes and mass participation ratios of each mass damper in the two models.

The modal parameters and mass participation factors are still useful to estimate the expected improvements in terms of seismic response of the model with the double TMD system. TABLE IV lists the three main periods of vibration of the structure in the X- and Y-direction. Fig. 14 shows the mode shapes and mass participation ratios of each mass damper in the double TMD system in comparison the single TMD system (reference model). It can be seen that for the model

with the additional TMD in story 32, the mass participation of the first mode increases slightly, while a decrease of the mass participation ratio for the second mode is observed. It is clear, that the inclusion of the second TMD unit influences mainly the participation of the second mode, and thus this TMD unit is said to be tuned for the second mode only.

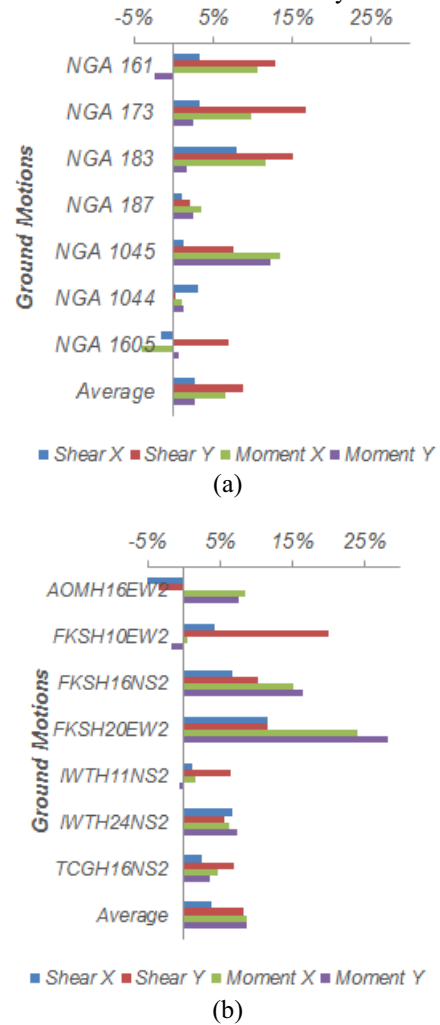


Fig. 15. Improvements in peak base reactions of double TMD system from reference model (single TMD system) due to: (a) shallow crustal motions, (b) subduction zone motions.

Fig. 15 shows that the utilization of double TMD system results in improvements in the peak base shear responses for almost all tested ground motions. For the shallow crustal motions, the double TMD system gives additional improvements of 5.7% to peak base shear responses (averaging in both directions) over the reference model and also resulting in a reduction of 23.3% of total peak base shear reduction. Significant improvements are observed for NGA 161 FP, NGA 173 FP, and NGA 183 FP with approximately 15% of additional improvements in peak base shear over the reference model. In the response generated by subduction zone motions, a similar trend is observed. The double TMD system reduce the overall peak base shear responses by 6.0% with maximum reduction of approximately 20%. However, for one particular earthquake, that is FKSH20EW2, although the

double TMD system reduces the peak base shear responses by 11.6% over the reference model, it still resulted in 7% higher peak base shear compared to the prototype building that has no TMD installed.

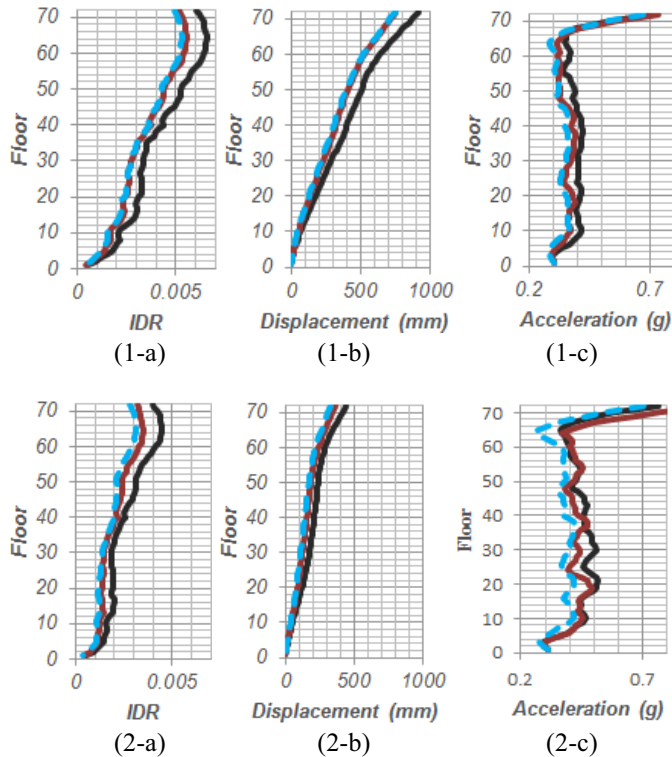


Fig. 16. Geometric means of envelope responses due to (1) crustal earthquakes and (2) subduction earthquakes for: (a) inter-story drift (IDR), (b) floor displacement, (c) absolute floor acceleration; legend: (i) **black line** is model without TMD; (ii) **red line** is model with single TMD system (reference model); (iii) **blue dashed line** is model with double TMD system.

Fig. 16 shows the geometric mean of peak story-drifts, peak floor displacements, and peak absolute floor acceleration responses. All responses show that the double TMD system has the smallest responses. In responses due to shallow crustal motions, the floor drifts and displacements improve by 4.3% from the reference model, while the floor absolute accelerations provide improvements of 5.1%. For the subduction zone motions, the double TMD system reduces the inter-story drift and displacement responses of reference model by 9.5%. Furthermore, floor absolute accelerations are also decrease by 13.1%, which is a notable improvement from the reference model.

VII. CONCLUSIONS

In this paper, a structural system known as diagrid structural system is used in the design of a prototype 72-story building. This building is assumed to be located in Seattle, Washington, in the United States, which is a region of moderate-to-high seismicity that is exposed to both shallow crustal faults and the Cascadia Subduction Zone earthquakes, both of which can produce significant and intense ground shaking. The building solution is assessed with and without the use of tuned mass

dampers (TMD) supported on friction pendulum system (FPS) isolators. The main conclusions of the paper are:

1. The buildings analyzed were subjected to an equal number of crustal and subduction motions (in total 14 motions). An equal number of crustal and subduction zone motions were selected since this approximated well the deaggregation of the seismic hazard at the site. Results presented were separated by types of earthquake motion to allow for a clear distinction between results obtained for both types of motion. Overall, from analysis of peak deformation and peak force response parameters, trends for both types of earthquake motions are identical. Results indicate that the effect of duration of the motions does not play an important role in the analysis. However, it should be noted that duration of the motion may be important in the analysis of shear and fatigue critical steel connections as the ones present in the diagonal elements, although such assessment was beyond the scope of this paper.
2. The design using one TMD unit was shown to improve the behavior of the prototype structure by reducing the base shear forces and overturning moments by as much as 20% on average and more than 30% for some motions. Peak interstory drifts and peak displacements were also reduced significantly. However, the peak floor acceleration responses were only modestly affected and can be said to have remained essentially unchanged.
3. Due to the configuration of the diagrid structural system, and since the levels where the diagonal elements cross were designed to be stronger and stiffer every four floors where the diagonal elements crossed, the TMD system was most effective if the mass damper is extended over four floors. This allows for optimal load transfer to the exterior diagrid structure.
4. Inclusion of a second TMD unit showed small improvements in the displacement and force responses when compared to the model using one TMD unit only. However, reductions in accelerations were observed when the second TMD unit was added.

The parametric study performed on the model with one TMD unit showed the following main points:

1. As the friction coefficients in the FPS are increased, the forces and accelerations in the building are reduced. These results seem to indicate that the most effective system is the one with larger friction. However, in most earthquakes, the changes in the displacements and inter-story drifts were negligible, mainly for subduction zone motions. Thus, these results seem to be competing in terms of the efficiency of the added friction.
2. Changes in the mass of the TMD unit by 20% did not correspond to significant changes in the response. This supports the conclusion that the response of TMD units supported on FPS are mainly sensitive to the friction parameters and are not very sensitive to the mass.

In summary, this document presented a design example and a TMD solution which can be incorporated into the design of a tall building using diagrid steel structures.

ACKNOWLEDGMENT

The Authors would like to acknowledge the support of the School of Civil and Construction Engineering at Oregon State University.

REFERENCES

- [1] M. M. Ali and K. S. Moon, "Structural developments in tall buildings: current trends and future prospects," *Archit. Sci. Rev.*, vol. 50, no. 3, pp. 205–223, 2007.
- [2] Council on Tall Buildings and Urban Habitat, "The Global Tall Building Database of the CTBUH," *The Skyscraper Center*, 2014. [Online]. Available: <http://www.skyscrapercenter.com/>.
- [3] I. McCain, "Diagrid: Structural Efficiency & Increasing Popularity."
- [4] S. L. Kramer, *Geotechnical earthquake engineering. in prentice-Hall international series in civil engineering and engineering mechanics*. Prentice-Hall, New Jersey, 1996.
- [5] K. Romney, "Soil-Bridge Interaction during Long-Duration Earthquake Motions," Master's Thesis, Oregon State University, Corvallis, Oregon, 2013.
- [6] Arup, "Sony City, Tokyo: A Diagrid Combined with Base Isolation," *Arup J.*, vol. 2, pp. 49–51, 2009.
- [7] A. Wada and N. Mori, "Seismic Design for the Sustainable City: A Report on Japanese Practice," in *Structures Congress 2008*, American Society of Civil Engineers, pp. 1–8.
- [8] A. Lago, T. J. Sullivan, and G. M. Calvi, "A novel seismic design strategy for structures with complex geometry," *J. Earthq. Eng.*, vol. 14, no. S1, pp. 69–105, 2010.
- [9] M. C. Constantinou and I. G. Tadjbakhsh, "Optimum characteristics of isolated structures," *J. Struct. Eng.*, vol. 111, no. 12, pp. 2733–2750, 1985.
- [10] Glotman Simpson, "Project Showcase - One Wall Centre," *Glotman Simpson Consulting Engineers*, 2001. [Online]. Available: <http://www.glotmansimpson.com/Commercial/One-Wall-Centre>. [Accessed: 03-Nov-2013].
- [11] A. K. Chopra, *Dynamics of structures: Theory and applications to earthquake engineering*, 2nd ed. Saddle River: Prentice Hall, 2001.
- [12] J. A. Inaudi and J. M. Kelly, "A friction mass damper for vibration control," Earthquake Engineering Research Center, University of California, Berkeley, California, UCB/EERC-92/15, 1992.
- [13] P. H. Wirsching and G. W. Campbell, "Minimal structural response under random excitation using the vibration absorber," *Earthq. Eng. Struct. Dyn.*, vol. 2, no. 4, pp. 303–312, 1973.
- [14] F. Sadek, B. Mohraz, A. W. Taylor, and R. M. Chung, "A method of estimating the parameters of tuned mass dampers for seismic applications," *Earthq. Eng. Struct. Dyn.*, vol. 26, no. 6, pp. 617–636, 1997.
- [15] M. N. Hadi and Y. Arfiadi, "Optimum design of absorber for MDOF structures," *J. Struct. Eng.*, vol. 124, no. 11, pp. 1272–1280, 1998.
- [16] K. Xu and T. Igusa, "Dynamic characteristics of multiple substructures with closely spaced frequencies," *Earthq. Eng. Struct. Dyn.*, vol. 21, no. 12, pp. 1059–1070, 1992.
- [17] G. Chen and J. Wu, "Optimal placement of multiple tune mass dampers for seismic structures," *J. Struct. Eng.*, vol. 127, no. 9, pp. 1054–1062, 2001.
- [18] A. Lucchini, R. Greco, G. C. Marano, and G. Monti, "Robust Design of Tuned Mass Damper Systems for Seismic Protection of Multistory Buildings," *J. Struct. Eng.*, 2013.
- [19] G. Mosqueda, A. S. Whittaker, and G. L. Fenves, "Characterization and modeling of friction pendulum bearings subjected to multiple components of excitation," *J. Struct. Eng.*, vol. 130, no. 3, pp. 433–442, 2004.
- [20] Y.-K. Wen, "Method for random vibration of hysteretic systems," *J. Eng. Mech. Div.*, vol. 102, no. 2, pp. 249–263, 1976.
- [21] Y. J. Park, Y. K. Wen, and A. Ang, "Random vibration of hysteretic systems under bi-directional ground motions," *Earthq. Eng. Struct. Dyn.*, vol. 14, no. 4, pp. 543–557, 1986.
- [22] G. Ramadhan, "Seismic performance of diagrid steel structures using single and double friction mass dampers," Master's Thesis, Oregon State University, Corvallis, Oregon, 2013.
- [23] K. S. Moon, "Optimal grid geometry of diagrid structures for tall buildings," *Archit. Sci. Rev.*, vol. 51, no. 3, pp. 239–251, 2008.
- [24] American Society of Civil Engineers, *Minimum design loads for buildings and other structures*. Virginia: ASCE, 2010.
- [25] PEER, "2011 PEER Ground Motion Database – Beta Version," *PEER Ground Motion Database*, 2011. [Online]. Available: http://peer.berkeley.edu/peer_ground_motion_database/spectras/new. [Accessed: 20-Aug-2013].
- [26] National Research Institute for Earth Science and Disaster Prevention, "Strong-Motion Seismograph Networks." [Online]. Available: <http://www.k-net.bosai.go.jp>. [Accessed: 03-Feb-2013].
- [27] A. R. Barbosa, H. B. Mason, and K. Romney, "SSI-Bridge: Solid-Bridge Interaction During Long-Duration Earthquake Motions," University of Washington, Seattle, WA, USDOT University Transportation Center for Federal Region 10, PacTrans Report, 2014.
- [28] J. W. Baker, "Quantitative classification of near-fault ground motions using wavelet analysis," *Bull. Seismol. Soc. Am.*, vol. 97, no. 5, pp. 1486–1501, 2007.
- [29] Computer and Structures, *SAP2000 v15.1.0*. Berkeley: Computer and Structures, 2011.
- [30] A. C. I. Committee, "Building code requirements for structural concrete (318-11) and commentary-(318R-11)," *Detroit Mich. Am. Concr. Inst.*, 2011.
- [31] J. Scheller and M. C. Constantinou, "Response history analysis of structures with seismic isolation and energy dissipation systems: verification examples for Program SAP2000," *Tech. Rep. MCEER*, no. 99-0002, 1999.
- [32] B. ANSI, "AISC 360-05-Specification for Structural Steel Buildings," *Chicago! AISC*, 2005.
- [33] R. Ramsdale, "Reference Tables - Coefficient of Friction," *Engineer's Handbook*. [Online]. Available: <http://www.engineershandbook.com/Tables/frictioncoefficients.htm>. [Accessed: 20-Oct-2013].
- [34] T. A. Morgan and S. A. Mahin, "The optimization of multi-stage friction pendulum isolators for loss mitigation considering a range of seismic hazard," in *Proceedings of the 14th World Conference on Earthquake Engineering*, Beijing, China, 2008.